Design of Multifunctional Nanomaterials to Improve Cancer Gene Therapy

Kui Wang

A dissertation

submitted in partial fulfillment of the

requirements for the degree of

Doctor of Philosophy

University of Washington

2015

Reading Committee:

Miqin Zhang, Chair

John R. Silber

Fumio Ohuchi

Forrest M. Kievit

Program Authorized to Offer Degree:

Materials Science and Engineering

University of Washington

Abstract

Design of Multifunctional Nanomaterials to Improve Cancer Gene Therapy

Kui Wang

Chair of the Supervisory Committee:
Professor Miqin Zhang
Materials Science and Engineering

Gene therapy shows promise for individualized cancer therapies. Compared to conventional treatments, this approach offers a variety of advantages, including a multiplicity of gene targets that define tumor clinical behavior, high specificity, low off target toxicity, and suppression of drug resistance. However, the lack of efficient delivery strategies for gene-specific agents and preclinical models for evaluation of the efficacy of gene-based therapeutics has impeded its clinical application. Nanoparticles provide a flexible platform for fabricating novel delivery vehicles capable of transporting gene-specific therapeutic agents to target tumors. Among the various types of nano-carriers for cancer therapy, superparamagnetic iron oxide nanoparticles have emerged as a leading candidate as they have a host of advantages compared to other formulations. The iron oxide core facilitates the condensation of other molecules to it that confer

biological properties that promote stability during transport through the circulation, penetration of physiological barriers such as the blood brain barrier, and targeted uptake by tumor cells by pinocytosis and endocytosis. Nanoparticles are formulated to minimize off target toxicity by using materials that are inherently biocompatible and facilitate rapid clearance from the circulation. Most importantly, these properties are maintained when the nanoparticles are derivatized to transport biologically active nucleic acids to affect tumor gene expression.

This dissertation documents the development of multifunctional drug delivery nanoparticles to improve cancer gene therapy. We first developed and characterized the functionality of an iron oxide-based nanoparticle containing a copolymer that binds a biologically active gene that activates an inherent tumor cell death pathway. This nanoparticle was also derivatized with a targeting peptide to improve tumor-specific gene delivery. The nanoparticle displayed little intrinsic toxicity and mediated excellent uptake of biologically active gene as evidenced by elevated glioblastoma (GBM) cell killing *in vitro* and suppression of GBM xenograft growth *in vivo*.

We next modified the nanoparticle to deliver RNA interference (RNAi)-based gene therapy. In collaboration with faculties in the Department of General Surgery, we demonstrated that nanoparticle-mediated small interfering RNA (siRNA) delivery can effectively suppress expression of target genes in cancer cells without notable cytotoxicity *in vitro*. Importantly, we have shown that recognition of a tumor cell surface epitope by an antibody-derivatized nanoparticle improves binding to target cells and greatly enhances inhibition of target gene expression in an orthotopic liver cancer mouse model *in vivo*.

After evaluating the efficacy of targeted delivery of siRNA, we determined the effect of siRNA-mediated suppression of biochemical pathways associated with malignancy and of

another with drug resistance in GBM cells *in vitro*. siRNA-mediated gene suppression reduced GBM cell motility, a hallmark of aggressive behavior, increased endogenously-induced apoptosis and increased sensitivity to temozolomide, the standard drug for GBM, by reducing the level a of key DNA repair enzyme, O6-methylguanine-DNA methyltransferase (MGMT). Systemic delivery of tumor targeting-nanoparticles carrying anti-MGMT-siRNAs reduced MGMT expression in an orthotopic xenograft model of a human GBM. Of clinical significance, reduction of tumor xenograft MGMT activity was accompanied by statistically significantly longer survival compared to control-treated animals. Our findings are the first substantive demonstration of a potential anti-resistance therapy that may enhance the efficacy of current GBM treatments and prolong survival.

Finally, we have developed a three-dimensional (3D) tissue culture model to better mimic of tumor microenvironment for the evaluation of nanoparticle-mediated gene delivery. Significantly, we found that targeted gene delivery was only observed in cells cultured in scaffolds whereas cells cultured on two-dimensional (2D) plates showed no difference in gene delivery between targeted and non-target control nanoparticles. *In vivo* evaluation of gene delivery in a xenograft tumor mouse model further demonstrated that 3D culture system can correctly modeled nanoparticle-mediated targeted delivery *in vivo*.

TABLE OF CONTENTS

LIST OF FIGURES

LIST OF TABLES

ACKNOWLEDGEMENTS

I would first and foremost like to thank my advisor, Prof. Miqin Zhang, whose mentorship, support, and encouragement guided me through completion of the degree. Without her guidance and persistent help this dissertation would not have been possible.

I would also like to thank my mentors, Prof. John R. Silber and Prof. Forrest M. Kievit, for their patience, encouragement, and guidance. Their critical attitude and comprehensive insight towards research was always a huge inspiration throughout my education.

I would also like to thank my committee members, Prof. Fumio Ohuchi and Prof. Marjorie A. Olmstead, who took time out of their busy schedules to provide valuable feedback on my graduate work. Additionally, I would like to thank our collaborators, Prof. Richard G. Ellenbogen and Prof. James O. Park, who offered much support during my Ph.D. studies.

I am grateful to all Zhang lab members who helped contribute to my projects. I certainly enjoyed working with them, and hope to work with many again in future collaborations. I would also like to thank all colleagues and friends outside Zhang lab for their support. I am also grateful to the staff at the Department of Materials Science and Engineering for their various forms of support during my graduate study.

I am indebted to my family for their support and reassurance they so gratefully offered; to my father Leisheng Wang, my mother Xiaoe Wang, my parents-in-law Jin Ding and Chunxiang Ren for their support, and specially to my dear wife Li Ding for her caring and understanding and for standing strongly by during my pursuit of graduate research. Without that, I would not have made it this far. I would also like to dedicate this dissertation to the memory of my grandparents Zongliang Wang, Kan Wang, and Sue Ye, whose roles in my life were, and remain immense.

Finally, I would like to acknowledge the funding I received that supported this work. I would like to acknowledge the College of Engineering Dean's Fellowship (the Scott Fellowship and the Marsh Fellowship) at University of Washington. I would further like to acknowledge the research grants (NIH/NCI R01EB006043, R01CA134213, R01CA161953, R01CA119408, and R01CA172455) that funded this work.

1. **INTRODUCTION**

Despite considerable advances in cancer research in the last two decades, cancer remains the second leading cause of death in the U.S., and is expected to surpass heart diseases as the leading cause of death in the near future [1]. Current standard treatments including surgery, radiation, and chemotherapy, are usually effective against local disease. However, there are a sizeable number of newly diagnosed tumors that remain refractory to treatment (*e.g*, malignant gliomas, pancreatic adenocarcinoma, non-small cell lung adenocarcinoma). Moreover, the prognosis for metastatic and recurrent tumors remain grim, in large part due to intrinsic and acquired resistance as well as the debilitating effects of salvage therapies [2]. Additional safe and effective therapeutic regimens are urgently needed to improve overall cancer outcome. Gene therapy that targets the expression of genes responsible for tumor malignant behavior and resistance to treatment-induced cell death has the potential of overcoming limitations of conventional treatments. However, clinical application of cancer gene therapy is impeded by the lack of safe and efficient delivery strategies. In addition, the discordance between *in vitro* and *in vivo* evaluation of the utility of gene therapy limits its development and translation to clinical application.

Nanoparticles are potentially effective gene delivery vehicles. To successfully deliver therapeutic agents, nanoparticles must be designed to (1) avoid elimination from the circulation by clearance organs, (2) protect anti-tumor agents during transport, (3) circumvent physiological barriers that protect tumors, and (4) be taken up preferentially by tumor cells [3]. This requires the fabrication of nanomaterials into multifunctional particles that possess appropriate physiochemical properties. Nanoparticles can be synthesized from a variety of materials including polymers, dendrimers, liposomes, carbon nanotubes, metal, metal-oxide, and so forth [4]. Multifunctional nanoparticles, typically through nanocrystalline synthesis, advanced polymer processing, coating and functionalization strategies, can simultaneously provide detection and therapeutic delivery capacities. In addition to nano-carriers, nanomaterials can also be applied in the synthesis of three-dimensional (3D) *in vitro* tissue culture model that better mimics tumor physiological behavior to facilitate preclinical evaluation of gene therapy

strategies by bridging the gap between *in vitro* and *in vivo* analyses [5]. The goal of the work presented in this dissertation was to develop nanomaterials to overcome these limitations.

This dissertation documents the development of an iron oxide nanoparticle coated with polycationic copolymer composed of chitosan, polyethylenimine (PEI), and polyethylene glycol (PEG), and its application as a gene delivery vehicle. Chitosan is a natural polymer derived from crustacean shells. It can form an effective coating to stabilize the iron oxide nanoparticle and has ample functional groups to attach functional ligands [6]. PEI is still considered as the most potent gene delivery polymer due to its high nucleic acid binding capacity and facilitation of endosomal release [7]. PEG serves as a stabilizer that prevents particle agglomeration that promote biodistribution and prolongs blood half-life [8]. Of note, it is also able to reduce the toxicity induced by PEI. Target-specific delivery of a suicide gene capable of inducing apoptosis and small interfering RNA (siRNA) against a known resistance mechanism were demonstrated both *in vitro* and *in vivo*. Importantly, delivery of either gene prolonged survival in mouse human tumor xenografts. Finally, a 3D porous chitosan-alginate (CA) polyelectrolyte complex scaffold was developed, which has been demonstrated to better represent the tumor microenvironment than standard two-dimensional (2D) cultures [9, 10]. Nanoparticle-mediated gene delivery was evaluated in cancer cells cultured on CA scaffolds, which was further compared with that in mice bearing xenograft tumor *in vivo*. Taken together, this dissertation demonstrate that the iron oxide-based nanoparticle can provide a means for safe and efficient cancer gene therapy, and 3D CA scaffolds can serve as a platform for preclinical evaluation of novel gene therapeutics.

This dissertation is organized as follows:

Chapter 1 provides an introduction and rationale for the work, highlighting the current challenges in clinical application of cancer gene therapy.

Chapter 2 reviews cancer gene therapy, including its mechanisms, delivery strategies, and limitations that prevents its translation to the clinic.

Chapter 3 describes the development of an effective gene therapy nano-vehicle that provides targeted suicide gene delivery to brain tumor *in vitro* and *in vivo*.

Chapter 4 investigates the application of the nanoparticle system developed in Chapter 3 in siRNA-mediated RNAi in cancer.

Chapter 5 presents the development of two RNAi-based gene therapies for brain cancer *in vitro*.

Chapter 6 evaluates the therapeutic combining siRNA-mediated gene suppression and chemotherapy developed in Chapter 5 *in vivo*.

Chapter 7 investigates the use of a 3D *in vitro* tissue culture model to more accurately represent the behavior nanoparticle-mediated gene delivery to tumors *in vivo*.

Chapter 8 summarizes the work and provides conclusions.

2. GENE THERAPY

2.1 BACKGROUND

Gene therapy was initially designed to treat germ line genetic diseases by introducing normal version of a defective or missing gene [11]. The introduced nuclei acids included whole genes, gene segments, or oligonucleotides. Gene delivery was first achieved using mammalian viruses capable of integrating their genome with that of infected cells. Viral mediated delivery, however, soon fell out of favor due to the inability to target gene insertion in target cells. Enthusiasm was further diminished by the death of a young subject in an adenovirus-based gene therapy for treatment of partial ornithine transcarbamylase deficiency in 2000 [12]. While these findings emphasized the need to develop novel gene locus delivery vehicles, they provided proof of principal of the potential of gene therapy in treating human disease, especially diseases caused by somatic mutation such as cancer.

2.2 GENE THERAPY FOR CANCER

Despite advances for a number of hematologic and solid tumors, many current cancer therapies fail to produce durable remissions in an appreciable fraction of patients. For pancreatic, lung, liver, and glial brain tumors, five-year survival rates remain abysmally low. Even tumors that are highly responsive to initial treatment (*e.g.*, prostate and breast cancer) frequently display lethal treatment resistance upon recurrence [13]. While conventional treatments can produce lasting remissions, survival following aggressive surgical intervention followed by radio- and chemotherapy is often accompanied by deleterious physical and/or cognitive consequences that degrade quality of life. Although better controlled than in the past, the systemic toxicity of chemotherapy still results in acute and delayed nausea, mouth ulcerations, and mild cognitive impairments [14]. The long-term side effects can also increase the risk of developing other types of cancers. Similarly, radiation therapy can also cause a host of side effects, including diarrhea, mucositis, skin toxicity, and xerostomia [15]. As a result, considerable research has been devoted to the development of novel therapies that minimize off target toxicity. Gene therapy holds unique promise of meeting this goal by offering a means of specific targeting of tumor genes that

promote malignant behavior and treatment resistance.

Since the first gene therapy study approved by the U.S. Food and Drug Administration (FDA) in 1990 for severe combined immunodeficiency disorder [15], the majority of gene therapy trials worldwide are aiming at the treatment of solid and hematological malignancies [16]. To date, successful trails have been reported in patients with chronic lymphocytic leukemia, acute lymphocytic leukemia, brain tumors, as well as others. Several gene therapy products are successful in the clinic, including ONYX-15 (Onyx Pharmaceuticals) for refractory head and neck cancer [17]; human papilloma virus vaccine (Gardasil) (Merck Sharp & Dohme) for the prevention of cancer cervix [18]; and modified dendritic cells, sipuleucel-T (Provenge) (Dendreon Corporation), for metastatic, asymptomatic, hormone-refractory prostate cancer [19].

2.3 Approaches of Cancer Gene Therapy

2.3.1 Gene Silencing

Suppression of gene expression utilizing RNA interference (RNAi) may provide a means to target malignant cells while avoiding the systemic toxicity. In principle, this approach would specifically deliver small interfering RNA (siRNA) or short hairpin RNA (shRNA) to target cells. Duplex RNA formed by binding of target mRNA and therapeutic siRNA would then be degraded by the RNA-induced silencing complex (RISC), thus suppressing gene expression within the target cells [20]. This process offers the opportunity to target genes uniquely expressed in tumor cells that are responsible for malignant behavior while sparing normal tissue. Such specificity and low toxicity would be far superior to conventional treatment regimens [21-23]. Genes involved in tumor behavior such as oncogenes, and mutated tumor suppressor genes, and genes that promote resistance to apoptosis are potential targets for RNAi-based therapies. Unlike most contemporary treatment regimens genes in multiple pathways determining tumor behavior can be simultaneously targeted for greater therapeutic effect [24]. However, due to the extreme sensitivity of therapeutic RNAs to degradation by endogenous nucleases, only a few siRNA therapeutics have reached clinical trial [25, 26].

2.3.2 Suicide Gene

Suicide gene therapy is based on the use of transgenes that produce therapeutic proteins or conversion of a non-toxic compound into a lethal drug after being introduced into tumor cells. Among the suicide systems that have been reported, herpes simplex virus type-1 thymidine kinase with ganciclovir (HSV-tk/GCV), cytosine deaminase (CD), the bcl-2-like protein 4 (Bax), and human tumor necrosis factor α-related apoptosis-inducing ligand (TRAIL), are the most extensively studied due to their cytotoxicity in tumor cells [27-29].

HSV-tk/GCV is one of the most thoroughly studied gene therapy systems. The HSV-tk gene can produce viral thymidine kinase that metabolizes GCV to ganciclovir monophosphate and further converted into ganciclovir triphosphate, which inhibits DNA polymerization, leading to tumor cell death. This approach has shown promising preclinical efficacy in a number of cancers, including melanoma, neuroblastoma, leukemia, bladder cancer, intrahepatic metastasis of liver cancer, colon adenocarcinoma, and oral cancer [30-35]. Using a similar strategy, CD is used to catalyze the non-toxic prodrug 5-FC to 5-FU that is subsequently converted by endogenous enzymes into potent pyrimidine antimetabolites (5-FdUMP, 5-FdUTP, 5-FUTP) that induce apoptosis. The efficacy of CD/5-FC system has been demonstrated in fibrosarcomas, carcinomas, gliomas and metastatic formations of different origin [36-39].

BAX was the first identified pro-apoptotic member of the bcl-2 protein family. Bax relays pro-apoptotic signals within cells by activating the caspase pathway and inducing release of apoptotic molecules such as cytochrome c from the mitochondria to the cytosol. By this mechanism, over-expression of BAX induces cells to undergo apoptosis. This has been shown to induce apoptosis in a wide variety of cell lines including those derived from prostate, colon, cervical, and ovarian cancers [40-44]. TRAIL is a TNF cytokine superfamily member, which forms a homotrimer that crosslinks death receptors (DRs) on the cell surface leading to downstream signaling of apoptosis [45, 46]. TRAIL is an attractive anticancer agent due to its ability to induce apoptosis in various types of tumors without significant cytotoxicity towards normal cells [47-49].

2.3.3 MicroRNA (miRNA)

As endogenous regulators of mRNA expression and function, miRNAs are attractive targets for gene therapies for cancer. Since their discovery, the abnormal expression of miRNA have been associated with tumor formation, progression and metastasis, as well as chemo-resistance [50]. The goal of miRNA-based is to restore normal function by either suppressing or eliciting expression of tumor-associated miRNAs. Thus, in contrast to siRNA/shRNA-mediated gene therapy, both antagonists and mimics are used depending on miRNA function and its status in the diseased tissue. miRNA antagonists are designed to interrupt the suppressive miRNA processing and RISC assembly, resulting in increased gene expression that can reverse malignant behavior (*e.g.*, tumor suppressor genes). In contrast, the aim of miRNA mimics, also known as miRNA replacement therapy, is to stimulate expression of silenced genes. In practice, miRNA antagonism is achieved by directly modifying nucleic acids that can bind and inhibit the mature miRNA [51], while miRNA mimics are typically packaged and delivered by vesicles. Successful preclinical studies have appreciated the therapeutic potential of several miRNA, including restoring the expression Let 7, miR-16, and miR-31. In particular, a liposome-based mimic of miR-34 has reached clinical trial [52].

2.3.4 Immunomodulation

Immunotherapy, the use of a person's own immune system to treat an infection or disease, has recently been at the forefront of cancer research. The curative potential largely depends on the administration of allogeneic T cells, especially for adoptive immunotherapy. In this treatment modality, patients' T cells are modified *ex vivo* to better recognize and respond to tumor antigens. The genetically modified T cells are then infused back into the patient. The modification typically involves the genetic engineering of those autologous T cells to express either chimeric antigen receptor (CAR) or affinity-enhanced T cell receptor (TCR) that recognize tumor target antigens, both are usually conducted by oncoretroviral vector transduction [53]. The CAR consists of an antibody-derived targeting domain fused with T cell signaling domains. When expressed by a T cell, it endows the T cell with antigen specificity determined by the targeting domain of the CAR. Immunotherapy using CAR T cells has been under development

for almost three decades, but until recent years the clinical successes with CD19-targeted CAR T cells pave the way for broader clinical application, particularly in the arena of solid cancers [54]. TCR-engineered T cells have been employed in a number of early-stage clinical trials for melanoma [55], and significant clinical response has been identified in myeloma using TCR-engineered T cells [56]. Overall, immunotherapy has indicated the potential to change the course of cancer treatment and may offer the long-elusive possibility of a cure for some types of cancer. But a collaborative and integrative approach will be the key to maximizing the impact of the field as a whole.

2.4 Gene Delivery Strategies

Efficient delivery of therapeutics into target tissues is critical for the success of gene therapy. Several methods have been developed to facilitate the entry of transgene products into target cells. In general, they are broadly divided into two major categories: viral and non-viral vectors.

2.4.1 Viral-Based Vectors

Viral-based gene delivery represents one of the most efficient means of gene transfer among all current methods. They have been widely studied in detail and many have been tested in clinical trial. They can provide robust expression of transgenes in diseased tissues, are easily produced in quantity, and are amenable to genetic manipulation to suppress immunogenicity and improve safety [57]. The main groups of viral vectors include adenoviruses, retroviruses, adeno-associated viruses, and lentiviruses, which vary in packaging capacity, host specificity, gene expression profile, and tendency to elicit immune responses, particularly when repeated administrations are required. In general, viral vectors fall into one of two main categories: integrating vectors (such as retroviral and lentiviral vectors), which insert into the recipient's genome; and non-integrating vectors (adenoviral vectors and adeno-associated vectors). Both have been utilized in delivering a wide range of therapeutic nucleic acids.

2.4.2 Bacteria

Bacteria are an emerging family of vectors for cancer gene therapy. Several strains of *Clostridia*, *Bifidobacteria,* and *Salmonellae* were originally found selectively colonize the hypoxic areas of tumors and destroy the tumor cells, and thereby provide a more selective tumor-targeted therapy [58]. Besides direct cell killing, these bacteria can be further enhanced by genetic modifications for targeted delivery of gene products to tumors. In such application, bacteria can deliver suicide genes, cytokines to evoke immune-response of the host, tumor-associated antigens as DNA vaccines, or a gene/enzyme able to convert systemically administered prodrug into its active compound specifically in tumor tissue [59]. Additionally, the anti-cancer effect of tumor-targeting bacteria can be achieved through oral administration, which may circumvent the use of the intravenous route of delivery and its associated adverse events.

2.4.3 Mammalian Stem Cell-Based Delivery

Mammalian cells, especially stem cells, can serve as an alternative delivery vehicle for tumor-targeted gene therapy. Stem cells hold therapeutic advantages such as tumor homing ability and ease of acquisition when compared to other vehicles such as proteins, antibodies, nanoparticles, and viruses. Mesenchymal stem cells, usually isolated from human bone marrow or adipose tissue, have been demonstrated feasible in delivering a wide range of gene therapeutics into various types of tumors, inhibiting their growth, and extending animal survival [60]. Besides mesenchymal stem cells, neural stem cells and hematopoietic stem cells have also been considered as vehicles for delivering anticancer therapeutics [61].

2.4.4 Nanoparticle Carriers

Many types of nano-sized constructs, including liposomes, polymer-based and metal-based nanoparticles, have been developed to deliver gene therapeutics. Among all the nano-carriers, liposomes are the oldest and most studied. Liposomes are microscopic vesicles of synthetic phospholipids and cholesterol that can enter into cells by endocytosis [62]. Their advantages include selective uptake by endothelial cells, relatively high gene transfer efficiency,

biocompatibility, and biodegradability [26]. Their abilities to deliver a variety of therapeutic molecules, such as drugs, nucleotides, proteins, plasmids, and large genes, have been demonstrated in many cancer models. Of note, the PEGylated form of doxorubicin (DOXIL in the U.S.) is used to treat a variety of human tumors [63].

Polymeric particles are among the most widely explored organic nanoparticles. They offer several advantages, including the ability to encapsulate a wide variety of drugs and release them over prolonged periods. They can be modified with targeting ligands on the surface, and show excellent stability *in vitro* and *in vivo*. Biodegradable polyesters such as poly (lactic acid) (PLA), poly (glycolic acid), poly (ε-caprolactone), poly (orthoesters), and poly (anhydrides) have been widely explored for various drug delivery applications. Copolymers of hydrophobic polymers, such as those listed above, with hydrophilic polymers such as poly (ethylene glycol) (PEG), poly (ethylene oxide) (PEO), and poly (propylene oxide) (PPO) are used to synthesize self-assembled therapeutic carriers. In addition, polymers that can respond to external stimulus such as temperature, pH, or electromagnetic radiation, are also being actively explored to facilitate drug delivery [64].

Inorganic nanoparticles made of metal, metal oxide, semiconductor, and silica are another important class of nano-sized structures. These nanoparticles often possess unique electric, magnetic, optical, and plasmonic properties due to quantum mechanical effects observed at nano-scales. Most of the nanoparticles can be generated with a great deal of control over size, shape, and composition, as well as chemical properties. As a result, many inorganic nanoparticles are now commercially available. Several types of inorganic nanoparticles are multifunctional due to the nature of the materials. For instance, gold nanoparticles are remarkable contrast agents for optical imaging, photoacoustic imaging, computed tomography, and photothermal properties [65]. Magnetic iron oxide nanoparticles have potential as MRI contrast agents [66]. Magnetic nanoparticles within the size limit of the magnetic domain wall become superparamagnetic, which can significantly increase MRI. In this dissertation, we developed a superparamagnetic iron oxide nanoparticle, and its physicochemical property was further tuned by coating with biocompatible copolymers and functionalized with targeting agents.

2.5 CHALLENGES OF CANCER GENE THERAPY

It is well recognized that the fundamental engineering challenge of successful gene therapy lies in the development of safe and effective delivery vectors that can deliver efficacious doses of therapeutic agent while circumventing biological barriers that impede delivery. However, the poor correlation between *in vitro* and *in vivo drug* evaluation outcomes has limited the development of novel gene therapy. A detailed understanding of the impediments to gene therapy and developing approaches to circumvent these obstacles are essential for achieving its ultimate potential.

2.5.1 Limitation of Current Delivery Strategies

Although many types of gene delivery strategies have been developed with several under clinical trial, limitations remain that prevent their translation to the clinic. The major unresolved problem in viral-based cancer gene therapy is the host immune response and the resulting toxic side effects, especially adenovirus-associated liver toxicity. Repeated administration of viral vectors is often required to achieve successful therapeutic effect, but this strategy can also promote immune response against the vector. But the host immune response can significantly hamper the viral-mediated gene transfer although the viral vectors are engineered to reduce their immunogenicity. Progress has been made to overcome vector immunogenicity, including modification of the virus [67] or co-administering an immune-suppressing agent to suppress the host immune response [68]. Specificity of transgene delivery is another potential issue of viral-based gene delivery as the systemic delivery of vector generally leads to unwanted vector uptake by many different cell types in multiple organs. All these issues need to be fully addressed before this type of delivery can be applied in clinical.

As compared to the cumbersome, time consuming, and expensive generation process of viral vectors, bacterial vectors are easier to manufacture. The biggest challenge of using recombinant bacteria in humans is the prevention of biological contamination. Particular care must be taken to prevent lateral gene transfer to other bacteria and to limit environmental spread of the vector. Further work is also required to limit potential adverse side-effects and to optimize delivery. Similarly, although remarkable progress has been made at the preclinical level, clinical

application of stem cells as gene delivery strategies requires further optimization due to the lack of a suitable method for *ex vivo* expansion and poorly understood *in vivo* kinetics of delivery.

To date, most nanoparticle systems are non-toxic, being composed of biocompatible and biodegradable materials to facilitate clinical use. In this regard, they are considered as safer delivery approach than viral- and bacteria-based vectors. Although many nanoparticle systems have shown promise *in vitro* as tumor-specific gene delivery vehicles, their clinical application continues to be limited by poor potency, uncertain target specificity, and unacceptable levels of systemic toxicity [69-71].

2.5.2 Lack of Efficient In Vitro Models

Another hurdle impeding the development of novel gene therapeutics is the lack of a physiologically relevant *in vitro* model of many human tumors. Currently, evaluating nanoparticle-based gene delivery, including target specificity, is a time-consuming, uncertain, expensive and low yield process for a number of reasons [72]. Typically, *in vitro* study of the nanoparticle delivery on two-dimensional (2D) cell culture is followed by extensive *in vivo* evaluation in animal models of human tumors prior to translation to clinical trials. However, successful nanoparticle delivery observed in 2D cell culture studies does not usually translate well to *in vivo* studies. This is in part due to the inability of monolayer cultures to replicate the three-dimensional (3D) morphology of solid tumors, the tumor microenvironment and the extracellular physiological barriers present *in vivo* [73].

3D cell cultures are employed to address these limitations as they provide a more realistic model of the *in vivo* tumor morphology and pathophysiology than adherent cells cultured on conventional 2D plates [5, 74]. During the last decades, numerous types of 3D cell culture systems have been developed, composed mostly of natural materials, such as collagen, gelatin, polysaccharides and so forth [75]. However, use of 3D cultures to evaluate nanoparticle delivery is not widespread, primarily due to the difficulties in manipulating 3D cultures, uniformly introducing nanoparticles into cells grown as tumor spheroids in the 3D matrix [76]. As a result, there have been few studies examining the correlation between the nanoparticle-based drug delivery in 3D cultures and *in vivo*.

3. IRON OXIDE NANOPARTICLE FOR SUICIDE GENE-BASED GENE THERAPY

Human tumor necrosis factor α-related apoptosis-inducing ligand (TRAIL) is an attractive cancer therapeutic because of its ability to induce apoptosis in tumor cells while having a negligible effect on normal cells. However, the short serum half-life of TRAIL and lack of efficient *in vivo* administration approaches have largely hindered its clinical use. Using nanoparticles (NPs) as carriers in gene therapy is considered as an alternative approach to increase TRAIL delivery to tumors as transfected cells would be induced to secrete TRAIL into the tumor microenvironment. To enable effective delivery of plasmid DNA encoding *TRAIL* into glioblastoma (GBM), we develop a targeted iron oxide NP coated with chitosan-polyethylene glycol-polyethyleneimine copolymer and chlorotoxin (CTX), and evaluate its effect in delivering *TRAIL in vitro* and *in vivo*. NP-TRAIL successfully delivers *TRAIL* into human T98G GBM cells and induces secretion of 40 pg/ml of TRAIL *in vitro*. Transfected cells show 3-fold increased apoptosis as compared to the control DNA bound NPs. Systemic administration of NP-TRAIL-CTX to mice bearing T98G derived flank xenografts delays tumor growth by 60 mm^3 and induces apoptosis in tumor tissue. Our results suggest that NP-TRAIL-CTX could potentially serve as a targeted anticancer therapeutic for more efficient TRAIL delivery to GBM.

3.1 INTRODUCTION

Glioblastoma (GBM) is the most common and deadly primary brain tumor in humans [77]. Even with aggressive surgical resection combined with radio-chemotherapy, the prognosis for GBM patients remains dismal with a median survival of approximately 14 months after initial diagnosis [78, 79]. The highly invasive and infiltrative nature of GBM prevents complete resection and the inherent resistance to current radiation and chemotherapeutic agents limits their usefulness as adjuvant therapies [80].

Gene therapy is considered to hold unique promise to overcome treatment resistance [81-83]. Suicidal genes or genes expressing therapeutic proteins and pro-drug activated enzymes

such as Bcl-2-related protein, herpes simplex virus type-1 thymidine kinase, bone morphogenetic protein 2, cytosine deaminase, and human tumor necrosis factor α-related apoptosis-inducing ligand (TRAIL), have attracted research interests due to their capacity in inducing apoptosis in cancer cells [27-29]. TRAIL is a strong candidate for GBM treatment because the majority of GBM express death receptors (DRs) [84], and recombinant TRAIL displays good tolerability in preclinical and early-phase clinical studies [85, 86]. Importantly, early-phase clinical trials demonstrated that it has no negative effect on non-neoplastic tissue [87-90]. In addition, TRAIL has shown a therapeutic effect when combined with chemo or radio-therapy in preclinical studies [49, 91].

Much effort has been devoted on delivering recombinant TRAIL using cell-based vehicles and vectors at nanoscale or microscale, but the translation of TRAIL-based therapies into clinical use for GBM treatment remains limited by the failure to deliver sufficient protein into the tumor to generate a therapeutic effect [92-94]. TRAIL gene therapy can potentially overcome this limitation by delivering *TRAIL* encoding DNA specifically to tumor cells so that they express and secrete this therapeutic protein into the tumor microenvironment [95, 96]. This strategy has been utilized in treating several types of cancer using both viral and non-viral based vectors [97, 98]. However, gene delivery to GBM is still hindered by low *in vivo* gene transfection efficiency with most delivery vehicles, especially with the presence of the blood-brain barrier (BBB) that has to be overcome before any therapeutics can reach tumor sites in the brain [99].

With this in mind, we designed a nanoparticle (NP) delivery vehicle for targeted gene transfection in GBM cells. The NP is comprised of an iron oxide core coated with a shell of chitosan-polyethylene glycol (PEG) grafted polyethyleneimine (PEI) copolymer (CP-PEI) and conjugated with chlorotoxin (CTX). Iron oxide is used as the core material because of its biocompatibility, biodegradability, and intrinsic superparamagnetic properties, and can serve as a magnetic resonance imaging (MRI) contrast agent for disease diagnosis and treatment monitoring [100, 101]. Chitosan is a natural polymer derived from crustacean shells and has ample functional groups allowing for attachment of functional ligands [6]. The PEG grafted chitosan (herein termed CP) serves as a stabilizer that prevents particle agglomeration and leads to excellent biodistribution and blood half-life [8]. We previously demonstrated that CP-PEI based NPs can effectively complex and deliver plasmid DNA to GBM cells *in vitro* and *in vivo* [102]. These NPs were derivatized with CTX to enhance their affinity towards GBM by binding

to cell surface lipid rafts containing MMP-2 and Annexin A2 [103, 104], and increase the *in vivo* transfection efficiency of gene delivery NPs [6]. Furthermore, CTX can promote BBB penetration through receptor-mediated transcytosis [8, 105]. In this study, we use the same CP-PEI based NPs to deliver *TRAIL* encoding plasmid DNA to study its efficacy in treating GBM. We first characterized the physicochemical properties of the NPs. We then examined the effect of NP bound *TRAIL* (NP-TRAIL) on cell viability and apoptosis in human T98G GBM cells *in vitro*, and the ability of CTX conjugated NP-TRAIL (NP-TRAIL-CTX) to induce apoptosis and reduce the tumor growth of T98G derived flank xenografts in mice *in vivo*.

3.2 EXPERIMENTAL

3.2.1 Materials

All chemicals were purchased from Sigma-Aldrich unless otherwise specified. All tissue culture reagents were purchased from Life Technologies unless otherwise specified.

3.2.2 Plasmid DNA Preparation

The plasmid pEGFP-TRAIL was purchased from Addgene (plasmid # 10953) [106]. It was propagated in DH5α *E. Coli* and purified using the Plasmid Giga Kit (Qiagen). Salmon DNA purchased from Sigma-Aldrich was used as the control plasmid DNA.

3.2.3 NP Synthesis

Chitosan-PEG (CP), chitosan-PEG-PEI copolymers (CP-PEI), and iron oxide nanoparticles with a siloxane PEG monolayer (IOSPM) were synthesized as described previously [107, 108]. The IOSPM was coated with CP-PEI copolymer through crosslinking N-succinimidyl iodoacetate (SIA) and 2-Iminothiolane (Traut's regents) (Molecular Biosciences) before purification using a S-200 sephacryl resin (GE Healthcare) equilibrated with 20 mM HEPES buffer (pH 7.4). NPs were complexed with plasmid DNA at a NP:DNA weight ratio of 1:2 (iron mass:DNA mass) prior to CTX attachment using SIA and Traut's reagent.

3.2.4 NP Characterization

For transmission electron microscopy (TEM) analysis, 5 µL of the NP-TRAIL-CTX (60 µg/mL) were placed on a formvar/carbon coated 300 mesh copper grid (Ted Pella). After 5 min, NP solution was removed and the grid was allowed to dry overnight before imaging using a Tecnai G2 F20 transmission electron microscope (FEI) operating at a voltage of 200 kV. All hydrodynamic size and zeta potential analyses were acquired in HEPES buffer (pH 7.4) using a DTS Zetasizer Nano analyzer (Malvern Instruments).

DNA binding was characterized using gel retardation assay. NP-TRAIL and NP-TRAIL-CTX were prepared by mixing 0.5 µg NP with 1 µg plasmid DNA in 60 µl of 20 mM HEPES buffer (pH 7.4). The complex was treated with heparin (50 µL of 1000 units/ml Heparin/1 µg DNA) and incubated for 30 min at room temperature to disrupt the electrostatic interaction between NP and DNA. Both heparin treated and untreated samples were subjected to electrophoresis on 1 % agarose gel for about 30 min at 120 V. Gels were stained with 0.5 µg/ml ethidium bromide and visualized using a Bio Rad Universal Hood II Gel Doc System.

3.2.5 Cell Culture

Human GBM derived T98G cells were purchased from American Type Culture Collection. T98G cells were grown in Dulbecco's Modified Eagle's Medium (DMEM) supplemented with 10 % FBS and 1 % penicillin/streptomycin (0.5 mg/ml) at 37 ℃ in a humidified atmosphere with 5 % CO_2. The medium was changed every 2–3 days.

3.2.6 In Vitro Gene Transfection

Twenty-four hours after plating T98G cells at a concentration of 25,000 cells/ml (1 ml/well) in 12 well plates, transfection was performed by replacing the cell culture medium with 1 ml of NP-TRAIL complex-containing medium (2 µg plasmid DNA per well). Four hours after transfection, the complex-containing medium was removed and replaced with fresh growth medium.

3.2.7 Quantitative RT-PCR (qRT-PCR)

RNA was extracted from T98G cells using the Qiagen RNeasy kit (Qiagen). cDNA was prepared using the iScript cDNA synthesis kit (Bio-Rad) following the manufacturer's protocol. Human β-actin served as a reference gene. SYBR Green PCR Master mix (Bio-Rad) was used for template amplification with a primer for each of the transcripts in a Bio-Rad CFX96 real-time PCR detection system. Quantitative amplification was monitored by the level of fluorescence reflecting the cycle number at the detection threshold (crossing point) using a standard curve. Thermocycling for all targets was carried out in a solution of 20 µl containing 0.2 µM primers (Integrated DNA Technologies) and 4 pg of cDNA from the reverse transcription reaction under the following conditions: 95 ℃ for 2 min, 40 cycles of denaturation (15 sec, 95 ℃), annealing (30 sec, 55 °C), and extension (30 sec, 72 °C). The primers are 5'-CGGTTCCGATGCCCTGAGGCTC-3'/5'- CGTCACACTTCATGATGGAATTG-3 and 5'-GTCTCTCTGTGTGGCTGTAAC-3'/5'-CTCTCTGAGGACCTCTT TCTCT-3' for β-actin and TRAIL, respectively.

3.2.8 Enzyme-Linked Immunosorbent Assay (ELISA)

Production of TRAIL protein levels following NP-TRAIL transfection in culture supernatants and cell lysates were measured by ELISA (Quantikine Human TRAIL Immunoassay; R&D Systems). Briefly, T98G cells were transfected with NP-TRIAL as described above. After 6-day incubation, medium was collected. Both supernatants and cell lysates were tested for TRAIL expression by following the manufacturer's specifications. Final color was evaluated at 450 nm (OD_{450}) on a microplate reader (Molecular Devices).

3.2.9 Cell Viability Assay

The Alamar blue (AB) assay was used to evaluate cell viability following the manufacture's protocol (Life Technologies). Briefly, T98G cells were plated and treated with NP-TRAIL as

previously described. Six days after treatment, cells were washed with Dulbecco's phosphate-buffered saline (DPBS) three times before adding 10% AB solution in complete growth medium to the wells. The samples were incubated at 37 ℃ for 2 hr. Then the AB solution was transferred to a 96-well plate, and fluorescence at an excitation wavelength of 556 nm and an emission wavelength of 586 nm was measured on a microplate reader (Molecular Devices).

3.2.10 Apoptotic Assay

The extent of apoptosis *in vitro* was determined by Annexin V and propidium iodide (PI) double staining using the Apoptotic, Necrotic & Healthy Cells Quantification Kit (Biotium). T98G cells were seeded on glass coverslip one day prior to treatment. Then, the cells were treated with NP-TRAIL or NP-control as described previously. Six days after NP treatment, cells were collected and washed with DPBS. Annexin V binding buffer (500 µl) mixed with 5 µl Annexin V-fluorescein isothiocyanate (FITC) and PI was added to cells, followed by incubation at room temperature in the dark for 15 min. The stained cells were then stained by DAPI to indicate nucleus, and visualized using a Nikon ECLIPSE TE2000-S microscope.

For flow cytometric analysis, T98G cells were stained with Annexin V-FITC and PI following the same protocol and analyzed with a FACS Canto flow cytometer (BD Biosciences). Data were analyzed with FlowJo (Ashland).

3.2.11 Cell Cycle Distribution Analysis

Six days following NP-TRAIL treatment, cells were harvested, washed and fixed with 70% ethanol at 4 ℃ overnight, followed by treatment of 0.5 µg/ml RNase and 50 µg/ml PI at 4 ℃ for 3 hr. The cells were then analyzed for their DNA content using a BD FACS Canto flow cytometer (BD Biosciences). All data were analyzed with FlowJo (Ashland). Results are presented as percentages of cells in the various phases, G0/1, S, G2/M.

3.2.12 In Vivo Studies

All animal studies were performed in accordance with the University of Washington Office of Animal Welfare guidelines for the humane use of animals, and all procedures were reviewed and approved by the Institutional Animal Care and Use Committee. For the flank xenograft model, 6-week-old female NOD-SCID mice (Jackson Laboratories) were anesthetized using 1.5% inhaled isoflurane and 6×10^6 T98G cells in 150 μl of a 1:1 mixture of RPMI media and Matrigel (BD Biosciences) were injected subcutaneously into their right flank. Palpable T98G xenografts developed within 6 days and tumors were measured using an external caliper and the volume was calculated using the formula: $4\pi/3 \times (\text{length}/2) \times (\text{width}/2)^2$. Animals with 12 days-old xenografts (3 animals per group) were randomly divided into 3 groups: untreated, NP-control treated, and NP-TRAIL treated. Animals in the control group did not receive any treatment. Each animal in treated groups received one injection of NP-control or NP-TRIAL at 20 μg plasmid DNA. The treatment was terminated after 38 days; tumor tissues were harvested on day 9 and submitted for terminal deoxynucleotidyl transferase dUTP nick end labeling (TUNEL) staining.

3.2.13 Statistical Analysis

All of the data were statistically analyzed to express the mean ± standard deviation (SD) of the mean. Statistical significance was set at $p < 0.05$ and tested with Student's *t*-test.

3.3 RESULTS AND DISCUSSION

3.3.1 NP Development and Characterization

The physiochemical properties of NPs, such as size and surface charge, are key factors determining their pharmacokinetics. Therefore, hydrodynamic sizes and zeta potentials of NP (i.e., the base NP with no TRAIL and CTX loaded), NP-TRAIL, and NP-TRAIL-CTX were characterized using dynamic light scattering (DLS). Z-average diameters of NP and NP-TRAIL were 34.2 ± 5.4 nm and 50.0 ± 1.1 nm, respectively (**Figure 1a**). Sizes of NP-TRAIL slightly increased to 57.1 ± 1.4 nm after CTX conjugation. Importantly, the size of NP-TRAIL-CTX is

within the preferred range (10–100 nm) for *in vivo* navigation and evasion of reticuloendothelial system and renal clearance [109, 110].

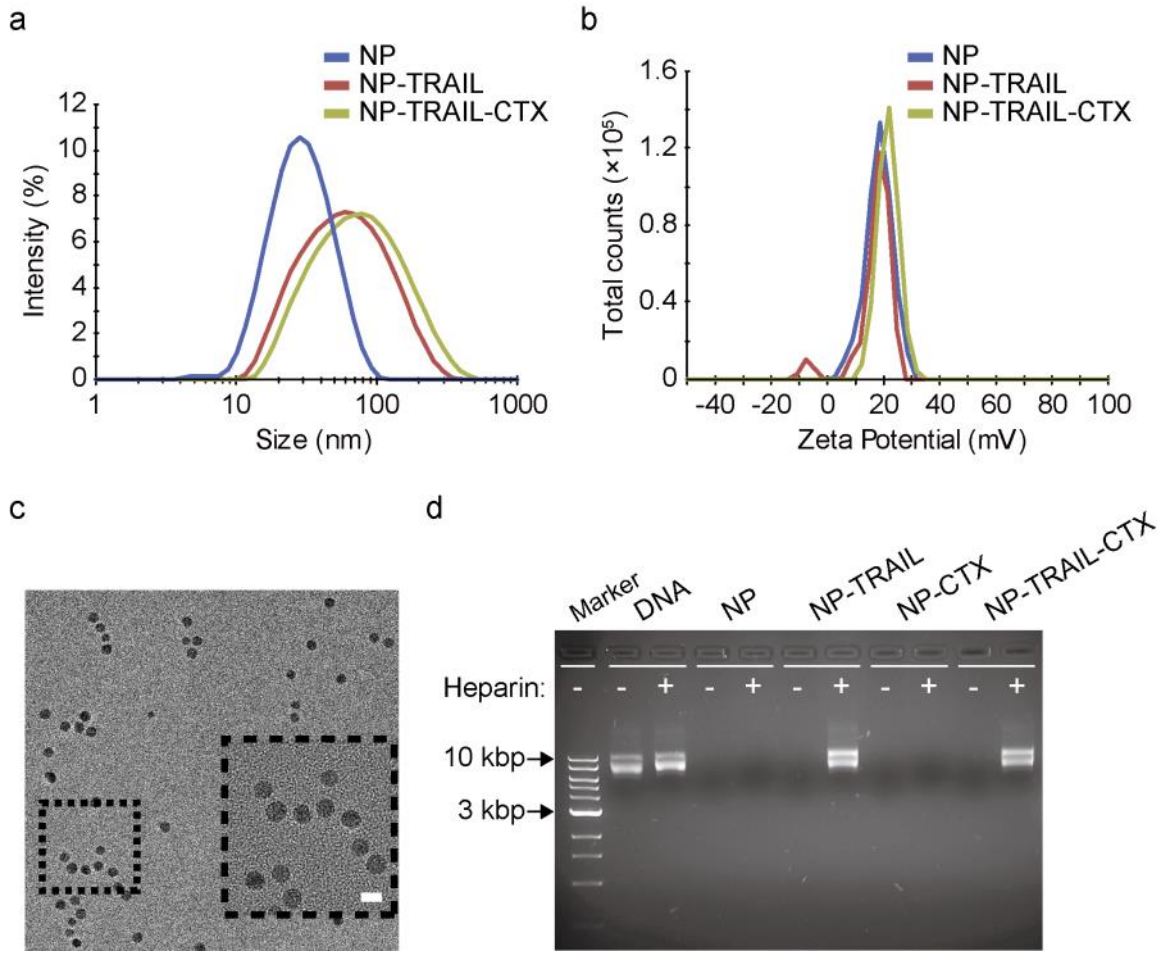

Figure 1. Physicochemical properties of NP-TRAIL-CTX. (a) Hydrodynamic size of NP, NP-TRAIL and NP-TRAIL-CTX in HEPES buffer (pH 7.4) determined by DLS. (b) Zeta potential of NP, NP-TRAIL, and NP-TRAIL-CTX in HEPES buffer (pH 7.4). (c) Representative TEM image of NP-TRAIL-CTX. Scale bar in the magnified image represents 10 nm. (d) Agarose gel image of naked *TRAIL* encoding plasmid DNA, NP, NP-TRAIL, NP-CTX, and NP-TRAIL-CTX with and without heparin treatment in the gel retardation assay. A 1 kb DNA Ladder was used as marker.

Zeta potential is another important physicochemical property for DNA delivery applications [111]. The positive surface charge correlates with the capacities of NPs to electrostatically complex, protect, and transfect plasmid DNA into cells. NP exhibited a zeta potential value of 17.75 ± 0.64 mV (**Figure 1b**). In agreement with the hydrodynamic size measurement, zeta potential was similar before and after CTX conjugation (16.70 ± 2.78 mV *vs.* 18.63 ± 1.27 mV), suggesting that CTX attachment does not compromise NP and *TRAIL* plasmid DNA complexation. TEM images revealed the spherical morphology and small size (10–12 nm) of the NP core (**Figure 1c**). Further, NP-TRAIL-CTX were well dispersed with no aggregation observed under TEM. This can be attributed to PEG coating on the surface of NPs and electrostatic repulsion between positively charged NPs. This suggests that DNA is fully incorporated within the polymer coating of a single NP rather than in aggregates of multiple NPs.

The ability of NPs to complex plasmid DNA was evaluated using a gel retardation assay where NPs bound DNA would not migrate down the gel. Naked plasmid DNA can freely migrate on agarose gel, whereas both NP formulations indicated complete binding of DNA as no DNA was observed in the gel (**Figure 1d**). After incubated with heparin, a competing reagent that disrupts the electrostatic interaction between DNA and NP, DNA became visible in both samples. This confirms DNA is bound within the NPs and CTX conjugation does not inhibit the complexing capacity of NPs. Taken together, the characterizations suggest that this NP system can potentially function well as a vehicle for delivery of plasmid DNA.

3.3.2 In Vitro Delivery of TRAIL

Efficacy of NP mediated delivery of *TRAIL* was evaluated *in vitro*. *TRAIL* encoding plasmid DNA was transfected in T98G cells using NP-TRAIL with NP loaded with salmon DNA as a control (NP-control). qRT-PCR revealed TRAIL mRNA only in NP-TRAIL transfected T98G cells as compared to untreated and NP-control treated cells (**Figure 2a**). Since TRAIL can be released as a soluble ligand, we also used an ELISA assay to evaluate the expression of TRAIL in cell culture supernatants. In agreement with the qRT-PCR measurement, NP-TRAIL treated cells produced 11.68 ± 0.13 pg of TRAIL in 300 µL cell culture medium 6 days after transfection, while no TRAIL expression was detected in either untreated or NP-control treated groups (**Figure 2b**). Moreover, ELISA revealed a 24-fold more TRAIL in cell culture medium

than that intracellularly (11.68 ± 0.13 *vs*. 0.49 ± 0.08 pg) indicating the vast majority of expressed TRAIL was secreted.

This is important for gene therapies since secreted therapeutic proteins could affect surrounding untransfected cells, which greatly reduces the transfection efficiency required to achieve a therapeutic effect. Previous studies have demonstrated that delivery of recombinant TRAIL using NPs can cause apoptotic activity of GBM [92]. In the current study, the concentration of secreted TRAIL is about 40 pg/ml, which is comparable with those reported in other studies where *TRAIL* was delivered by vehicles such as virus, neural stem cells, and lipofectamine [97, 112, 113]. Furthermore, multiple serial treatments required by recombinant TRAIL is not a necessity for our approach, which is preferable in clinical use.

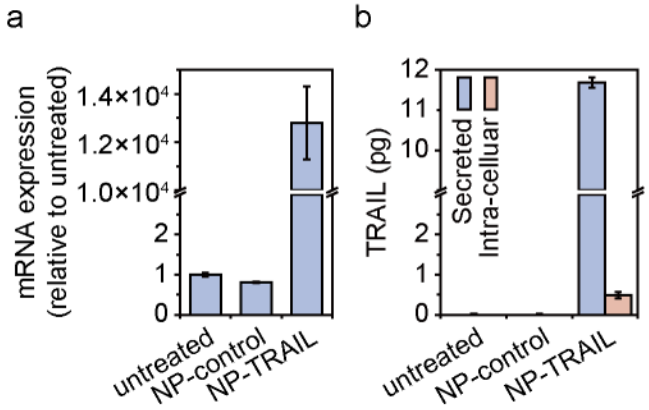

Figure 2. *In vitro* evaluation of TRAIL expression following NP-TRAIL treatment. (a) T98G cells were transfected with NP-TRAIL, with untreated cells and NP-control treated cells as controls. TRAIL mRNA expression was quantified by qRT-PCR at 6 days after transfection. (b) At day 6 after NP-TRAIL treatment, the concentration of secreted TRAIL in culture supernatant and intra-cellular TRAIL was analyzed by ELISA.

3.3.3 In Vitro Toxicity of NP-TRAIL to Human GBM Cells

Having demonstrated NP-mediated *TRAIL* gene delivery and expression in T98G cells, we investigated the therapeutic effects of NP-TRAIL *in vitro*. Six days post-transfection, cell viability was tested using the Alamar blue (AB) assay (**Figure 3a**). As expected, NP-control

showed little toxicity with approximately 81.9 ± 3.0 % viability. As a comparison, NP-TRAIL led to greatly reduced cell viability (51.4 ± 1.9 %). The AB results were also corroborated by optical imaging of cells shown in **Figure 3b**. Untreated and NP-control treated T98G cells exhibited similar normal cell morphologies whereas NP-TRAIL treated cells had significantly lower cell numbers and dramatic toxicity can be directly visualized.

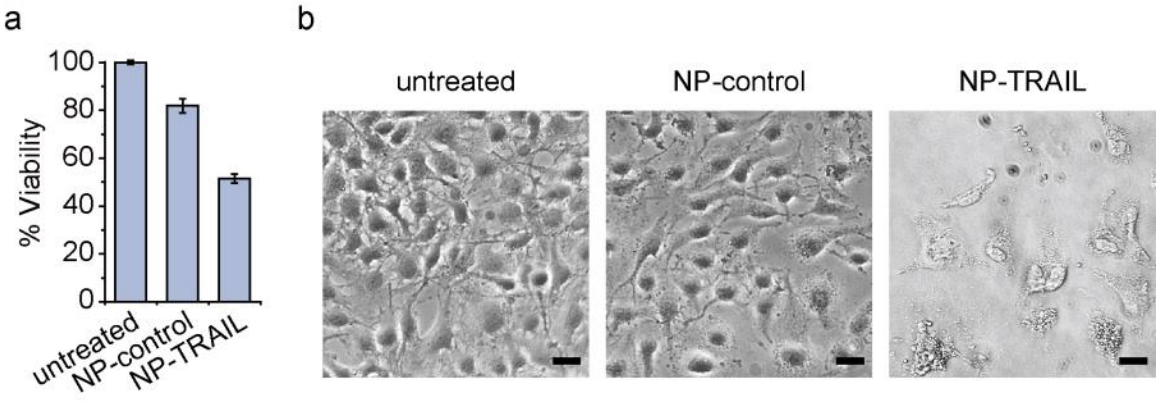

Figure 3. TRAIL gene therapy induces cellular toxicity *in vitro*. (a) Viability of T98G cells on day 6 post-transfection as determined by AB assay. (b) Bright-field microscopy images of transfected T98G cells on day 6 post transfection. Scale bars correspond to 10 μm.

3.3.4 Apoptotic Effect of NP-TRAIL on GBM Cells In Vitro

We examined the degree of apoptosis in T98G cells using Annexin V-FITC and PI double-staining. In accordance with the cell viability measurement, NP-TRAIL treated cells showed positive staining for both Annexin V-FITC and PI by fluorescence microscopy (**Figure 4a**). As a comparison, no fluorescence signal was detected from either the untreated or NP-control treated cells. Additionally, DAPI staining showed significant nuclear fragmentation in NP-TRAIL treated cells whereas untreated and NP-control treated cells showed little evidence of apoptosis. Quantification of apoptosis using flow cytometry revealed a 47.9 ± 3.2 % apoptotic cell population by NP-TRAIL transfection. In contrast, untreated and NP-control treatment showed 13.1 ± 3.4 % and 17.9 ± 2.6 % Annexin V-FITC and PI double positive populations (**Figure 4b and c**).

The *TRAIL* encoding plasmid DNA used here is expressed as a fusion with EGFP, which was shown to not affect its therapeutic efficacy [106]. In order to examine if EGFP expression has a negative effect on Annexin V-FITC staining, flow cytometry and microscopy analysis was conducted on NP-TRAIL treated T98G cells with and without Annexin V-FITC labeling. Both assays revealed that green fluorescence intensity of NP-TRAIL transfected cells after 6 days were similar with untreated T98G cells (**Figure 5a**). We believe that EGFP expression had receded into background color 6 days after NP-TRAIL transfection because of plasmid DNA dilution through cell division and impairment as the majority of T98G cells underwent apoptosis. Therefore, the green fluorescence intensity of EGFP was significantly lower than that from Annexin V-FITC labeled NP-TRAIL treated cells (**Figure 5b)**, which demonstrates the reliability of the apoptosis analysis results.

The effect of NP-TRAIL on cell cycle progression in GBM cells was also examined. Six days after transfection with NP-TRAIL, T98G cells were labeled with PI and the DNA content was analyzed using flow cytometry. As shown in **Figure 6**, NP-TRAIL treatment caused an increase in the proportion of cells in the G2-M phase (54.6% *vs*. 20.8% for untreated and 13.7% for NP-control) and a corresponding decrease in the proportion of cells in the S and G1 phases. This G2-M cell cycle arrest in NP-TRAIL treated cells is in agreement with the apoptosis results and provides further evidence of NP-TRAIL treatment efficacy in GBM cells.

TRAIL is an attractive anticancer agent due to its ability to induce apoptosis in a variety of tumor cell types including GBM [47-49, 92]. In line with these studies, NP-TRAIL caused cytotoxicity occurred through induction of the apoptosis in GBM cells. In fact, TRAIL can activate both extrinsic and intrinsic mitochondrial apoptotic pathways in T98G that was identified as a p53 mutant cell line [45, 114-116]. In the current study, cell cycle status was analyzed 6 days after NP-TRAIL treatment rather than 24 hr or 48 hr, the duration that were used for apoptosis characterization in other studies [117, 118]. At this late stage at 6 days, apoptosis might also rely on the intrinsic mitochondrial apoptotic pathway, accompanied by p53 associated G2-M phase cell cycle arrest in response to DNA damage [119-123].

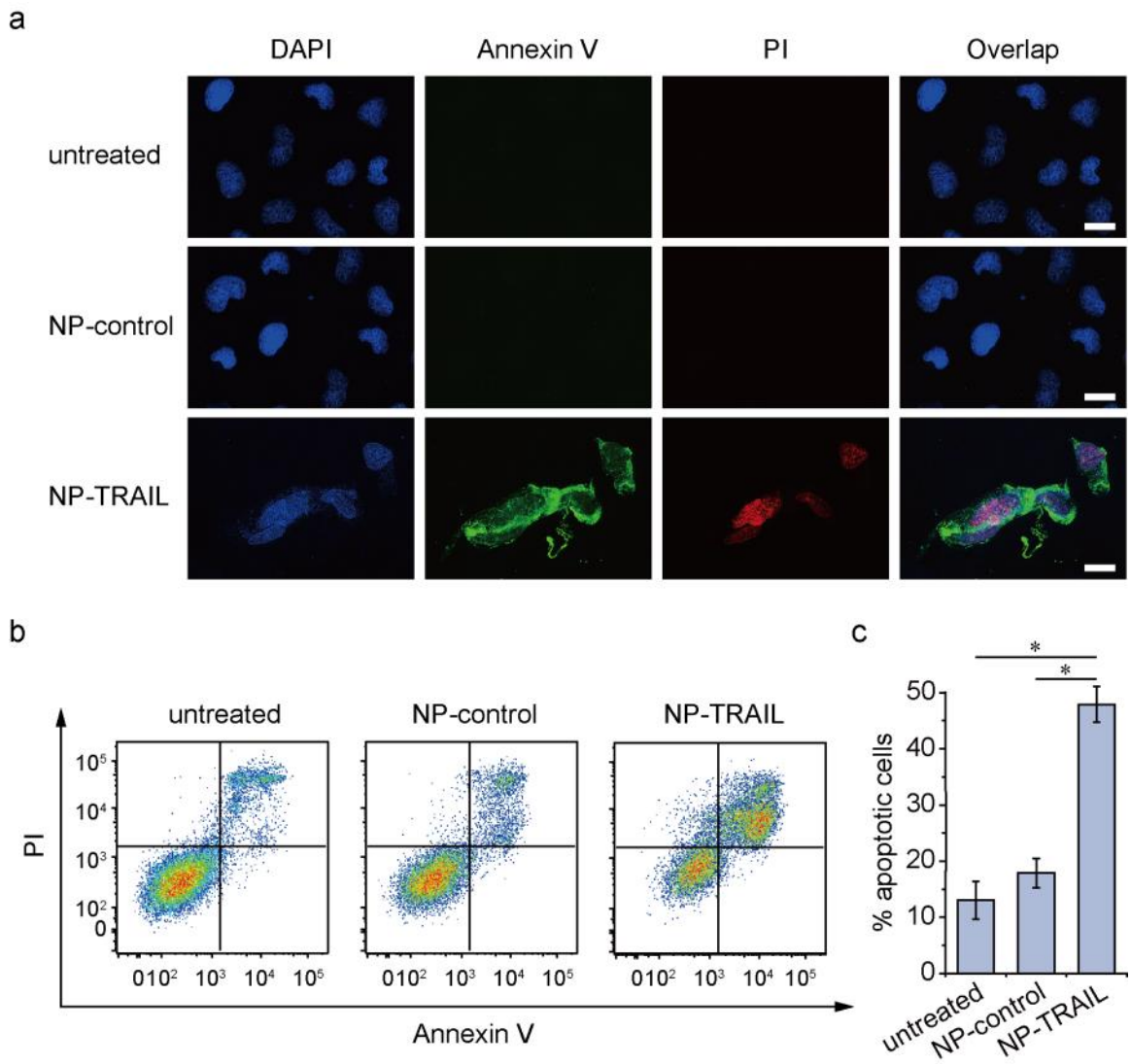

Figure 4. TRAIL gene therapy induces apoptosis in T98G cells *in vitro*. (a) Representative fluorescence images of T98G cells co-stained with Annexin V-FITC and PI 6 days following treatment. Scale bars represent 10 μm. (b) Apoptosis analysis of T98G cells with flow cytometry 6 days after NP-TRAIL treatment. (c) Quantification of Annexin V-FITC and PI positive apoptotic cell populations from panel b. Data are from three independent experiments. ∗ represents $p < 0.01$.

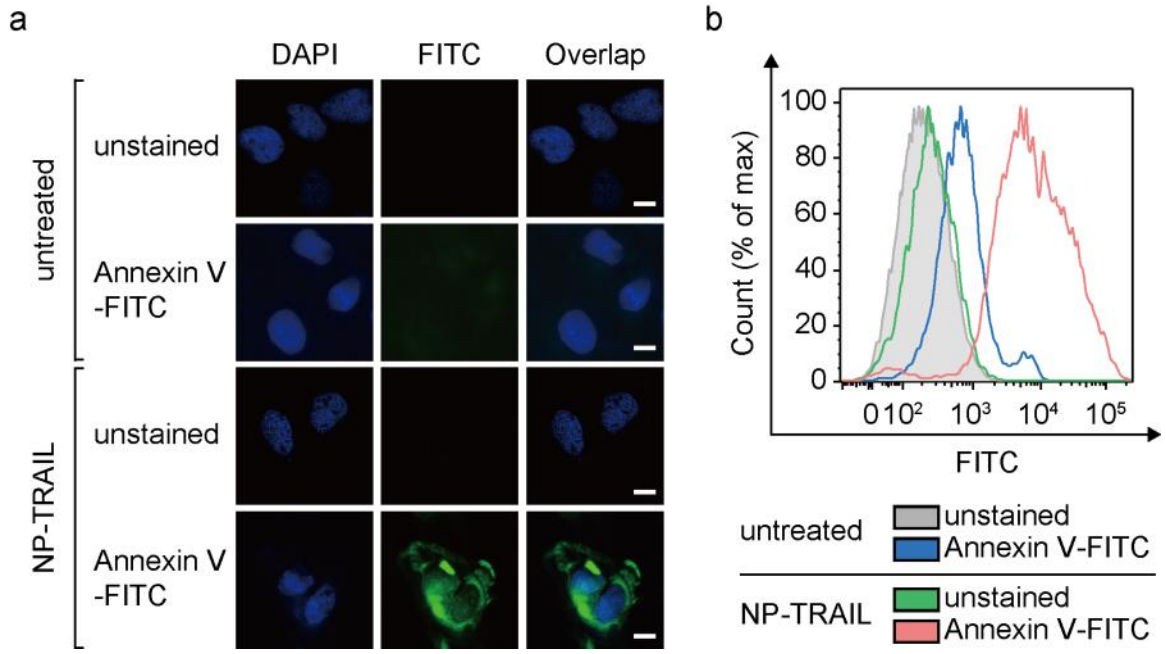

Figure 5. Elimination of false positive effect of GFP expression on Annexin V-FITC staining. (a) Representative fluorescence images of T98G cells stained with Annexin V-FITC 6 days following NP-TRAIL treatment. Scale bars represent 10 μm. (b) Flow cytometric analysis of T98G cells from panel a.

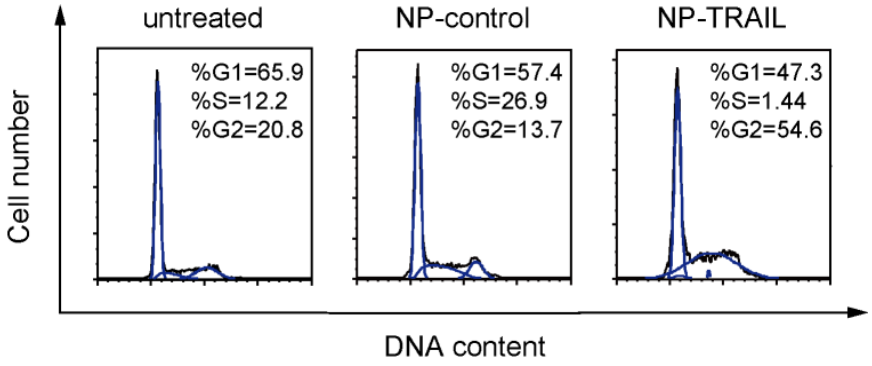

Figure 6. Representative cell cycle phase distribution of T98G cells 6 days after NP-TRAIL transfection. Results were the average of three independent experiments.

3.3.5 In Vivo Antitumor Effect of NP-TRAIL-CTX

The therapeutic efficacy of NP delivery of *TRAIL* encoding plasmid DNA was determined *in vivo* by treating athymic nude mice harboring T98G flank tumors with NP-TRAIL-CTX or NP-control-CTX. Here, CTX was attached to the NP as it is crucial to incorporate targeting agents on the surface of gene delivery vehicles in order to improve *in vivo* transfection efficiency specifically in the tumor [124, 125]. Our previous studies show that conjugating CTX to the surface of NPs increases NP distribution throughout the tumor and *in vivo* transfection efficiency [6, 70]. Mice treated with NP-TRAIL-CTX showed rapid shrinkage in tumor size followed by slow growth whereas mice treated with NP-control-CTX showed a consistent increase in tumor size over time (**Figure 7b**). This suggests that the NPs were able to deliver TRAIL encoding plasmid DNA into tumor cells for TRAIL expression, secretion, and induction of apoptosis.

To determine the degree of apoptosis caused by NP-TRAIL-CTX treatment, xenograft tumors were collected 9 days after NP injection, and apoptosis analyzed through TUNEL staining. NP-TRAIL-CTX induced more apoptosis as compared to NP-control-CTX as evidenced by the large number of TUNEL-positive tumor cells (**Figure 7c**). This correlates well with the *in vitro* apoptosis results and shows the ability of the NPs to deliver *TRAIL* gene to tumors for expression and subsequent promotion of apoptosis in transfected and surrounding cells (**Figure 7a**). The high level of apoptosis in tumor tissues induced by NP-TRAIL-CTX administration suggests that this strategy has clinical potential for GBM treatment.

Targeted gene delivery is crucial for gene therapy and much efforts have been devoted to improve efficient NP targeting and penetration into tumors. The targeting capacity of CTX to human brain tumors by binding to MMP-2 and Annexin A2 is well established by previous studies [6, 103, 104, 126]. Moreover, Annexin A2 has been identified highly expressed on the surface of neovasculature [127-130]. This could provide an additional target for TRAIL delivery as endothelial cells that were targeted with NP-TRAIL-CTX could also produce TRAIL and secrete it into the tumor microenvironment. Here, we have also incorporated another level of targeting by using TRAIL, as its therapeutic effect is specific to tumor cells [131]. Therefore, even if NP-TRAIL-CTX were taken up to a significant degree by any off-target tissue, no negative response to TRAIL expression would be expected.

Another big impediment to the clinical translation of TRAIL therapeutics lies in the heterogenetic resistant of tumors to TRAIL, which is due to the expression of decoy receptors and several internal countervail cell signaling [114, 132, 133]. Our NP system is ideal in overcoming these obstacles by co-delivery of *TRAIL* and inhibitors of the resistant mechanisms. Furthermore, our treatment can be combined with other gene therapeutics targeting multiple signaling pathways for a synergetic efficacy.

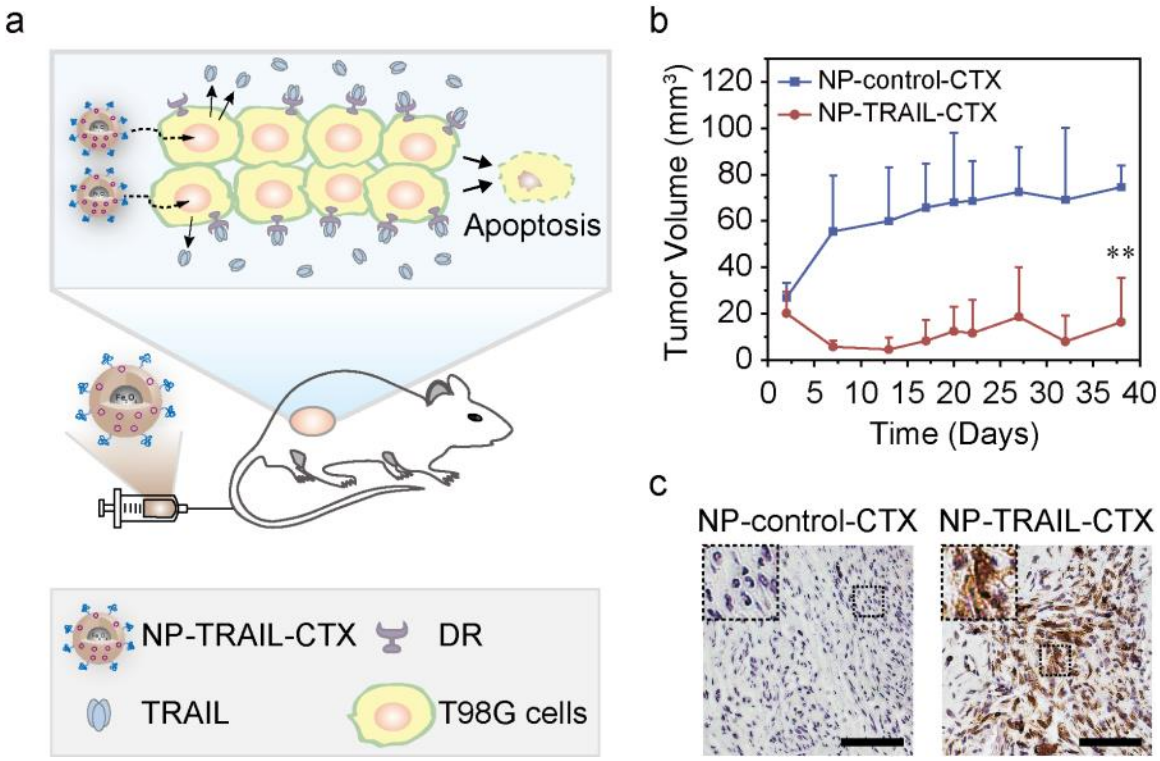

Figure 7. NP-mediated TRAIL gene delivery shows therapeutic efficacy *in vivo*. (a) Schematic of mice subjected to one injection of NP-TRAIL-CTX. (b) Volumes of T98G flank xenograft tumors of mice treated with NP-TRAIL-CTX and NP-control-CTX once tumor became palpable. All values are mean ± SD of determinations made in 3 animals. ** indicates $p < 0.05$. (c) TUNEL staining revealed significant apoptosis in tumors from NP-TRAIL-CTX treated mice. Scale bars represent 200 μm.

3.4 CONCLUSIONS

In this study we developed a CTX activated iron oxide NP coated with chitosan-PEG-PEI copolymer with appropriate properties for plasmid DNA delivery to tumor. We demonstrated that NPs loaded with the *TRAIL* gene are able to transfect GBM cells to express and secrete sufficient quantities of TRAIL to promote apoptosis *in vitro*. Importantly, we found that NP-mediated TRAIL gene delivery in a GBM flank xenograft mouse model induced significant apoptosis in the tumor and effectively reduced tumor burden. These results suggest NP-TRAIL-CTX as a potential strategy for improving localized delivery of TRAIL to GBM.

4. DEVELOPMENT OF IRON OXIDE-BASED NANOVECTOR FOR TUMOR TARGETED SIRNA DELIVERY

Hepatocellular carcinoma (HCC) is one of the deadliest cancers worldwide. Small interfering RNA (siRNA) holds promise as a new class of therapeutics for HCC as it can achieve sequence-specific gene knockdown with low cytotoxicity. However, the main challenge in the clinical application of siRNA lies in the lack of effective delivery approaches that need to be highly specific and thus incur low or no systemic toxicity. Here, we present a non-viral nanoparticle-based gene carrier that can specifically deliver siRNA to HCC. The nanovector (NP-siRNA-GPC3 Ab) is made of an iron oxide core coated with chitosan-PEG grafted PEI copolymer, which is further functionalized with siRNA and conjugated with a monoclonal antibody (Ab) against human glypican-3 (GPC3) receptor highly expressed in HCC. A rat RH7777 HCC cell line that co-expresses human GPC3 and firefly luciferase (Luc) is established to evaluate the nanovector. The nanoparticle-mediated delivery of siRNA against Luc effectively suppresses Luc expression *in vitro* without notable cytotoxicity. Significantly, NP-siLuc-GPC3 Ab administered intravenously in an orthotopic model of HCC is able to specifically bound to tumor and induce remarkable inhibition of Luc expression. Our findings demonstrate the potential of using this nanovector for targeted delivery of therapeutic siRNA to HCC.

4.1 INTRODUCTION

Hepatocellular carcinoma (HCC) is the second-leading cause of cancer-related deaths worldwide, resulting in more than one million deaths annually [134, 135]. Despite its global significance, HCC is understudied compared with other major lethal types of cancer in the US. Although potentially curative treatments such as surgical resection, ablative therapies, and liver transplantation exist [136], the prognosis remains poor as the majority of patients are diagnosed at an advanced stage and are not candidates for such therapies [135, 137], Sorafenib, a small molecule tyrosine kinase inhibitor, is currently the only drug approved for the treatment of patients with advanced HCC. However, it prolongs survival by a mere 2–3 months, and has dose-

limiting side effects [138-141]. Thereby, there is an urgent need for more effective therapeutic approaches for these patients.

RNA interference (RNAi) mediated by small interfering RNA (siRNA) can silence gene expression in a highly specific manner, and thus holds great promise as a potent inhibitor of therapeutic targets with low toxicity and a high degree of specificity that is far superior to conventional drugs [21-23]. In fact, many aberrant signal transduction pathways that are associated with tumorigenesis and *chemotherapy* resistance in HCC have been identified, and RNAi utilized to suppress these targets exhibited encouraging therapeutic effects [142-144]. Although siRNA is powerful gene regulation agents, the efficiency of systemic delivery of siRNA is extremely low due to quick degradation in biological fluids, poor cellular uptake resulted by the inherent physicochemical characteristics of siRNA (i.e., high molecular weight, negative charge, and stiff structure), and inefficient intracellular trafficking to escape from endosomes and release of siRNA in cytoplasm [145-147].

Nanoparticles as carriers for systemic delivery of synthetic siRNA have gained significant attention [21, 69]. Several nanoscale constructs have been investigated for siRNA delivery to HCC, including cationic polymers, lipid-based, and superparamagnetic nanoparticles [148-153]. Despite many nanoparticle systems have shown promise *in vitro* for targeting tumor cells, their *in vivo* applications and clinical utility have been hindered because of limited potency and poor target specificity, resulting in an unacceptable level of systemic toxicity [69, 154]. As carriers for siRNA delivery, nanoparticles are required to protect siRNA from degradation during transport and overcome extra- and intra- cellular barriers for specific site functions [69]. Compared to other tumors, target-specific delivery of nanoparticles to HCC is especially challenging. Liver cells are filtrated with a large number of Kupffer cells that will quickly take up these nanoparticles before they can reach tumors [110, 145]. In addition, the availability of HCC-specific targeting ligands remains limited although research in finding targeting moieties that recognize HCC-specific cell receptors has been actively pursued in the past decade [149, 155-158].

In this study, we present a theranostic nanovector (NP-siRNA-GPC3 Ab) and demonstrated that it can specifically and effectively deliver siRNA to HCC through systemic injection in an orthotopic xenograft mouse model. The NP-siRNA-GPC3 Ab is made of an iron oxide core coated with chitosan-PEG grafted polyethyleneimine (PEI) copolymer (CP-PEI) shell and

conjugated with a monoclonal antibody (Ab) against human glypican-3 (GPC3) receptor. An iron oxide-based nanoparticle formulation is used here because of its biocompatibility, biodegradability, and inherent superparamagnetic properties that can serve as a magnetic resonance imaging (MRI) contrast agent for disease diagnosis and treatment monitoring, as demonstrated in our previous studies using the same nanoparticle synthesis strategy [6, 70, 100, 158]. Chitosan, a natural polymer derived from crustacean shells, has ample functional groups allowing for attachment of functional ligands and cationic polymers for complexing siRNA [159, 160]. The PEG grafted chitosan (herein termed CP) serves as a stabilizer that prevents particle agglomeration. CP-PEI copolymer coated iron oxide nanoparticles has demonstrated their ability to protect siRNA from degradation and facilitate proper intracellular trafficking for safe and effective siRNA delivery [70]. GPC3 Ab is covalently attached to the surface of nanovector to confer the ability of HCC targeting. Recent studies have revealed that GPC3 is a promising receptor for HCC targeting as it is highly expressed in HCC but not in healthy tissues [161-163]. Notably, we have demonstrated the tumor specificity of GPC3 Ab [158], which has a very high binding affinity (~30 pM) and is internalized by HCC [164], making it an ideal targeting ligand. A rat RH7777 HCC cell line co-expressing human GPC3 and firefly luciferase (Luc) in orthotopic mouse model is used to evaluate tumor targeting and NP-siRNA mediated Luc gene silencing due to their ability to form tumors that represent histopathologic features of HCC.

4.2 EXPERIMENTAL

4.2.1 Materials

All chemicals were purchased from Sigma-Aldrich unless otherwise specified, and tissue culture reagents were purchased from Life Technologies unless otherwise specified.

4.2.2 Nanovector Synthesis

The preparation of NP-siRNA-GPC3 Ab is outlined in **Figure 8**. CP, CP-PEI copolymer, and iron oxide nanoparticles with a siloxane PEG monolayer (IOSPM) were synthesized as described previously [108, 165]. The IOSPM was coated with CP-PEI copolymer through crosslinking SIA

and Traut's regents (Molecular Biosciences) before purification using a S-200 sephacryl resin (GE Healthcare) equilibrated with 20 mM HEPES buffer (pH 7.4) (**Figure 8a**). IOSPM coated with CP-PEI copolymer, herein termed NP, were complexed with siRNA at weight ratio (Fe equivalent of NP:siRNA) of 1:2 in 20 mM HEPES buffer (pH 7.4), and incubated for 20 min at room temperature to allow formation of NP-siRNA complexes. Subsequently, GPC3 Ab was conjugated to NP-siRNA using a heterobifunctional PEG linker, NH_S-PEG_{12}-maleimide. Briefly, GPC3 Ab was reacted with excess Traut's reagent in thiolation buffer (pH 8.0) for 1 hr in the dark at room temperature to form Ab Traut's. Unreacted Traut's reagent was removed through Zeba spin columns (Life Technologies). NP-siRNA was reacted with NHS-PEG_{12}-maleimide (Life Technologies) in the dark at room temperature with gentle rocking for 30 min before removing unreacted linker through Zeba spin columns. The thiolated Ab was mixed with thiol-reactive NP-siRNA (2 mg Ab per 1 mg NP-siRNA) and allowed to react for 1 hr in the dark at room temperature with gentle rocking. Unreacted Ab was removed from NP conjugated Ab through size exclusion chromatography in S-200 sephacryl resin to obtain pure NP-siRNA-GPC3 Ab (**Figure 8b**).

4.2.3 Nanovector Characterization

For proton NMR (^{1}H-NMR) analysis, 50 µg (Fe) of IOSPM and NP were lyophilized to remove water. 30 µl of DCl and 870 µl of D_2O were added to the lyophilized NP to dissolve the iron core leaving free polymer coating in solution. 1.72 mg of trimethylsilyl propionate in 100 µl D_2O was added as internal reference. ^{1}H-NMR spectra were obtained using a Bruker Avance 300 spectrometer operating at 300 MHz (1H) and 325 K (number of scans = 128, acquisition time = 3s, delay (D1) = 1s).

For transmission electron microscopy (TEM) analysis, NP-siRNA-GPC3 Ab was diluted to 100 µg/mL in deionized water and 5 µL of the dilute solution were placed on a formvar/carbon coated 300 mesh copper grid (Ted Pella). After 5 min, the NP solution was removed and the grid was allowed to dry overnight before imaging using a Tecnai G2 F20 electron microscope (FEI) operating at a voltage of 200 kV. Hydrodynamic size and zeta potential analyses were acquired in HEPES buffer (pH 7.4) using a DTS Zetasizer Nano (Malvern Instruments).

GPC3 Ab after conjugated onto the NP-siRNA surface was detected by a sodium dodecyl sulfate polyacrylamide gel electrophoresis (SDS-PAGE) in comparison with free GPC3 Ab. A Precision Plus Protein™ Dual Color Standard (Bio-Rad) was used as molecular weight marker. The gel was run under reducing conditions by using a Mini PROTEAN 3 Cell electrophoresis unit (Bio-Rad) at a constant voltage mode of 100 V in a Tris/glycine/SDS buffer. The gel was then stained with Coomassie Brilliant Blue solution (Bio-Rad) and imaged with a Bio-Rad Universal Hood II Gel Doc System. NP-siRNA-GPC3 Ab was also evaluated for their possession of Ab by measurement of their absorption at $OD_{280\,nm}$ using a SpectraMax i3 *multi-mode* microplate reader (Molecular Devices).

siRNA binding was characterized using gel retardation assay. NP-siRNA complexes containing 1 μg siRNA were prepared at NP:siRNA weight ratios of 1:2 in 20 mM HEPES buffer (pH 7.4). The complex were treated with heparin (1000 units/ml, 50 μL Heparin/ 1 μg siRNA) and incubated for 30 min at room temperature to block the electrostatic interaction between NP and siRNA. Both heparin-treated and untreated complexes were loaded onto a native polyacrylamide gel for electrophoresis for about 30 min. After staining the gel with 0.5 μg/ml ethidium bromide, free-siRNA was detected using a Gel Doc XR (Bio-Rad).

4.2.4 Cell Culture

Rat RH7777 HCC cells were purchased from American Type Culture Collection (ATCC no. CRL-1601) and cultured at 37℃ in a humidified atmosphere with 5% CO_2 using Dulbecco's modified Eagle's Medium (DMEM) supplemented with 10% fetal bovine serum and 1% antibiotic-antimycotic.

GPC3 and Luc co-expressing RH7777 (RH7777-Luc-GPC3) cells were generated by transfecting previously established Luc-expressing RH7777 cells [163] with pLX304-BLAS-V5-GPC3 (Life Technologies) using Lipofectamine 2000 (Life Technologies) following the manufacture's protocol. Three days after transfection, regular DMEM was replaced by DMEM containing 2.5 μg/ml blasticidin. Cells were maintained in the selective medium for additional three weeks prior to sorting with a BD FACSAria™ II cell sorter (BD Biosciences). The stably transfected RH7777-Luc-GPC3 cells were cultured in complete medium supplemented with 2.5 μg/ml blasticidin.

Surface GPC3 antigen expression on the established RH7777-Luc-GPC3 cells was analyzed by flow cytometry. RH7777-Luc-GPC3 cells were incubated with mouse anti-GPC3 Ab (1 mg/ml, 1:50 dilution) at 4℃ for 30 min, and then probed with FITC conjugated rabbit anti-mouse secondary Ab (Abcam, 1:100 dilution) at 4℃ for 30 min. Cells were then washed, collected and analyzed with a FACSCanton™ II flow cytometer (BD Biosciences). Data were analyzed with FlowJo (Ashland).

4.2.5 In Vitro Cell Transfection

Twenty-four hours after plating RH7777-Luc-GPC3 cells at a concentration of 25,000 cells/ml, transfection was performed by replacing cell culture medium with 1 ml of NP-siRNA complex-containing medium (50 nmol siRNA per well). After 4 hr of transfection, NP-siRNA complex-containing medium was removed and replaced with fresh DMEM. Firefly luciferase gene-targeting siRNA (siLuc) and scramble siRNA (siScramble) were purchased from Dharmacon Research Inc.

Endosomal escape was evaluated using an endosomal integrity assay [166]. In brief, RH7777-Luc-GPC3 cells were co-incubated with NP-siRNA and membrane impermeable dye calcein (0.25 mM). Excess dye was washed off after 2 hr incubation. Cells were fixed and nuclei were stained with DAPI prior to imaging by fluorescence microscopy.

To evaluate NP-siRNA uptake, RH7777-Luc-GPC3 cells were transfected with NP complexed with Dy677-labeled siScramble (Dharmacon Research Inc). Twelve hours later, cells were fixed in 4% formaldehyde and nuclei were stained with DAPI prior to imaging using fluorescence microscopy.

4.2.6 Cell Viability Assay

The effect of NP-siRNA on RH7777-Luc-GPC3 cell viability was determined using the Alamar blue (AB) assay following the manufacture's protocol (Life Technologies). Briefly, cells were plated and transfected as described. After treatment, cells were washed with PBS three times before adding 10% AB solution in DMEM medium to the wells. Cells were incubated for 1 hr, then the AB solution was transferred to a 96-well plate, and the fluorescent emissions at an

excitation wavelength of 550 nm and an emission wavelength of 590 nm were read with a microplate reader.

4.2.7 Quantitative RT-PCR (qRT-PCR)

RNA was extracted from cells 48 hr after siRNA transfection using the Qiagen RNeasy kit. cDNA was prepared using the iScript cDNA Synthesis kit (Bio-Rad) following the manufacturer's protocol, which was then used as a template for PCR. qRT-PCR was used to evaluate the relative expression levels of Luc utilizing rat glyceraldehyde 3-phosphate dehydrogenase (GAPDH) as a control. SYBR Green PCR Master mix (Bio-Rad) was used for template amplification with a primer for each of the transcripts in a Bio-Rad CFX96 real-time PCR detection system. Quantitative amplification was monitored by the level of fluorescence reflecting the cycle number at the detection threshold (crossing point) using a standard curve. Thermocycling for all targets was carried out in a solution of 20 µl containing 0.5 µM primers (Integrated DNA Technologies) and 4 pg of cDNA from the reverse transcription reaction under following conditions: 95℃ for 2 min, 40 cycles of denaturation (15 sec, 95℃), annealing (30 sec, 58℃), and extension (30 sec, 72℃). The primers used for *GAPDH and Luc* were forward: 5'-GACATGCCGCCTGGAGAAAC-3'/reverse: 5'-AGCCCAGGATGCCCTTTAGT-3' and forward: 5'-ATTACACCCGAGGGGGATGA-3'/reverse: 5'-TCTCACACACAGTTCGCCTC-3', respectively.

4.2.8 Luc Activity Quantification

In vitro measurement of Luc activity was conducted using Luc assay following the manufacture's protocol (Promega). Briefly, 50,000 cells were collected and washed with PBS three times before lysed by 0.1% Triton-X. 200 µl of cell lysis were reacted with 50 µl luciferin, and read with a microplate reader. Protein was quantified by Bradford assay (Bio-Rad) following the manufacture's protocol.

4.2.9 Animal Model

All animal studies were performed in accordance with the University of Washington Office of Animal Welfare guidelines for the humane use of animals, and all procedures were reviewed and approved by the Institutional Animal Care and Use Committee. For the orthotopic xenograft model, 8-week-old female athymic Nu/J mice (Jackson Laboratories) were anesthetized using 1.5% inhaled isoflurane and the left lobe of the liver was exposed through an upper midline laparotomy. RH7777-Luc-GPC3 cells (1×10^6) in 50 μL of DMEM containing 50% Matrigel (BD Biosciences) were injected into the subcapsular space of the left lobe. Two weeks after injection, a 75 mg/kg intraperitoneal injection of VivoGlo luciferin (Promega) was administered and imaging was performed using an IVIS Lumina II system (PerkinElmer) to monitor the growth of intrahepatic tumors.

To analyze the GPC3 antigen expression on RH7777-Luc-GPC3 xenograft, tumors were harvested two weeks after implantation. Tumor cells were dissociated and passed through a 70 μm cell strainer (Thermo Fisher Scientific) to acquire single cell suspension. They were then subjected to anti-GPC3 Ab staining as described previously, and analyzed by flow cytometry using a FACSCanton™ II flow cytometer (BD Biosciences). Data were analyzed with FlowJo (Ashland).

4.2.10 Histological Analysis

After NP treatment, RH7777-Luc-GPC3 liver tumor tissues were fixed in 4% formaldehyde for 24 hr and placed in 30% sucrose until fully saturated. The tissues were subsequently cut into small pieces and frozen in OCT embedding medium (Sakura) at −80 ℃. Frozen sections (8 μm thickness) were stained with DAPI (Life Technologies) and photographed under a Zeiss 510 META confocal fluorescence microscope.

4.2.11 Statistical Analysis

All the data were statistically analyzed to express the mean value ± standard deviation (SD) of the mean. An unpaired, 2-tailed Student's *t* test was used, with a *P* value of less than 0.05 considered statistically significant.

4.3 RESULTS AND DISCUSSION

4.3.1 Nanovector Synthesis and Characterization

NP-siRNA-GPC3 Ab were synthesized as described in the previous section and illustrated in **Figure 8**. The presence of CP-PEI copolymer on iron oxide nanoparticles with a siloxane PEG monolayer (IOSPM) was verified by proton NMR (^{1}H-NMR) (**Figure 9a**). The characteristic ^{1}H-NMR peak at 3.65 ppm (peak I) representing ethylene group (–O–CH_2–CH_2–) of PEG is evidenced on the spectra of IOSPM and IOSPM coated with CP-PEI copolymer (herein termed NP). The ethylenimine (–NH_2–CH_2–CH_2–) repeat unit of PEI at 3.3–3.62 ppm (peak II) and the H3–6 peaks (peak III, δ = 3.68–3.73 ppm; peak IV, δ = 3.9–3.95 ppm) of chitosan on NP spectrum indicate the covalent attachment of CP-PEI on IOSPM. NP was complexed with siRNA at weight ratio (Fe equivalent of NP:siRNA) of 1:2, corresponding to approximately 300 siRNA molecules per NP as determined from calculations of molar masses of NP (~2,000,000 g Fe/mole NP) and siRNA (13,300 g/mole).

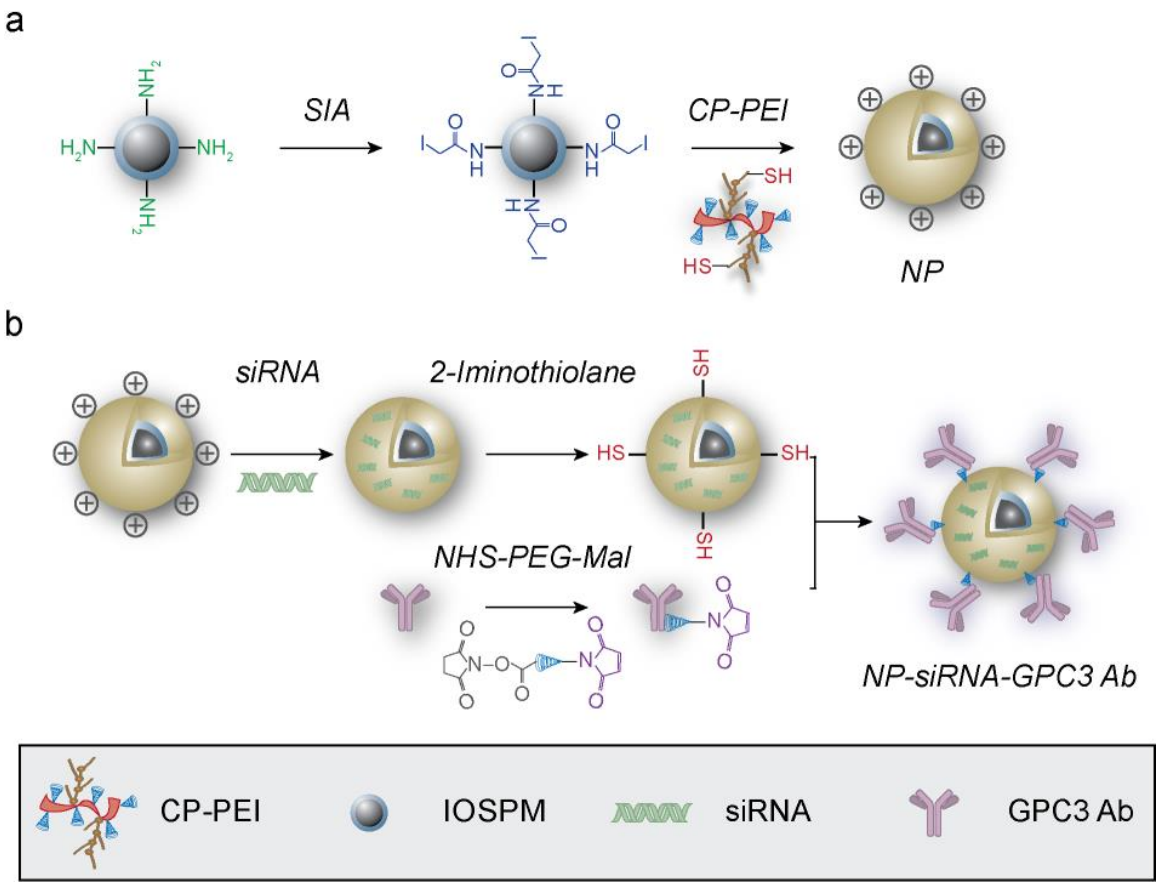

Figure 8. Schematic of NP-siRNA-GPC3 Ab synthesis. (a) Modification of IOSPM with CP-PEI to produce our NP. (b) NP-siRNA complexation and subsequent conjugation with GPC3 Ab to form fully functionalized NP-siRNA-GPC3 Ab.

Transmission electron microscopy (TEM) images in **Figure 9b** revealed a spherical morphology of the iron oxide core of NP-siRNA-GPC3 Ab with a size around 10–12 nm, confirming that the iron oxide core sizes remained uniform after copolymer conjugation. Additionally, NP-siRNA-GPC3 Ab was well dispersed in aqueous medium. SDS-PAGE was used to evaluate attachment of GPC3 Ab on NP-siRNA. As shown in **Figure 9c**, both light and heavy chains of Ab were detected from the purified NP-siRNA-GPC3 Ab under reducing conditions, which confirmed the conjugation of Ab to the NP. Band density quantification revealed there were approximately 26 Ab molecules per NP.

The NP core with copolymer coating of NP-siRNA-GPC3 Ab were characterized by dynamic light scattering (DLS). Both hydrodynamic sizes and zeta potentials of NP, NP-siRNA, and NP-siRNA-GPC3 Ab were determined (**Figure 9d**). No apparent change in size was observed after siRNA binding (39.87 ± 0.83 nm *vs.* 39.65 ± 0.70 nm), suggesting the strong complexing capacity of NP. NP slightly increased in size to 41.02 ± 0.41 nm after GPC3 Ab conjugation. The size of NP has a dramatic effect on nonspecific uptake by off-target cells in the body. In order to successfully reach the tumor site, NP has to overcome multiple physiological barriers including the liver, kidneys, and spleen. The hydrodynamic size of NP should be between 10–100 nm to avoid elimination by these organs [154]. Moreover, our NP-siRNA-GPC3 Ab is smaller than 60 nm, which is expected to have better penetration from blood vessels into tumor [167].

Zeta potential is another important physicochemical property for DNA/siRNA delivery applications [111]. The positive surface charge correlates with the capacities of NP to electrostatically complex and deliver siRNA into cells. Our base NP exhibited a zeta potential value of 27.85 ± 2.33 mV (**Figure 9d**). After siRNA complexation (NP-SiRNA), the zeta potential showed little change (27.30 ± 0.28 mV), consistent with the hydrodynamic size measurement which showed little change before and after siRNA complexation. After Ab attachment, the zeta potential of NP-siRNA-GPC3 Ab decreased to 22.85 ± 2.62 mV. This was likely caused by the addition of the PEG linker and Ab, which could both shield the charge of the NP.

The gel retardation assay was utilized to further demonstrate full siRNA binding in NP. As shown in the gel image (left panel of **Figure 10)**, the siRNA band was not visible when complexed with NP, suggesting the fully encapsulation of siRNA in the copolymer coating of the NP. siRNA was released from NP when treated with heparin, an electrostatic disrupting agent, as visualized by the siRNA band on the gel (right panel of **Figure 10**). Overall, the characterization of NP-siRNA-GPC3 Ab suggested that this NP system should function well as a vehicle for delivery of siRNA into HCC.

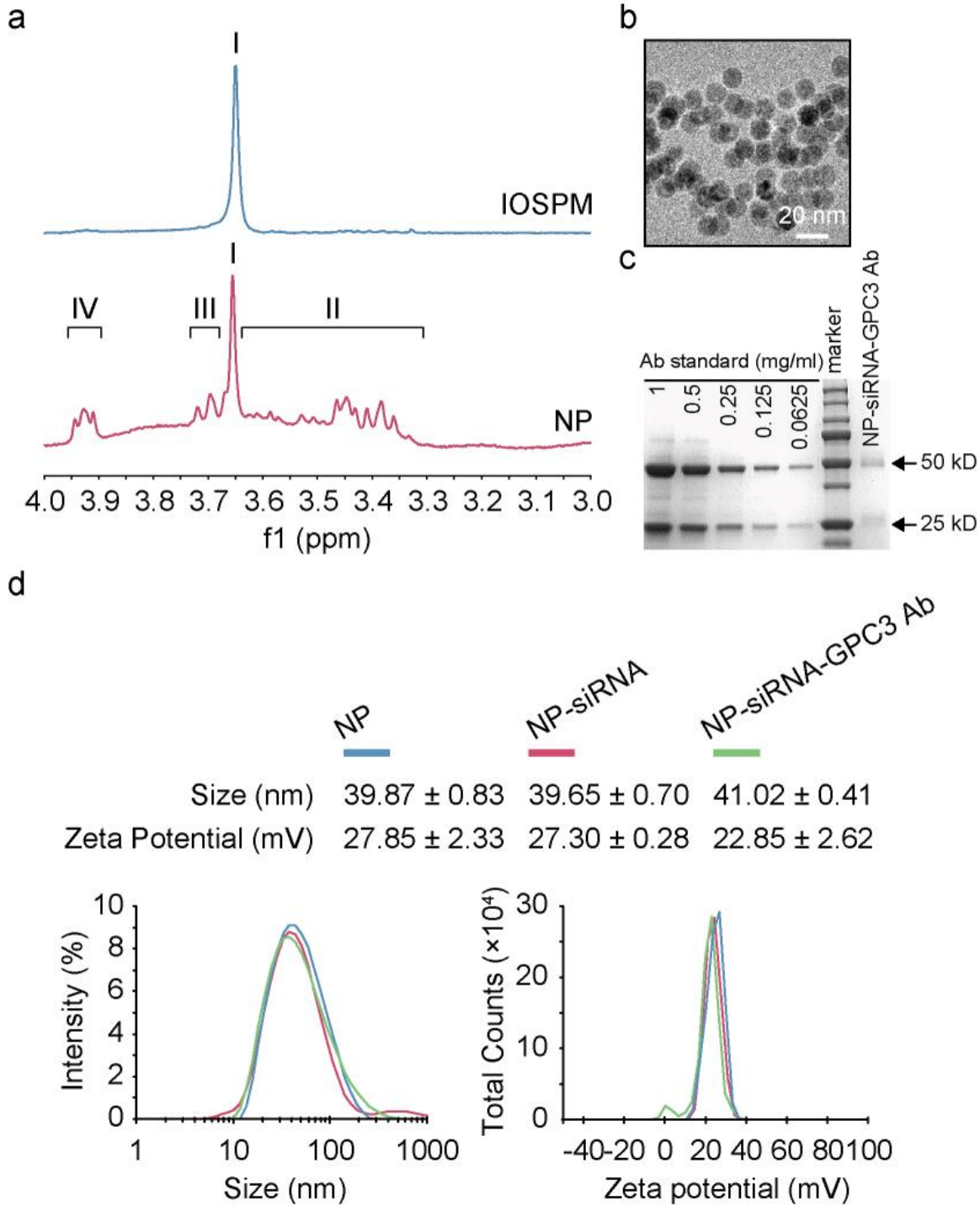

Figure 9. Characterization of NP-siRNA-GPC3 Ab. (a) 1H-NMR analysis of IOSPM and NP. The characteristic peak of the ethylene group of PEG (peak I) on IOSPM, the ethylenimine group of PEI (peak II), and 6 peaks of aldohexoses (peak III and IV) on chitosan were indicated on spectrum of NP. (b) TEM images of NP-siRNA-GPC3 Ab; scale bar = 20 nm. (c) SDS-PAGE

image showing the presence of Ab on NP-siRNA-GPC3 Ab with free Ab used as the standard. (d) Hydrodynamic size and zeta-potential of NP, NP-siRNA, and NP-siRNA-GPC3 Ab at pH 7.4 as determined by DLS.

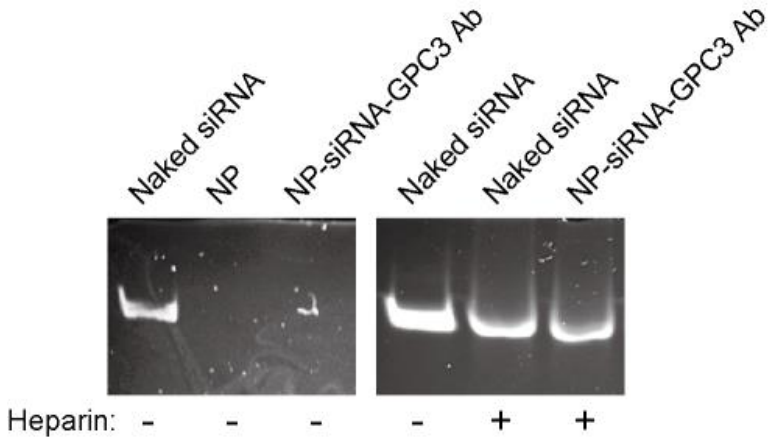

Figure 10. Evaluation of siRNA binding on NP using the gel retardation assay. Agarose gel images of naked siRNA, NP, NP-siRNA-PC3 Ab, naked siRNA with heparin, and NP-siRNA-GPC3 Ab with heparin. Development of GPC3 and Luc Co-Expressing RH7777 (RH7777-Luc-GPC3) Cells

To enable targeted siRNA delivery using our previously developed anti-GPC3 Ab [158], human GPC3 was stably transfected into RH7777 cells. Additionally, we stably transfected RH7777 cells with Luc for proof-of-concept knockdown experiments using our nanovector. RH7777 cells were chosen because of their ability to form tumors in the livers of athymic nude mice that represent histopathologic features of HCC.

Here we used siLuc as our therapeutic siRNA and scramble siRNA (siScramble) as control siRNA. Prior to evaluating *in vitro* and *in vivo* knockdown efficiency of NP-siLuc, expression level of Luc and GPC3 in the established RH7777-Luc-GPC3 cells were measured. The *in vitro* Luc assay revealed a 1224-fold higher luminescent signal in RH7777-Luc-GPC3 cells as compared to native RH7777 cells (**Figure 11a**). Surface expressed GPC3 antigen on RH7777-Luc-GPC3 cells were analyzed by flow cytometry. As shown in **Figure 11b**, flow cytometric analysis revealed a distinct GPC3 positive cell population with significantly higher fluorescence

intensity when compared to the unstained and non-targeting Ab controls. Taken together, these results verified the successful generation of a Luc and GPC3 co-expressing RH7777 cell line.

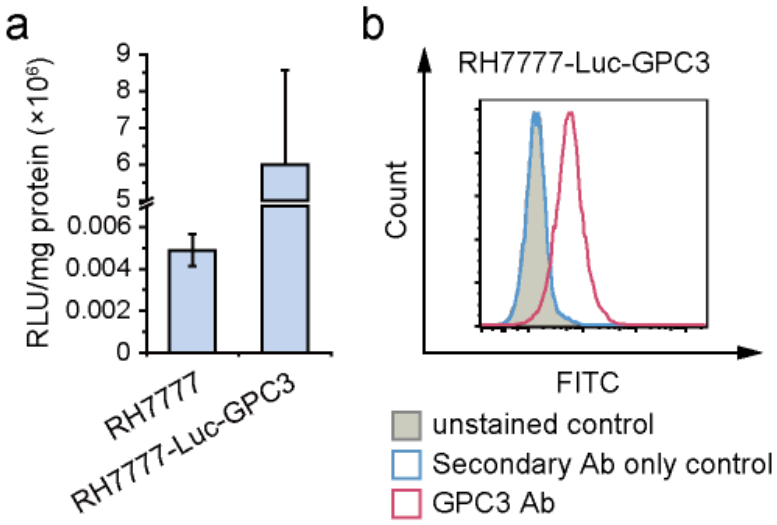

Figure 11. Characterization of RH7777-Luc-GPC3 cells. (a) Evaluation of Luc activity of RH7777-Luc-GPC3 cells using *in vitro* Luc assay, where native RH7777 cells served as negative control. (b) Flow cytometry analysis of GPC3 expression in RH7777-Luc-GPC3 cells. Filled peak represents unstained control. Histograms for secondary Ab control are also shown.

4.3.2 In Vitro Knockdown of Luc

After successfully establishing RH7777 cells that co-express Luc and GPC3, we evaluated gene-silencing efficacy of NP-siLuc *in vitro*. Forty-eight hours after NP-siLuc transfection, transient Luc expression in RH7777-Luc-GPC3 cells was measured at both mRNA and protein levels by quantitative RT-PCR (qRT-PCR) and Luc assays, respectively. As shown in **Figure 12a and b**, NP-siLuc exposure resulted in a 66% reduction in mRNA abundance, corresponding to a 79% suppression of Luc activity in RH7777-Luc-GPC3 cells. In contrast, no inhibition of Luc expression was observed from untreated or NP-siScramble treated cells.

Upon uptake by cells, NP-siRNA need to access cytoplasm to initiate RNAi. To further illustrate the mechanism of the nanovector-mediated gene knock-down, we investigated the escape of NP-siRNA from endosomes using an endosomal integrity assay [166]. Calcein

fluorescence (green) was barely detectable in RH7777-Luc-GPC3 cells indicating the integrity of endosomes while calcein fluorescence was observed throughout the cells contain both NP-siRNA and calcein (**Figure 12c**). Distribution of NP-siRNA in RH7777-Luc-GPC3 cells was detected using fluorophore-labeled siScramble. As shown in **Figure 12d**, fluorescence signal from NP-siRNA (red) could be observed throughout the cytoplasm, supporting the calcein endosomal integrity assay results that NP-siRNA was able to escape from endosomes and readily access the cytoplasm of cells. Once NP-siRNA was internalized into the cells through endocytosis, the PEI on NP copolymer coating can trigger endosomal escape through the proton sponge effect, where the influx of protons and counter-ions promotes the swelling and rupture of endosomes and the release of NP-siRNA complex into the cytoplasm [168].

We also measured NP-siRNA-associated toxicity using the Alamar blue (AB) assay. Compared to the untreated control, approximately 80% cell viability was observed at 48 hr after transfection (**Figure 12e**) indicating the biocompatibility of the NP. These results demonstrate that NP-siRNA can efficiently suppress a target gene with limited cellular toxicity in cultured HCC cells.

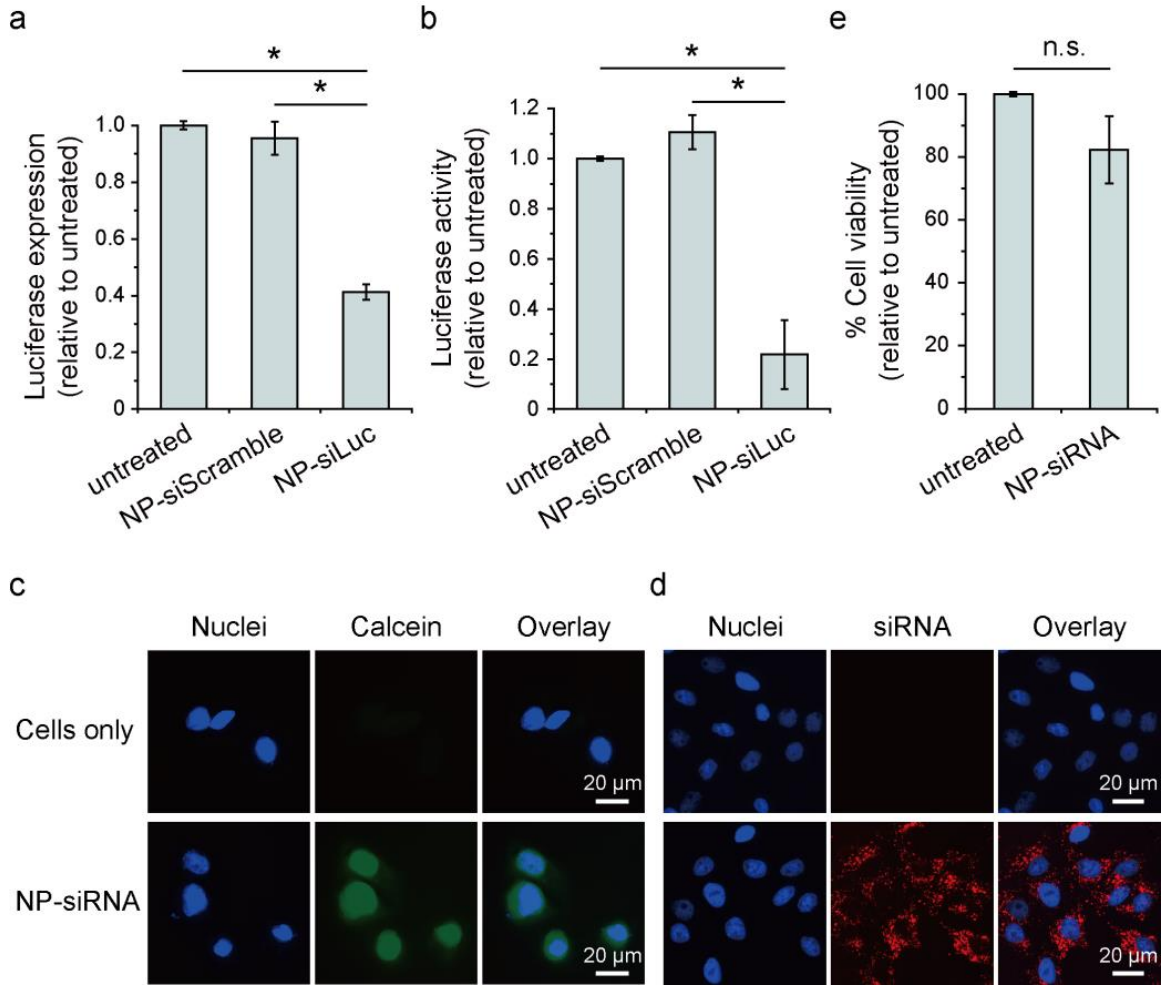

Figure 12. Effective suppression of Luc in RH7777-Luc-GPC3 cells by NP-siLuc transfection *in vitro*. (a) Knockdown of Luc mRNA in RH7777-Luc-GPC3 cells quantified by qRT-PCR. (b) Suppression of Luc protein in RH7777 cells as a result of NP-siLuc treatment. (c) Fluorescence images of RH7777-Luc-GPC3 cells treated with calcein (top row) and cells treated with NP-siRNA-GPC3 Ab and calcein mixture (bottom row). Scale bars correspond to 20 μm. (d) Fluorescence images of RH7777-Luc-GPC3 cells transfected with fluorophore-labeled NP-siRNA. Scale bars represent 20 μm. (e) RH7777-Luc-GPC3 cell viability after NP-siLuc treatment; * indicates statistical significance ($P < 0.05$) and n.s. indicates no statistical significance as determined by Student's *t*-test.

4.3.3 Establishment and Characterization of Orthotopic RH7777-Luc-GPC3 Xenograft

Having demonstrated that *in vitro* delivery of siLuc using our NP could produce effective gene silencing, we evaluated the efficacy of NP-siLuc mediated Luc suppression *in vivo*. We developed RH7777-Luc-GPC3 orthotopic xenografts as illustrated in **Figure 13a**. Successful hepatic grafting with a 5 mm tumor nodule with well-defined margins was observed during surgery. The histological characteristics of tumor tissues were analyzed by H&E staining. As shown in **Figure 13b,** a moderately well-defined tumor that is separated from normal liver is observed in the enlarged image. The marked nuclear crowding and typical trabecular growth pattern are representative histopathologic features of HCC [169]. This demonstrates the successful grafting of RH7777-Luc-GPC3 orthotopic xenograft tumors.

To verify GPC3 expression in the tumors, we isolated tumor cells and analyzed their surface GPC3 expressing using flow cytometry. As shown in **Figure 13c**, RH7777 cells with or without anti-GPC3 Ab staining show similar fluorescence intensity, suggesting the absence of GPC3 antigen expression. As a comparison, a distinct population of GPC3-positive cells was observed in isolated RH7777-Luc-GPC3 tumor cells, demonstrating that the RH7777-Luc-GPC3 xenograft tumors retained surface GPC3 antigen expression *in vivo*, and confirming that this model can be used for the study of GPC3 Ab-guided siRNA delivery *in vivo*.

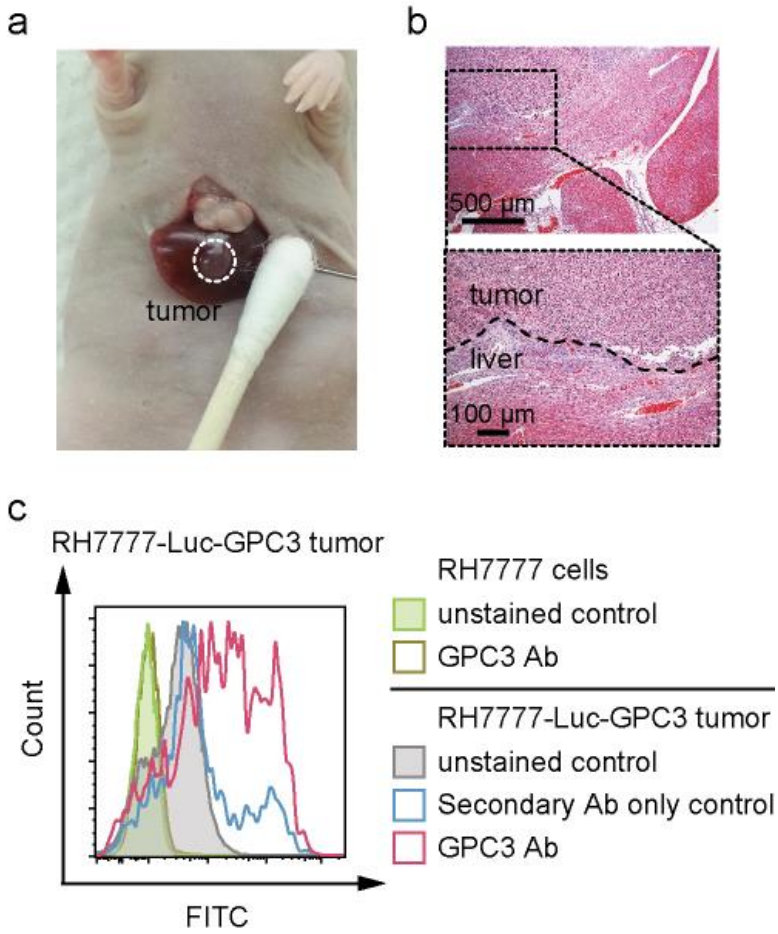

Figure 13. Characterization of orthotopic RH7777-Luc-GPC3 xenografts. (a) Photograph of RH7777 tumor implantation. The xenograft is recognized as a solitary nodule protruding from the liver surface. (b) Histological characteristics of the RH7777 tumor sections evaluated by H&E staining. (c) Representative flow cytometry analysis of GPC3 antigen displayed on the cell surface. Filled peaks represent unstained control of RH7777 cells and RH7777-Luc-GPC3 tumor. Histograms for secondary Ab control are also shown.

4.3.4 In Vivo Tumor Targeted Delivery of siRNA

Administration of siRNA specifically into tumor site and the correct intracellular location is essential for gene silencing activity. NP-mediated DNA/siRNA delivery can be enhanced specifically in the tumor through attachment of targeting ligands on the surface of the NP [6, 70]. To enable tumor targeted delivery of siRNA *in vivo*, we incorporated GPC3 Ab into NP-siRNA

(hereafter NP-siRNA-GPC3 Ab). The localization of NP-siRNA-GPC3 Ab to the orthotopic HCC was evaluated using Dy677-labeled siScramble complexed into NP. Mice were administered with NP-siRNA-GPC3 Ab via tail vein injection and imaged using a Xenogen IVIS Imaging system at 4, 24, 48, 72, and 120 hr post-injection with untreated mice as control (**Figure 14a**). Bioluminescent imaging revealed the tumor location while fluorescence imaging showed the distribution of Dy677-labeled siRNA.

As shown in **Figure 14a**, Dy677 fluorescence (red) from Dy677-labeled siRNA loaded NP was detectable in liver at 4 hr after injection. The overlap of the fluorescence and luminescence (blue) from tumors indicates accumulation of NP in the xenograft tumors. A decay of fluorescence signal as a function of time was also observed, most likely a reflection of the elimination of NP through clearance organs. NP-siRNA-GPC3 Ab remained detectable at 120 hr after injection, indicating the prolonged retention of NP-siRNA-GPC3 Ab in tumors. To further confirm the presence of NP-siRNA-GPC3 Ab within the tumors, the tumors were harvested and tumor sections were imaged by confocal fluorescent microscopy. There was no Dy677 fluorescence observed in untreated control animals whereas NP-siRNA-GPC3 Ab produced appreciable fluorescence in tumor regions (**Figure 14b**). In addition, Dy677 fluorescence was seen near the nucleus suggesting NP-siRNA-GPC3 Ab was able to deliver siRNA to the perinuclear region site of action. No accumulation of NP-siRNA-GPC3 Ab was detected in non-neoplastic tissue, including liver, spleen, kidney, and lung 5 days after NP injection (**Figure 15**), which further confirms the targeting capability of NP-siRNA-GPC3 Ab to HCC. These findings demonstrate that our NP platform can achieve targeted siRNA delivery to tumor tissue through intravenous administration.

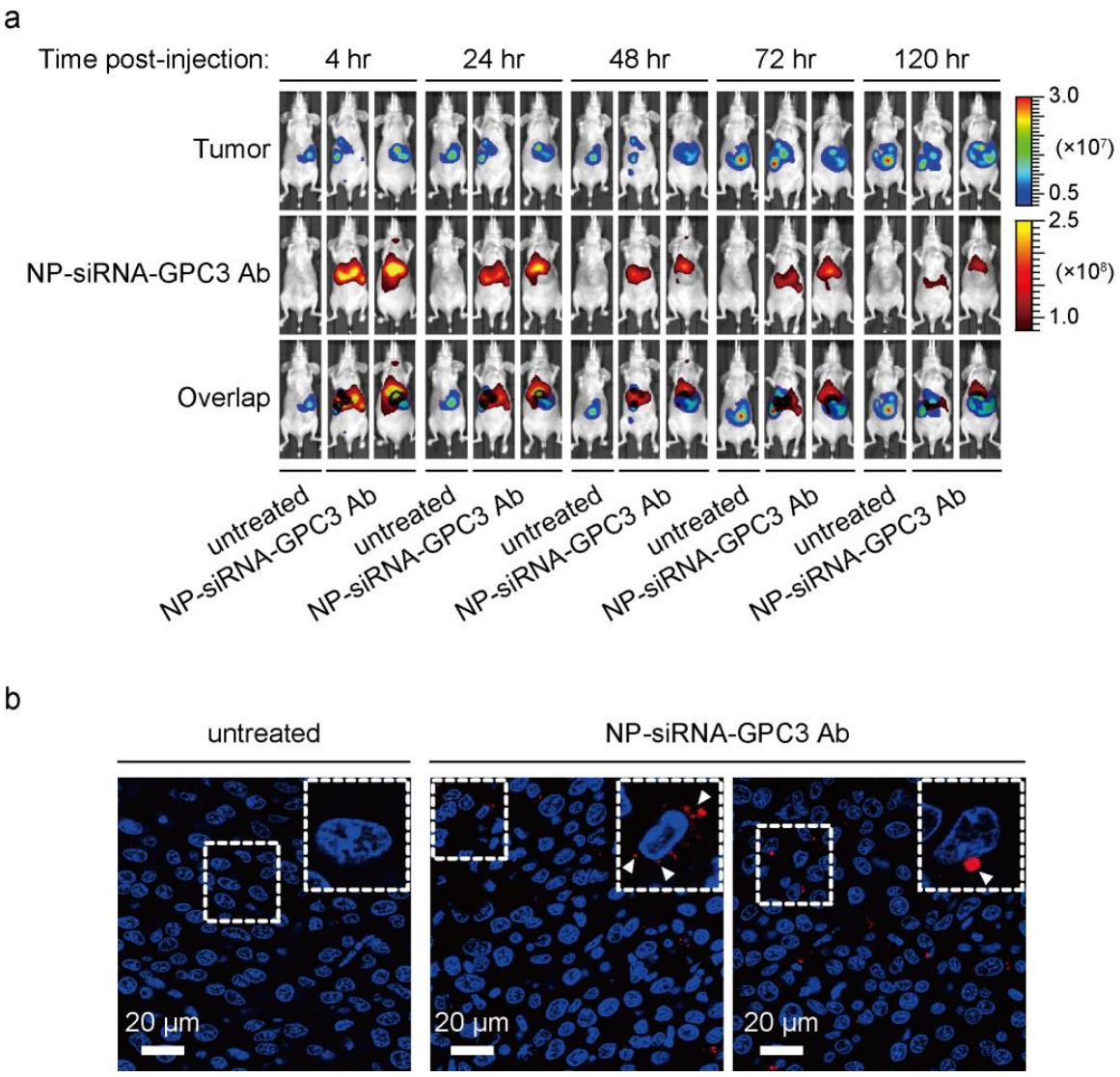

Figure 14. Evaluation of tumor uptake of NP-siRNA-GPC3 Ab *in vivo*. (a) Xenogen IVIS images showing co-localization of RH7777-Luc-GPC3 tumor and Dy677-labeled siRNA loaded NP at different time points post-injection from one untreated and two treated mice. (b) Confocal fluorescence microscopy images showing accumulation of NP-siRNA-GPC3 Ab in tumor sections at 120 hr after injection from the same animals presented in panel (a).

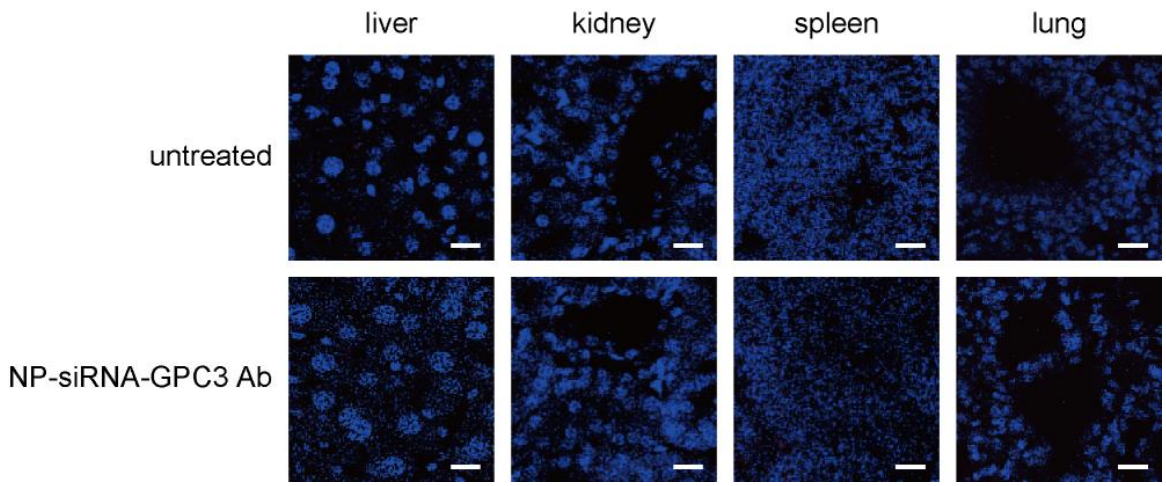

Figure 15. Fluorescence microscopy images showing biodistribution of NP-siRNA-GPC3 Ab in liver, kidney, spleen, and lung *in vivo* at 120 hr after injection. Scale bars represent 20 μm.

4.3.5 NP-Mediated Luc Silencing In Vivo

To determine whether the siRNA delivered to the tumor site was bioactive and could knock down gene expression, siLuc formulated in the nanovector was administered at 20 μg siRNA per animal intravenously daily for five days. Luc expression was assessed using a Xenogen IVIS Imaging system on 3, 6, 8, and 11 days after the first NP-siRNA-GPC3 Ab injection, as shown in the scheme in **Figure 16a**. A significantly decreased bioluminescence signal (from tumor cells) in NP-siLuc-GPC3 Ab treated mice was observed as compared to untreated mice and NP-siScramble-GPC3 Ab treated mice (**Figure 16b**). The normalization of the bioluminescent signal revealed that the untreated and control siRNA (siScramble) treated animals indicated a continuously elevated luminescence signal, representing the tumor cell proliferation. As a comparison, NP-siLuc-GPC3 Ab induced a dramatically retarded increase of luminescence signal, with approximately 4-times lower than untreated and control siRNA treated animals on day 11 (**Figure 16c**). In addition, both untreated and control siRNA treated animals showed similar tumor bioluminescence levels, indicating the effect was specific to siRNA delivery and not a non-specific reduction in tumor growth or Luc expression levels caused by the NP or GPC3 Ab themselves.

The tumor accumulation observed with fluorophore labeled NP-siRNA-GPC3 Ab may occur through both GPC3 Ab mediated targeting and passive tumor accumulation through the "enhanced permeability and retention" (EPR) effect [170, 171]. NP likely enter the tumor site though the EPR effect followed by active distribution throughout the tumor from the tumor targeting ligand [172, 173]. Without targeting ligand, positively charged NPs have strong affinity to both extracellular matrix (ECM) and target cells [174]. In contrast, accumulation of NP-siRNA-GPC3 Ab in tumor can be enhanced by GPC3 Ab. In the current study, the *in vivo* gene-silencing activity parallels tumor accumulation and intracellular uptake of NP complex. A sustainable reduction in Luc activity was induced by NP-siLuc treatment. This provides strong evidence that our nanovector is a suitable nanocarrier for siRNA delivery to HCC. The use of siRNA against therapeutic targets will be the next step in the development of these nanovectors for improved HCC therapy. We have found therapeutic targets that are effective alone [175] as well as those that can enhance the effects of conventional treatments [166]. Additionally, the targeting capacity of our nanovector may allow them to potentially reach any organ system with HCC involvement, which allows treatment of disseminated HCC [176, 177]. This could provide a more effective option for patients with untreatable HCC.

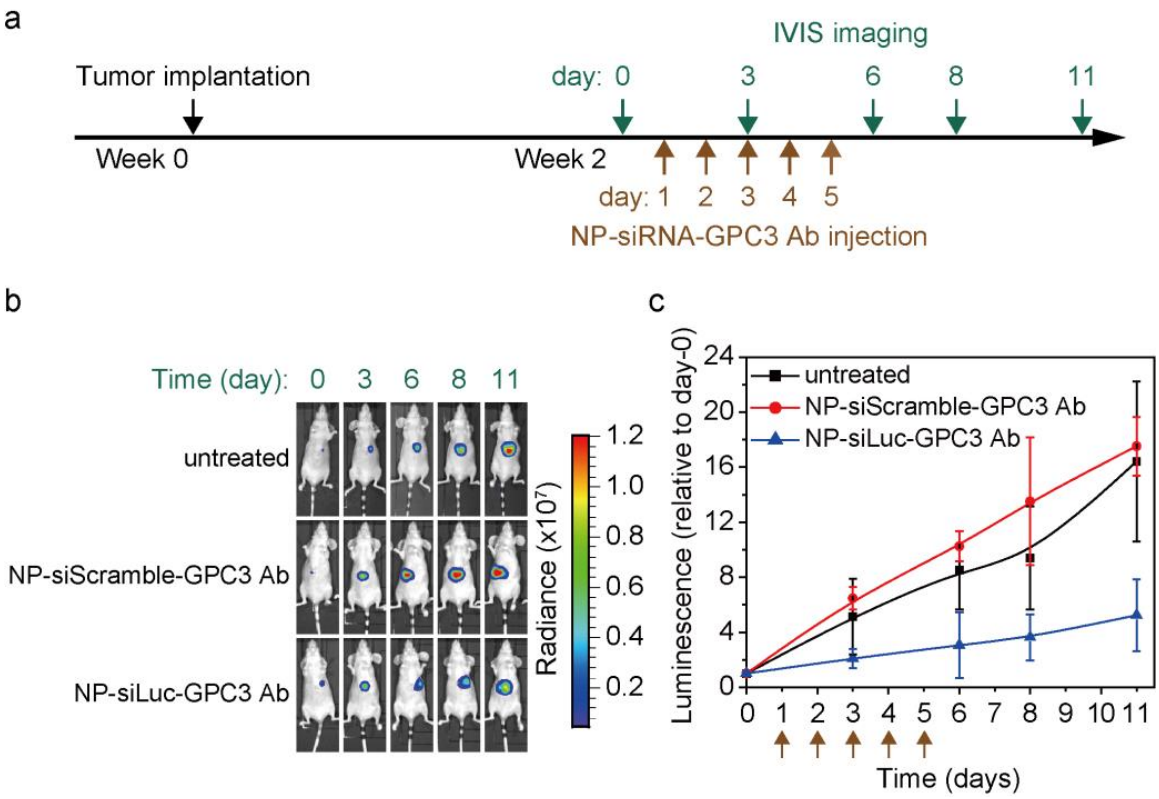

Figure 16. *In vivo* delivery of NP-siLuc-GPC3 Ab knocks down luminescence of RH7777-Luc-GPC3 tumors. (a) Scheme of tumor implantation and treatment. Two weeks after orthotopic injection with RH7777-Luc-GPC3 cells, xenograft-bearing mice received five daily intravenous injections of NP-siLuc-GPC3 Ab. IVIS imaging was initiated one day prior to the first NP-siLuc-GPC3 Ab injection. (b) Representative live IVIS images of mice bearing RH7777-Luc-GPC3 tumors with administration of NP-siLuc-GPC3 Ab. Untreated mice and mice treated with scramble siRNA served as the controls. (c) Quantitative luminescence of mice from untreated and treated groups (n = 4). Luminescence was normalized to day 0 and line graph was indicated as presented as mean ± SD. Arrows indicate NP-siRNA-GPC3 Ab injection.

4.4 CONCLUSIONS

We have reported the rational design and synthesis of an iron oxide-based nanoparticle coated with CP-PEI copolymer and conjugated with an anti-GPC3 Ab tumor targeting ligand for specific and effective siRNA delivery to HCC. The nanovector exhibited appropriate

physiochemical properties required for systemic siRNA delivery to tumor. We showed that the nanovector loaded with siRNA could successfully lower expression levels of target genes (Luc reporter) *in vitro* without evident associated toxicity. We further demonstrated that the intravenous administration of HCC targeted NP-siRNA-GPC3 Ab resulted in nanovector accumulation in RH7777-Luc-GPC3 orthotopic HCC and induced significantly decreased Luc activity. Overall, our results demonstrated the ability of this NP platform to overcome intra- and extra- cellular barriers and its promise in delivering siRNA for HCC treatment.

5. DEVELOPMENT OF SIRNA-BASED GENE THERAPEUTICS FOR CANCER

After demonstrating the efficacy of targeted delivery of small interfering RNA (siRNA) using our nanoparticles, we evaluated the therapeutic effect of siRNA-mediated suppression of biochemical pathways associated with malignancy and of another with drug resistance in glioblastoma (GBM) cells *in vitro*.

EGFR and β-catenin are two key mediators of cell signal transduction overexpressed in GBM and both play significant roles in GBM carcinogenesis. However, down-regulating EGFR individually only provide limited therapeutic efficacy. In this study, we demonstrated that simultaneous inhibition of EGFR and β-catenin potently decreased cell proliferation and delayed the progression of cell cycle in U-87 MG cells, although no significant increase in apoptosis was evidenced. The migratory ability of GBM cells was also inhibited. These findings suggest that combinatorial inhibition of EGFR and β-catenin expression could represent an effective therapy for human GBM, and warrants further study *in vivo*.

In addition to the combinatory siRNA treatment, we also evaluated the sensitization of GBM cells to temozolomide (TMZ), the mainstay chemotherapy for GBM, through RNA interference (RNAi). We demonstrated that siRNA against O6-methylguanine-DNA methyltransferase (MGMT), that repairs DNA adducts at the O6 position of guanine, significantly enhanced the chemosensitivity of human SF763 GBM cells to TMZ. These findings demonstrate that siRNA-mediated inhibition of MGMT can potentially serve as effective therapies for human GBM.

5.1 INTRODUCTION

Considerable research interest have been devoted to the development of novel treatments for GBM, among which gene therapy holds unique promise of specific gene targeting with applications to overcome drug resistance [23, 178]. Cellular signaling pathways implicated in the development and progression of GBM, the functions of several disregulated genes and their

potential use as targets for therapy are being extensively studied by several groups [179]. RNA interference (RNAi) is an effective approach that can potently inhibit these critical signaling pathways with relatively low toxicity and a high degree of specificity, far superior to that can be achieved by most anticancer agents [21, 69]. However, ablation of a single gene in a given pathway has not shown to provide maximal therapeutic efficacy [180]. Hence, targeting a range of different signaling pathways in GBM simultaneously has become urgently needed to produce a more robust and sustainable therapeutic effect.

The epidermal growth factor receptor (EGFR) has been implicated as a primary contributor to GBM pathogenesis, initiating the early stages of tumor development, sustaining tumor growth, promoting infiltration, and mediating resistance to therapy [181]. Aberrant expression of EGFR and its downstream effectors has been frequently observed in GBM [182, 183]. Several studies have also identified EGFR as a negative prognostic indicator of survival [184, 185]. However, clinical trials have demonstrated that gene-silencing of EGFR alone has been insufficient for GBM treatment, and when EGFR knockdown is combined with other therapeutics, the outcome has been far from uniform [186-190]. Wnt signaling is associated with tumorigenesis in various human cancers [191, 192] and there is increasing evidence to suggest that aberrancies within this pathway are responsible for the initiation and progression of malignant GBM [193, 194]. β-catenin is a key mediator of Wnt signaling and has been found to be over-expressed in GBM together with several other genes involved in the Wnt pathway [195, 196]. Although the mechanisms underlying the effects of β-catenin on GBM propagation are poorly understood, it has been postulated that accumulation of β-catenin is essential for more efficient GBM growth and progression [197]. Gene silencing of β-catenin has been demonstrated to successfully suppress malignant GBM cell growth [196]. In addition to being a therapeutic target in GBM treatment, β-catenin may also be used as a potential biomarker for pathological diagnosis of GBM as its expression level is associated with GBM grade [195].

In addition to playing a significant role in GBM individually, these two pathways have been reported to closely inter-twined in GBM tumorigenesis. Activation of EGFR could induce the up-regulation of β-catenin possibly through receptor tyrosine kinase pathway, while transactivation of β-catenin was demonstrated to facilitate EGFR-promoted GBM development [198, 199]. Previous studies have also confirmed that down-regulation of β-catenin could result in the reduced expression of components in EGFR pathway in GBM cells [197, 200].

Given the importance of the interaction between of EGFR and β-catenin in GBM carcinogenesis combined with the limitations of current therapies for GBM, we hypothesized that simultaneous inhibition of both genes may be an effective therapeutic approach for GBM overcoming the insufficient therapeutics when suppressing EGFR only. In the present study, we firstly confirmed the effect of siRNA treatment on down-regulating gene expression. Subsequently, cell survival, cell cycle progression, apoptosis and migration capability of GBM cells transfected with siRNA targeting EGFR and β-catenin were examined.

Although targeting cell signaling pathways associated with GBM tumorigenesis has attracted much research interests, chemotherapy still serves as the standard treatment for GBM. Temozolomide (TMZ) is the most commonly used alkylating agent chemotherapy of GBM regarding its ease of administration and capability of crossing blood brain barrier (BBB) [32]. However, its efficacy is often unsatisfactory due to inherent or acquired resistance of GBM to TMZ. Many studies have revealed that such resistance is closely associated with a high level of O6-methylguanine-DNA methyltransferase (MGMT) in tumor tissue. This protein can directly and specifically eliminate the cytotoxic alkyl adducts formed at the O6 position of guanine caused by TMZ [33, 34]. In this regard, much effort has been devoted to enhance the chemosensitivity of GBM to TMZ by ablating MGMT activity [35-37]. O6-benzylguanine (O6BG) is a potent MGMT inactivating agent that has been studied in combination with alkylating agents in restoring TMZ sensitivity in patients with recurrence malignant GBM [38]. However, it failed clinical trials because the continuous delivery of O6BG required to maintain a low level of MGMT caused severe bone marrow toxicity when combined with a therapeutic level of TMZ [36, 39-41]. Alternative TMZ dosing schedules have also been used to deplete MGMT activity, but the results are far from uniform [42]. Therefore, new strategies that provide safe inhibition of MGMT activity are expected to have a direct impact on GBM therapy. In this study, we inhibited MGMT expression in human SF763 GBM cells by delivering siRNA against MGMT, and evaluated the cellular response to TMZ using the clonogenic survival assay.

5.2 EXPERIMENTAL

5.2.1 Cell Culture and Transfection

Human malignant GBM cell line (U-87 MG), purchased from American Type Culture Collection (ATCC) was propagated in 75 cm^2 flasks at 37 ℃ in a humidified atmosphere with 5% CO_2 using the MEM cell culture medium supplemented with 10% FBS and 1% antibiotic-antimycotic (Life Technologies). Human SF763 GBM cells were cultured at 37 ℃ in a humidified atmosphere with 5% CO_2 using DMEM supplemented with 10% FBS (Atlanta Biologicals) and 1% antibiotic-antimycotic (Life Technologies).

Twenty-four hours after plating the U-87 MG cells in antibiotic-free complete MEM medium, the cells were transfected with 25 nM siRNA using DharmFECT4 reagent according to the manufacture's instructions (Dharmacon). The non-targeting siRNA was purchased from Ambion and the ON-TARGET plus siRNA against EGFR and β-catenin were purchased from Dharmacon Research Inc.

5.2.2 Quantitative RT-PCR (qRT-PCR)

RNA was extracted from cells 48 hr after siRNA transfection using the Qiagen RNeasy kit. cDNA was prepared using the Qiagen RNeasy kit following the manufacturer's protocol, which was then used as a template for PCR. qRT-PCR was used to evaluate the relative expression levels of EGFR and β-catenin utilizing glyceraldehyde 3-phosphate dehydrogenase (GAPDH) as a control. SYBR Green PCR Master mix (Bio-Rad) was used for template amplification with a primer for each of the transcripts in a Bio-Rad CFX96 real-time PCR detection system. Quantitative amplification was monitored by the level of fluorescence reflecting the cycle number at the detection threshold (crossing point) using a standard curve. Thermocycling for all targets was carried out in a solution of 25 µl containing 0.2 µM primers (Integrated DNA Technologies) and 4 pg of cDNA from the reverse transcription reaction under following conditions: 95 ℃ for 15 min, 45 cycles of denaturation (15 sec, 94 ℃), annealing (30 sec, 55 ℃), and extension (30 sec, 72 ℃). The primers used for EGFR and β-catenin amplification were: 5'-TGACTCCGTCCAGTATTGATC-3'/5'-ATTCCGTTACACACTTTGGGG-3' and 5'-

CCTCTGATAAAGGCTACTGTT-3’/5’-CTGATGTGCACGAACAAGCA-3’, respectively. The pre-evaluated primers used for MGMT amplification was purchased from Bio-Rad.

5.2.3 Cell Viability Assay

The effect of targeted or control siRNA on U-87 MG cell proliferation was determined using the Alamar blue (AB) cell viability assay following the manufacture’s protocol (Life Technologies). Briefly, cells were plated and transfected as described. After treatment, cells were washed with PBS three times before adding 10% AB in MEM medium to the wells. Cells were incubated for 1 hr, then the AB solution was transferred to a 96-well plate, and the fluorescent emissions at an excitation wavelength of 550 nm and an emission wavelength of 590 nm were read on a SpectraMax M5 microplate reader (Molecular Devices).

5.2.4 Clonogenic Assay

U-87 MG and SF763 cells were treated with control or targeted siRNA for 48 hr as described above. The cells were then trypsinized, and 300 cells were plated per well in six-well plates in normal, 10% FBS-containing medium in triplicate. For SF763 cells, TMZ (TCI AMERICA) was treated at 24 hr after plating. Cells were cultured for 2 weeks before fixation and staining with Methylene Blue. Colonies consisting of 50 or more cells were counted.

5.2.5 Cell Cycle Distribution Analysis

Seventy-two hours following siRNA treatment, cells were harvested, washed and fixed with 70% ethanol at 4℃ overnight, followed by treatment of 0.5 μg/ml RNase and 50 μg/ml propidium iodide (PI) at 4℃ for 3 hr. The cells (1×10^5) were then analyzed for their DNA content using a BD FACS Canto flow cytometer (BD Biosciences). All data were analyzed with Flow Jo. Results are presented as percentages of cells in the various phases, G0/1, S, G2/M.

5.2.6 Assessment of Apoptosis by Annexin V Staining

The extent of apoptosis was determined by flow cytometry using the Apoptotic, Necrotic & Healthy Cells Quantification Kit (Biotium). Forty-eight hours following siRNA transfection, staining of U-87 MG cells was carried out following the manufacturer's protocol. Fluorescence-activated cell sorter analysis was performed with a BD LSR II Flow Cytometer (BD Biosciences). Data were analyzed with FlowJo software. Annexin V-FITC and Ethidium Homodimer III (EtD-III) double stain was used to evaluate the proportion of cells undergoing apoptosis. We defined Annexin V-FITC positive cells as apoptotic [201, 202]. The percentage of specific apoptosis was calculated by subtracting the percentage of spontaneous apoptosis of the relevant controls from the total percentage of apoptosis.

5.2.7 Scratch Migration Assay

U-87 MG cells were transfected with scrambled control or targeted siRNA, plated, and allowed to form a monolayer for 48 hr after treatment. A linear scratch wound was created on the monolayer using a 200 µl pipette tip, and the non-adherent cells were washed off with PBS. Cells were then incubated at 37℃ in 5% CO_2. To minimize the contributions of cell proliferation, MEM medium containing 2% FBS was used following the wash. Each scratch was randomly photographed at three separate sites along the length of the scratch, starting proximally and ending distally at 12 hr after the scratch injury, when cell migration was apparent but effects of cell proliferation were negligible. Bright-field images were captured at 4-times magnification (Nikon ECLIPSE TE2000-S microscope) and analyzed using Tscratch [203]. Data are represented as the percentage of the closure area of cells migrating into the scratch area.

5.2.8 Statistical Analysis

For statistical analysis, acquired data are expressed as mean ± SD. Statistical significance was determined using the Student's *t*-test. Significant values were designated as follows: $*P < 0.05$, $**P < 0.01$.

5.3 RESULTS AND DISCUSSION

5.3.1 Reduction of EGFR and β-catenin mRNA Expression by siRNA

The ability of siRNA against EGFR and β-catenin to induce a substantial decrease in expression of these genes in U-87 MG cells was confirmed by quantifying the mRNA level using qRT-PCR. The scramble siRNA did not affect either of the two targets, as the expression level was comparable to that in non-treated cells, whereas siRNA targeting EGFR or β-catenin resulted in 89% and 80% reduction in the respective mRNA transcripts (**Figure 17**). It was apparent that while siRNA targeted against β-catenin did not significantly affect the expression of EGFR, siRNA targeting EGFR inhibited the expression of β-catenin by 36%. Moreover, the combinatorial inhibition of both targets resulted in similar levels of down-regulation compared to the individual siRNA-treated cells, confirming successful down-regulation of EGFR and β-catenin by the siRNA in combination.

An interesting finding was that the inhibition of EGFR also suppressed the mRNA expression of β-catenin, suggesting that crosstalk between these two pathways which has been described in many other types of cancers [199, 204, 205] may also be present in GBM. Conversely, it has also been reported that β-catenin can affect EGFR signaling by down-regulating certain components of the EGFR pathway in GBM, such as STAT3 and MYC [200]. However, this was not observed in our study; with no significant effect on STAT3 expression at the mRNA level (data not shown). The disregulation of STAT3 or MYC may be more apparent on the protein expression level. Another potential reason for this may be the unique gene expression level in the EGFR pathway of U-87 MG cells, as the majority of Wnt target genes was found to be cell-type specific [206, 207].

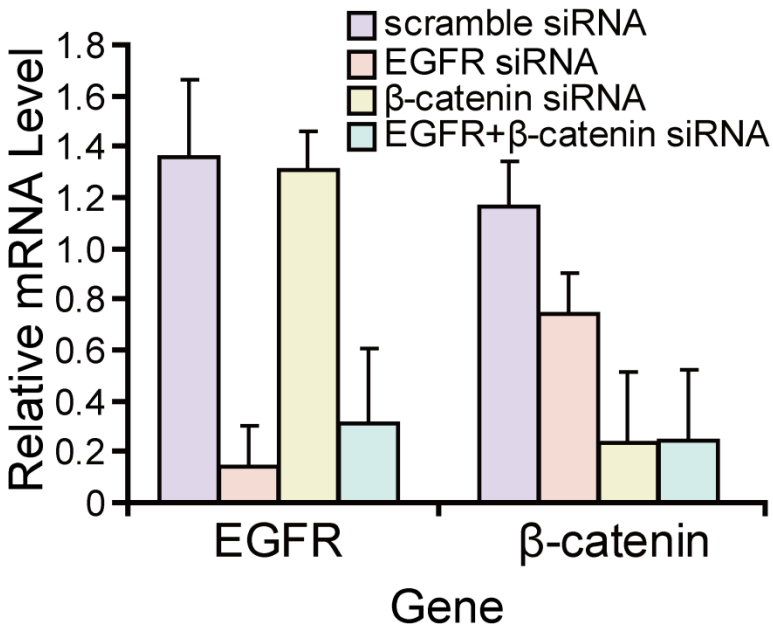

Figure 17. The mRNA expression of EGFR and β-catenin in U-87 MG after siRNA transfection**.** The mRNA expression of EGFR and β-catenin in U-87 MG cells at 48 hr after transfection of control and targeted siRNA. GAPDH served as internal control. Expression of EGFR and β-catenin was normalized to untreated controls.

5.3.2 Knockdown of EGFR and β-catenin Suppresses Human GBM Cell Proliferation and Colony Formation

Given the implications of EGFR and β-catenin on GBM pathogenesis and propagation, the effect of RNAi against these genes on cell growth and proliferation was evaluated. Scramble siRNA-treated GBM cells remained at a similar growth rate with non-treated cells throughout the entire experimental period, while knockdown of β-catenin alone or simultaneously with EGFR both led to reduction of U-87 MG cell proliferation as shown in **Figure 18a**. Reduction in EGFR expression had a limited effect in impairing cell proliferation, as EGFR siRNA-treated cells appeared to maintain their proliferative capacity throughout the entire period of the experiment. Transfection of siRNA against β-catenin induced reduction of proliferation to about 70% ± 4.5% by 96 hr after transfection and it remained decrease in the following days, reaching 48% ± 1.0% on day 6 (**Figure 18b**). The combinatorial treatment with the two siRNA had a similar anti-proliferative effect, with the cell viability reduced by 46% on day 7 after transfection.

In agreement with several previous reports [195, 208], our results also revealed that down-regulation of EGFR did not reduce cell proliferation as significantly as with β-catenin inhibition from both the cell viability and clonogenic assays, which thereby resulted in comparable inhibitory effect of targeting β-catenin alone versus the combinatorial treatment. There have been conflicting reports in the literature regarding the therapeutic effect of targeting EGFR against GBM. Certain studies have demonstrated that inhibition of EGFR alone was unsatisfactory for GBM tumor suppression [190, 208]. Along with our findings, these results suggest the necessity of combined RNAi treatment, as the inhibition of β-catenin could effectively serve as a compensatory silencing mechanism to the insufficient targeting of EGFR alone.

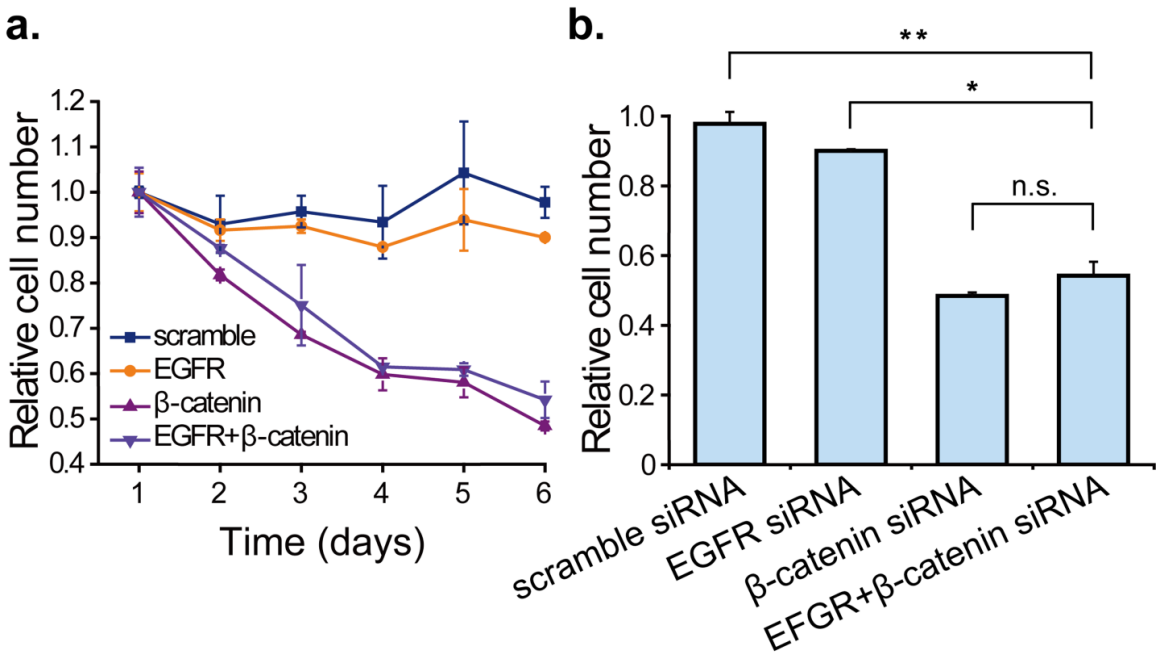

Figure 18. Cellular proliferation of U-87 MG transfected with scramble, EGFR and β-catenin siRNA. (a) The proliferation of U-87 MG treated with control siRNA and siRNA targeting β-catenin alone or EGFR and β-catenin simultaneously during the 6-day observation period starting from the second day after transfection. (b) Bar graphs indicating cell viability using siRNA either individually or in combination compared with scramble siRNA on day 6. Data are expressed as percentage of viable cells relative to untreated control cultures. Asterisk indicates significant level in Student's *t*-test: $*P < 0.05$, $**P < 0.01$, n.s.: non-significant.

To evaluate long-term efficacy of siRNA on cell survival, the clonogenic assay was then performed. The decrease in colony-forming ability resulting from knockdown of EGFR and β-catenin individually was evidenced, but the scramble siRNA did not affect the long-term survival of U-87 MG cells compared with the non-treated control (**Figure 19**). In particular, combinatorial siRNA significantly impaired long-term survival of U87-MG, as indicated by an approximate 6-fold fewer formed colonies in comparison to the scramble siRNA treated cells.

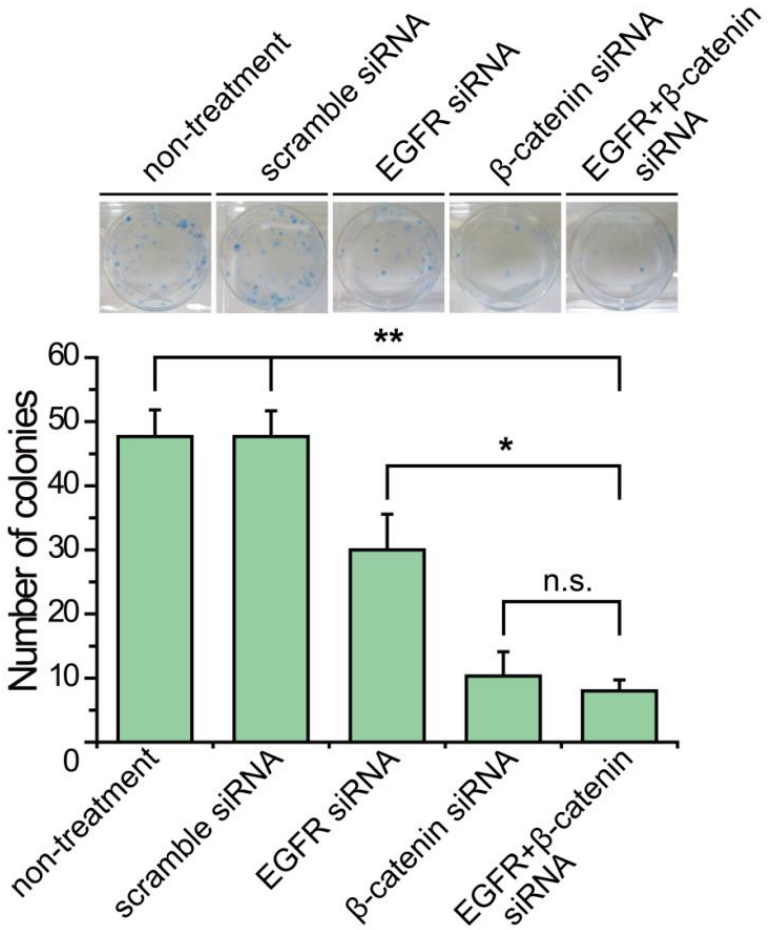

Figure 19. Colony formation capacities of U-87 MG with siRNA transfection. Colony formation of U-87 MG cells transfected with scramble, EGFR and β-catenin siRNA is represented as in the images. The mean ± SD number of colonies was quantified and presented in the bar graph.

Asterisk indicates significant level in Student's *t*-test: $*P < 0.05$, $**P < 0.01$, n.s.: non-significant.

5.3.3 Down-Regulation of EGFR and β-catenin by siRNA in Human GBM Cells Induces G0/1-Phase Arrest

We were interested in examining the effects of combinatorial siRNA on cell cycle progression in GBM. U-87 MG cells were transfected with siRNA against EGFR and β-catenin alone or in combination, at the same conditions used in the above-mentioned assays. At 72 hr after treatment, cells were labeled with PI and the DNA content was analyzed by flow cytometry. As shown in **Figure 20**, the siRNA targeting either EGFR or β-catenin caused an increase in the proportion of cells arrested in the G0/1 phase and a corresponding decrease in the proportion of cells in the S and G2/M phases, and this effect became more pronounced when EGFR and β-catenin were down-regulated simultaneously, with the G0/1 phase fraction increasing to 68.7% as compared to 55.8% in the scramble siRNA treated groups. These results revealed the delay in cell cycle progression in GBM cells transfected with the siRNA in combination, suggesting that the decreased cell viability may be a result of cell cycle arrest. In fact, G0/1 phase arrest has been previously observed in EGFR or β-catenin down-regulated GBM [195, 196, 209], although the accumulation of G0/1 phase arrested cells was less obvious in our studies. This may due to the difference in growth profiles or the timescale for the occurrence of cell cycle arrest among GBM cell lines.

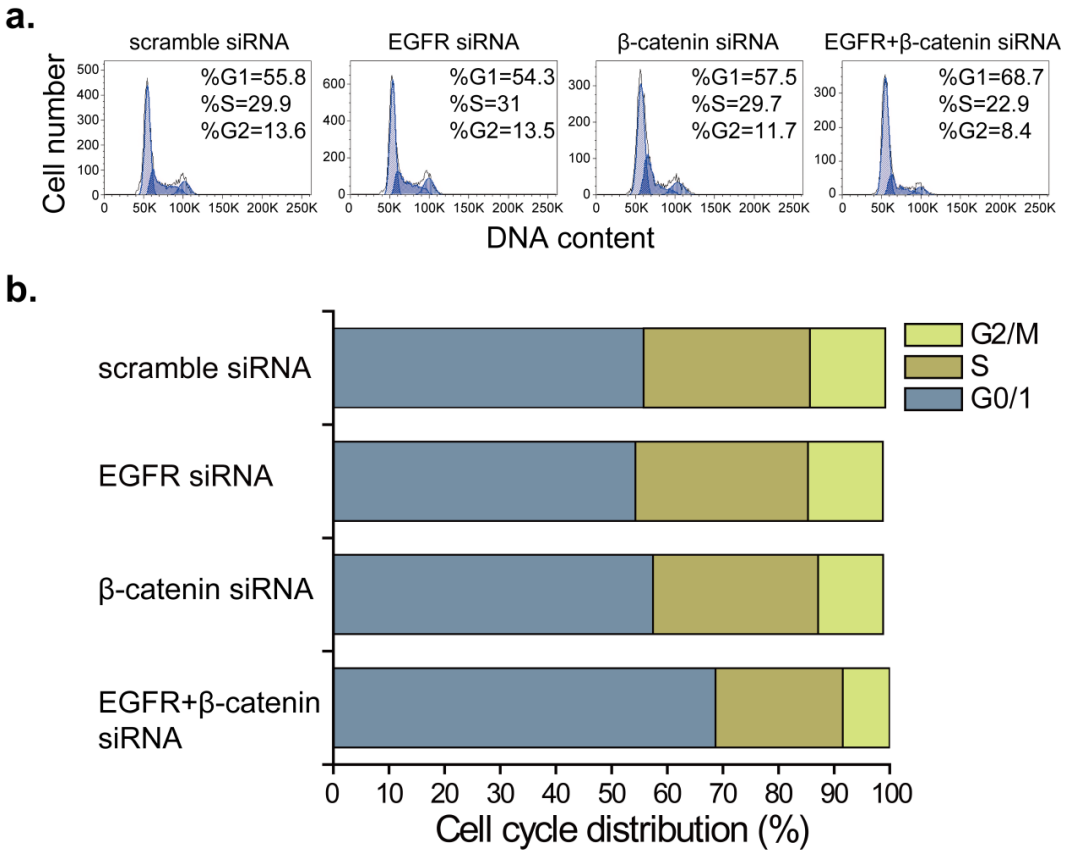

Figure 20. Representative cell cycle distributions in U-87 MG transfected with control siRNA and targeted siRNA individually and in combination. (a) Cell cycle phase distribution of U-87 MG cells after siRNA transfection for 72 hr. (b) Bar graph indicates the proportions of cells in G0/1, S and G2/M phases of the cell cycle. All experiments were performed in duplicate and gave similar results.

5.3.4 Induction of Apoptosis in GBM Cells by siRNA Targeting EGFR and β-catenin

To investigate the extent of apoptosis induced by EGFR and β-catenin gene-silencing, cells treated with siRNA were stained with Annexin V-FITC and EtD-III and then analyzed by flow cytometry at 48 hr following transfection. The two-dimensional flow cytometric profiles of U-87 MG cells are depicted in **Figure 21**. The percentage of apoptotic cells among β-catenin siRNA treated cells was similar to that of cells transfected with EGFR siRNA, with an apoptotic rate of

8.9% ± 4.2% and 8.9% ± 4.9%, respectively. The combinatorial down-regulation of EGFR and β-catenin induced 11.9% ± 3.9% apoptotic cells. This proportion was comparable to that induced by the individual siRNAs, but significantly increased ($p < 0.05$) compared with cells transfected with scramble siRNA, which had an apoptotic rate of 4.9% ± 1.7%.

Apoptosis was evidenced when knocking down EGFR and β-catenin both individually and in combination, but there was no statistic difference in apoptosis rate among the siRNA treated groups, suggesting that the two genes may play comparable roles in regards to inducing apoptosis and the combinatory treatment did not appear to possess a synergetic effect in GBM. We speculated that the majority of U-87 MG cells underwent autophagy instead of apoptosis in response to the combined siRNA treatment. GBM cells have been shown to be more resistant to apoptosis than to autophagy-related cell death [210, 211] and autophagy as a protective cellular response to EGFR down-regulation has been supported in previous studies [212-214]. Accordingly, such autophagy-related anti-apoptotic nature of GBM is capable in preventing apoptosis when both EGFR and β-catenin were down regulated.

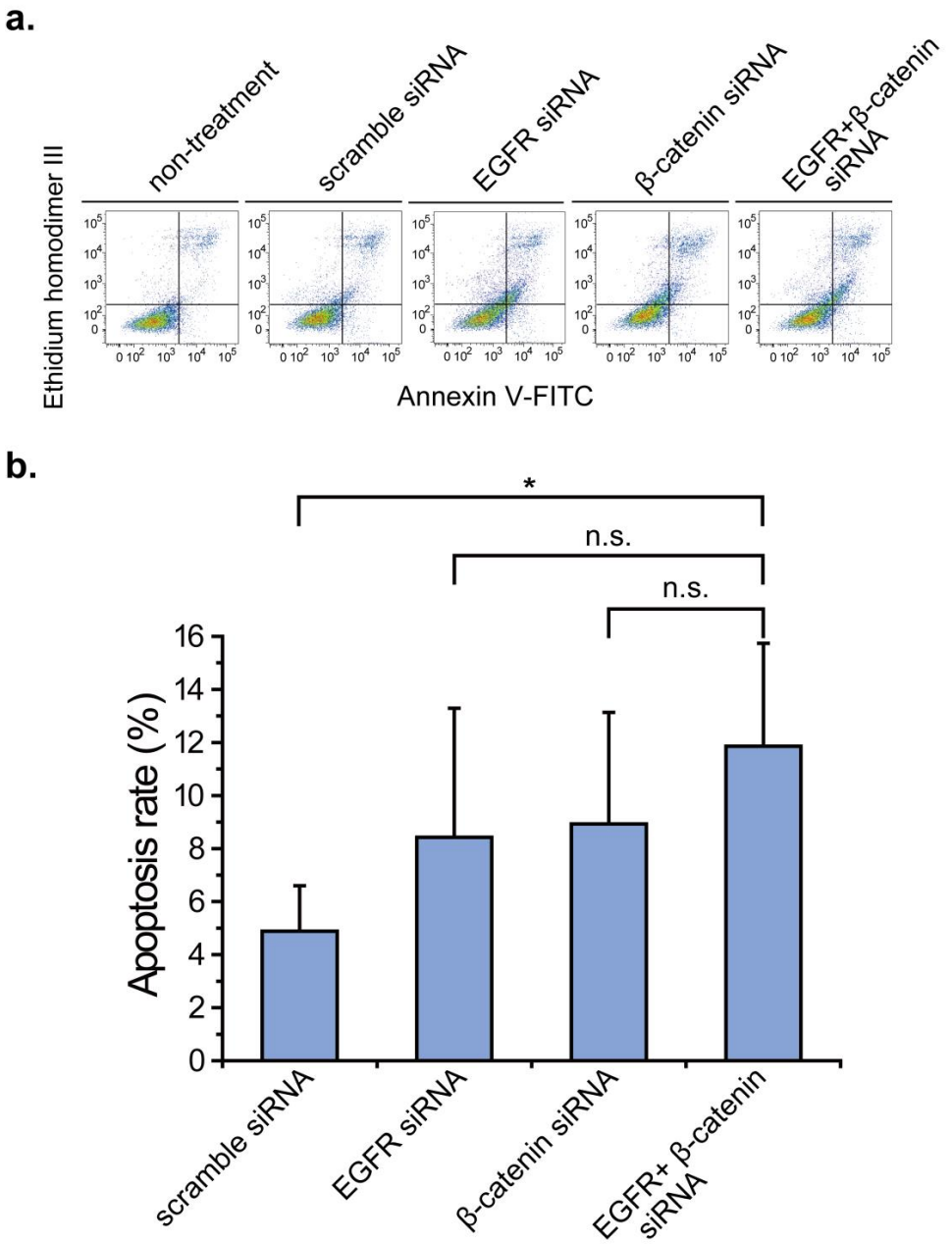

Figure 21. Apoptotic induced by siRNA transfection on U-87 MG cells. (a) Apoptotic index of U-87 MG cells transfected with control and targeted siRNA and stained by annexin V-FITC and EtD-III followed by flow cytometry analysis. (b) The apoptosis rate of U-87 MG cells treated with scramble and targeted siRNA is shown in the bar graph. Asterisk indicates significant level in Student's *t*-test: $^{**}P < 0.05$, n.s.: non-significant.

5.3.5 EGFR and β-catenin Affect the Migratory Capacity of GBM Cells

Scramble and targeted siRNA transfected U-87 MG cells were then used in a scratch wound assay to identify their effect on inhibiting GBM cell migration (**Figure 22a**). Both EGFR and β-catenin siRNA led to a decrease in the wound surface coverage by migrating U-87 MG cells at 12 hr following induction of the scratch wound, which were 22.4% ± 3.7% and 21.4% ± 4.2%, respectively (**Figure 22b**). Simultaneous knockdown of the two genes substantially inhibited migration of the cells, inducing a roughly 5-time less migration into the scratch area in comparison to the cells transfected with scramble siRNA and approximately 44% to 41% less migration compared to EGFR and β-catenin silenced cells. These results are corroborated by previous reports where EGFR was implicated as a regulator of GBM cell migration and motility [215, 216]. An invasion assay was then conducted using the Matrigel coated transwells. Knockdown of EGFR and β-catenin alone reduced the number of invasive U-87 MG cells relative to those transfected with scramble siRNA by 35% and 23%, respectively (**Figure 22c**). The combinatory siRNA treatment led to a decrease in GBM cell invasiveness by 57% relative to the cells treated with the scramble siRNA control. In addition, the number of invasive cells treated with combinatory siRNA group as compared to the EGFR and β-catenin was nearly 34% and 44%, respectively.

Down-regulation of MMP-2 protein levels was induced by knocking down of β-catenin, which suggests that the cellular migration may involve the phosphorylation of β-catenin [217]. Our studies provide more direct and promising evidence on the indispensible role that β-catenin plays in this cellular behavior of GBM, and more importantly, demonstrates that inhibition of EGFR and β-catenin simultaneously could provide an essential therapy for limiting tumor cell progression via migration.

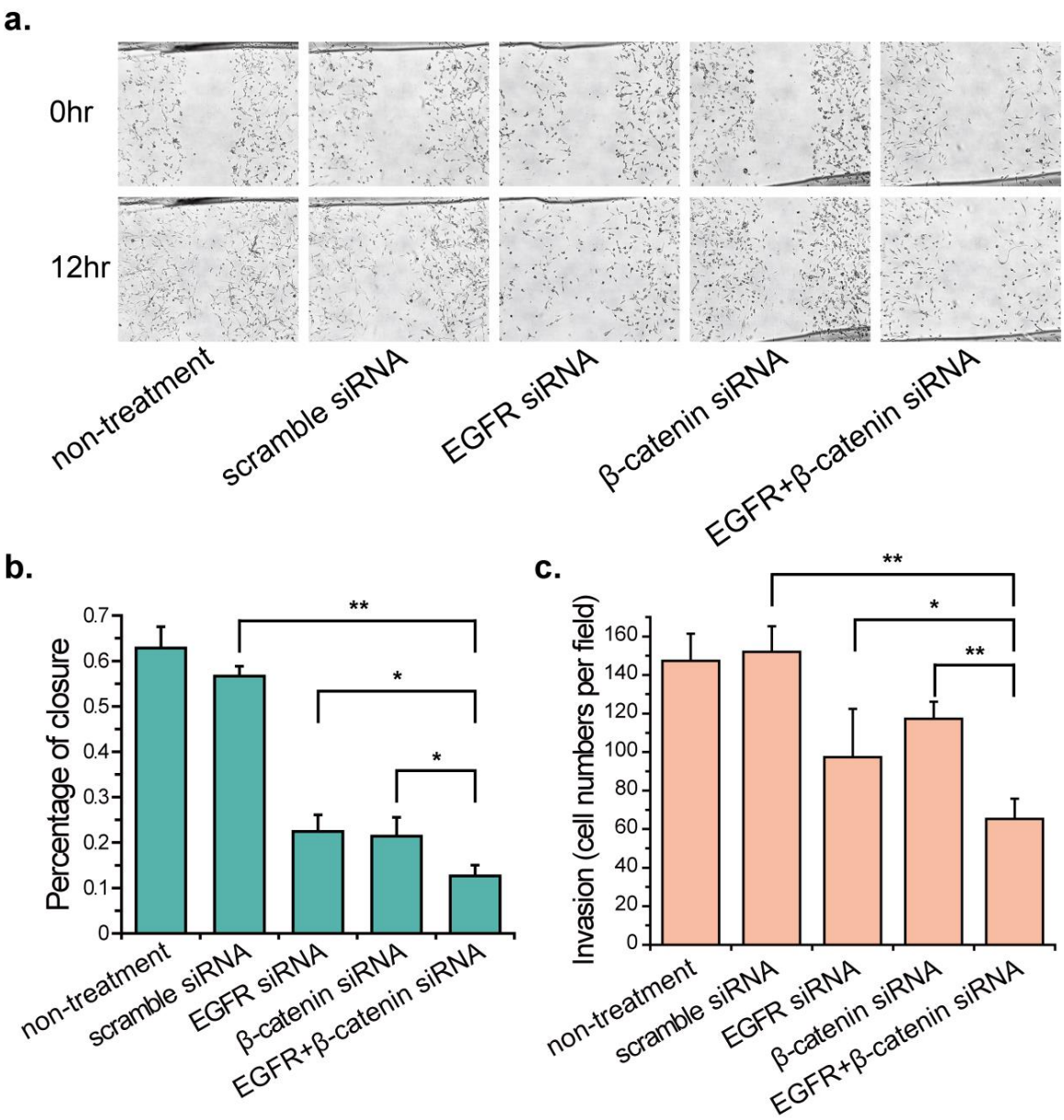

Figure 22. Effects of knockdown of EGFR and β-catenin on U-87 MG cell migration and invasion. (a) Representative bright-field images of U-87 MG cell migration across the wound edges at 0-24 hr after wounding in confluent U-87 MG transfected with scramble and targeted siRNA. (b) The bar graph represents the quantitative results for percent closure of cells migrating to the wound area. Analyses were performed at two randomly positions, and the error bars indicate the SD of the two independent analyses. (c) Decreased numbers of invading U-87 MG

cells were observed after siRNA transfection in transwell analysis. Asterisk indicates significant level in Student's *t*-test: $*P < 0.05$, $**P < 0.01$.

5.3.6 Down-Regulation of MGMT Sensitizes Human GBM Cells to TMZ

The effect of MGMT siRNA in sensitizing human GBM cells to TMZ was also evaluated in the short-term and long-term using AB and clonogenic assay, respectively. SF763 cells were used in this study because of their high MGMT activity [218]. As shown in the survival curves in **Figure 23**, much less TMZ was required to induce an obvious cytotoxicity in MGMT siRNA transfected SF763 cells, while the control GFP siRNA did not alter the resistance of SF763 to TMZ. The shift of the survival curve of MGMT siRNA treated cells was more significant from the clonogenic assay, suggesting that this assay is more sensitive than the AB assay. Results from both assays confirmed our speculation that suppression of MGMT is efficient in sensitizing GBM cells to TMZ.

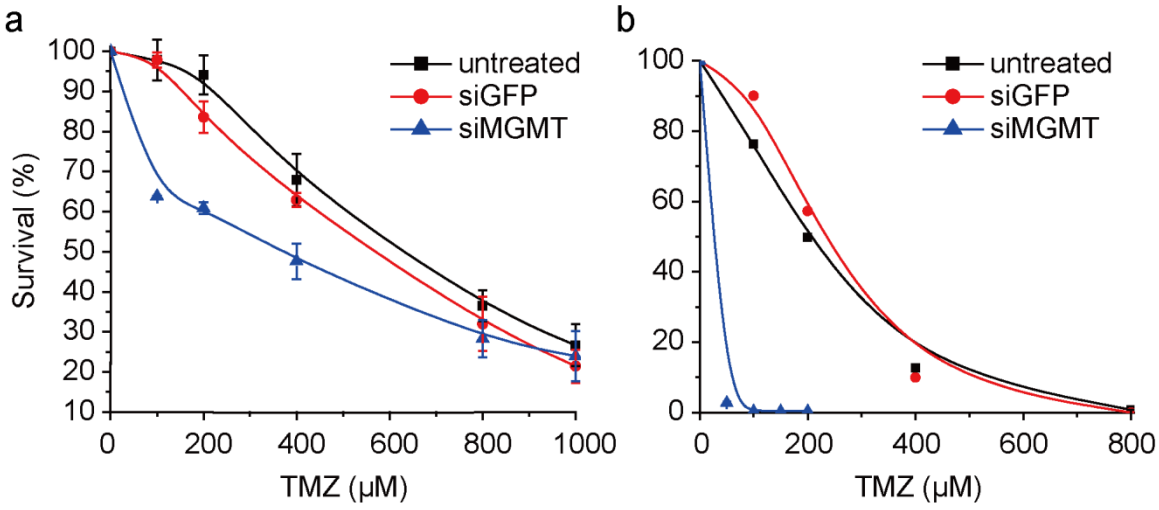

Figure 23. Cell survival of SF763 with siMGMT and TMZ treatment from AB (a) and clonogenic assay (b).

5.4 CONCLUSIONS

The results presented here demonstrate that a therapeutic effect on GBM can be achieved by targeting and silencing EGFR and β-catenin simultaneously. Also, the combinatorial treatment of siRNA against MGMT with TMZ can serve as a new effective therapy strategy against GBM, and warrants further study *in vivo*.

6. SENSITIZATION OF CANCER TO CHEMOTHERAPY BY IRON OXIDE NANOPARTICLE-MEDIATED SIRNA TREATMENT

Previous studies have demonstrated that RNA interference (RNAi) offers the potential for highly specific treatment for human glioblastoma (GBM) with minimal side effects. However, the lack of safe, tumor targeted delivery vehicles has hindered the translation of RNAi therapies into widespread clinical use. To this end, we have developed a tumor targeted, superparamagnetic iron oxide nanoparticle that shows high transfection efficiency and low toxicity *in vitro* and *in vivo*. We showed that this multifunctional nanoparticle was able to successfully deliver small interfering RNA (siRNA) against O6-methylguanine-DNA methyltransferase (MGMT) *in vitro* and *in vivo* to significantly enhance the chemosensitivity of human GBM cells to temozolomide (TMZ). Notably, *in vivo* administration of MGMT siRNA using nanoparticles was effective against GBM stem-like cells and effectively diminished tumor growth and extended survival of mice bearing human GBM6 tumors. Taken together, these findings demonstrate the potential clinical use of the nanoparticle-siRNA mediated treatment for human GBM.

6.1 INTRODUCTION

GBM is the most aggressive and deadly malignant primary brain tumor in humans, with approximately new diagnoses annually [77]. The greatest improvement in GBM survival over the past 30 years was achieved by including the methylating agent TMZ during radiotherapy, which significantly improved survival to 14 months [219]. Thus, TMZ is the most commonly used chemotherapy agent in GBM treatment as it is delivered orally, is well tolerated, and can cross the blood brain barrier (BBB) [220]. However, a large subset of patients do not respond to TMZ, which was found to be closely associated with a high level of MGMT, the only protein that provides cells the ability to remove O6-methylguanine from DNA [221-223]. Moreover, recent studies suggest that GBM stem-like cells (GSCs), a subpopulation of tumor cells, are also responsible for chemo-resistance partially due to their high MGMT expression [224-227]. GSC

killing remains a significant hurdle in GBM treatment and is thought to be responsible for the high rate of recurrence [228, 229].

In this regard, much effort has been devoted to enhancing the chemosensitivity of GBM to TMZ by ablating MGMT activity [230, 231]. O6-benzylguanine (O6BG), a chemical inhibitor of MGMT, has received significant attention, but failed clinical trials because the continuous delivery of O6BG required to maintain a low level of MGMT caused severe bone marrow toxicity when combined with a therapeutic level of TMZ [232-234]. Therefore, new strategies that provide safe inhibition of MGMT activity are expected to have a direct impact on GBM therapy.

Small interfering RNA (siRNA) based RNA interference (RNAi) holds unique promise of specific gene targeting with low systemic toxicity and immunogenicity that is far superior to conventional treatments [21, 23, 69]. The growing interest in RNAi has garnered a strong incentive to develop advanced materials for delivery of siRNA with high efficiency, stability, and minimal cytotoxicity [147, 235-237]. Among the various constructs studied [238], iron oxide nanoparticles have emerged as a highly desirable siRNA delivery platform owing to their ability to penetrate the BBB and efficiently deliver nucleic acids specifically into GBM cells [6, 8, 70, 102].

Here we report on a multifunctional iron oxide nanoparticle for siRNA-mediated suppression of MGMT. We demonstrate this nanoparticle can enhance the chemosensitivity of GBM cells and GSC tumors to TMZ, and extend survival of animals bearing human GBM tumors. This nanoparticle platform could lead improved standard-of-care treatment for GBM patients and be translated to widespread clinical use.

6.2 EXPERIMENTAL

6.2.1 CP-PEI Copolymer Synthesis

PEG was grafted to depolymerized chitosan using a method described previously [165]. Amine groups on 25,000 Da polyethylenimine (PEI, Sigma-Aldrich) were modified with 2-iminothiolane (Traut's reagent, Molecular Biosciences) for 1 hr in thiolation buffer. Concurrently, chitosan-grafted PEG (CP) was modified with N-succinimidyl iodoacetate (SIA,

Molecular Biosciences) at a 1:10 molar ratio in thiolation buffer (pH 8.0) through N-hydroxysuccinimide ester chemistry before removing unreacted SIA reagent using a Zeba spin column (Thermo Scientific) equilibrated with thiolation buffer (pH 8.0). The modified CP was then added to PEI-Traut's for attachment through the formation a thiol-ether bond. After reaction at room temperature for 4 hr, the resultant mixture was dialyzed with a dialysis membrane (MW 50,000 cut, Spectrum Labs) against distilled water, and the solution was subsequently freeze-dried.

6.2.2 CP-PEI Copolymer Characterization

The presence of the constituent polymers on the lyophilized CP-PEI was verified by proton NMR (^{1}H-NMR) in D_2O. Trimethylsilyl propionate was used as the internal standard. NMR spectra of polymer coatings were obtained using a Bruker Avance 301 spectrometer operating at 300 MHz and 298 K.

6.2.3 NP Synthesis

Synthesis of iron oxide nanoparticles with a siloxane poly(ethylene glycol) (PEG) monolayer (IOSPM) was conducted with a method described previously [108]. CP-PEI was conjugated to IOSPM through thiol-ester chemistry. In brief, CP-PEI was first functionalized with iodoacetyl groups using SIA at a 1:10 molar ratio. The excess of SIA was purified using a Zeba spin column equilibrated with thiolation buffer (pH 8.0). IOSPM was simultaneously reacted with Traut's reagent at room temperature for 1 hr; then combined with the purified CP-PEI-SIA overnight before purified through Zeba column equilibrated with 20 mM HEPES buffer (pH 7.4).

6.2.4 NP-siRNA-CTX Preparation

NP and siRNA were mixed in 20 mM HEPES buffer (pH 7.4) for 30 min to allow formation of NP-siRNA complexes. Afterwards, a 1 mg/mL solution of CTX was thiolated through reaction with Traut's reagent at a 1.2:1 molar ratio for 1 hr in the dark at room temperature. Concurrently,

SIA was conjugated to amine functional groups on NP at 1 mg of SIA/mg iron in the dark with gentle rocking for 1 hr. Subsequently the thiolated CTX was reacted with the Iodoacetyl groups on the SIA at 1 mg CTX per 0.9 mg Fe, anchoring CTX to the surface of the siRNA-bound NP to form NP-siRNA-CTX.

6.2.5 NP-siRNA Complex Characterization

Hydrodynamic size and zeta potential analyses of the NP-siRNA complexes in HEPES buffer (pH 7.4) were performed using DTS Zetasizer Nano (Malvern Instruments).

siRNA binding and serum stability were characterized using native polyacrylamide gel electrophoresis (PAGE, Bio-Rad). NP-siRNA complexes were formed as described previously at concentrations corresponding to the W/W ratios (iron weight of NP/siRNA weight) tested (0.5:1, 1:1, 2:1, 5:1, 10:1 and 20:1). While maintaining a uniform concentration of siRNA, NP-siRNA complexes were prepared at NP:siRNA weight ratios ranging from 0:5 to 20:1. The complex were treated with heparin (1000 units/ml, 50 μL Heparin/ 1 μg siRNA) and incubated for 30 min at room temperature to block the electrostatic interaction between NP and siRNA. Both heparin treated and untreated samples were loaded onto the gel and electrophoresis for about 30 min at 120 V. Gels were stained with 0.5 μg/ml ethidium bromide and visualized using a Bio Rad Universal Hood II Gel Doc System.

For serum stability assay, the NP-siRNA complex at a series of weight ratios of NP to siRNA as mentioned above were incubated in a 10:1 volume ratio of medium and fresh serum to give 10% serum concentration and incubated at 37℃ overnight. Then the complexes were treated with heparin before running the polyacrylamide gel. Naked siRNA served as the control.

6.2.6 Cell Culture

All tissue culture reagents purchased from Life Technologies unless specified otherwise. The MGMT-proficient SF763 (activity = 59 ± 3 fmol/10^6 cells, i.e., 35,400 ± 1,800 molecules/cell) and MGMT-deficient A1235 human GBM cell lines were cultured at 37℃ in a humidified atmosphere with 5% CO_2 using Dulbecco's modified Eagle's Medium (DMEM) supplemented with 10 % fetal bovine serum (Atlanta Biologicals) and 1% antibiotic-antimycotic.

6.2.7 In Vitro Cell Transfection

Twenty four hours after plating cells at 30,000 cells per well in 24 well plates, cells were transfected with NP-siRNA at 100 nM of siRNA. After incubation for 24 hr, the transfection medium was replaced with fresh medium, and cells were incubated for an additional 48 hr before analysis. The siRNA targeting green fluorescence protein (GFP) and the ON-TARGET plus siRNA against MGMT (siMGMT) were purchased from GE Dharmacon.

6.2.8 Quantitative RT-PCR (qRT-PCR)

RNA was extracted from cells at 48 hr after siRNA transfection using the Qiagen RNeasy kit. cDNA was prepared using the iScript cDNA Synthesis Kit (BioRad) following the manufacturer's protocol, which was then used as a template for PCR. Quantitative RT-PCR (qRT-PCR) was used to evaluate the relative expression levels of MGMT utilizing human β-actin as a reference gene. SYBR Green PCR Master mix (Bio-Rad) was used for template amplification with a primer for each of the transcripts in a Bio-Rad CFX96 real-time PCR detection system. Quantitative amplification was monitored by the level of fluorescence reflecting the cycle number at the detection threshold (crossing point) using a standard curve. Thermocycling for all targets was carried out in a solution of 20 µl containing 0.5 µM primers and 4 pg of cDNA from the reverse transcription reaction under following conditions: 95 ℃ for 2 min, 40 cycles of denaturation (15 sec, 95 ℃), annealing (30 sec, 58 ℃), and extension (30 sec, 72 ℃). The primers used for β-actin is: 5'-AGCGAGCATCCCCCAAAGTT-3'/5'-GGGCACGAAGGCTCATCATT-3'. The pre-evaluated primers used for MGMT amplification was purchased from Bio-Rad.

6.2.9 Cell Survival Assays

Alamar blue assay was used to evaluate cell viability following the manufacture's protocol (Life Technologies). Briefly, GBM cells were plated and transfected as described previously. AB assay was conducted at 2 days after tranfection. Cells were washed with PBS (pH 7.4) three times before adding 10% AB in complete growth medium to the wells. After incubation for 1 hr,

the AB solution was transferred to a 96-well plate, and fluorescent emissions at an excitation wavelength of 550 nm and an emission wavelength of 590 nm were read on a SpectraMax M5 microplate reader (Molecular Devices).

Clonogenic assay was used to evaluate cell response to drugs. Briefly, GBM cells were treated with control or siMGMT for 48 hr as described above. The cells were then trypsinized, and 250-300 cells were plated per well in six-well plates in normal 10% FBS-containing growth medium in triplicate. Cells were then treated with drugs at 24 hr after plating and cultured for 1-2 weeks before fixation and staining with Methylene Blue (Sigma-Aldrich). Colonies consisting of 50 or more cells were counted.

6.2.10 In Vivo Biodistribution and Serum Half-Life of NP

All animal experiments were conducted in accordance with University of Washington Institutional Animal Care and Use Committee (IACUC) approved protocols as well as with federal guidelines. Wild-type C57 BL/6 mice (Jackson Laboratories) were systemically administrated via tail vein with Dy677 labeled NP-siScrambled-CTX (NP-siScr-Dy677-CTX). The non-injected animal was included as control. Two or forty-eight hours after injection, the animals were euthanized and tissues were dissected from brain, liver, kidneys and spleen. Each tissue was imaged using a Xenogen IVIS Lumina II system (PerkinElmer) to monitor NP distribution.

Blood was collected by retro-orbital eye bleed or terminal heart puncture for blood half-life evaluation at 0.5, 1, 2, 4, 24, and 48 hr after NP injection. Due to the limited amount of blood from each animal, none were used for more than two time points. Blood samples were drawn from four independent mice for each time point. 100 µl of blood was added to a 96 well clear bottom plate, and scanned on the Odyssey NIR fluorescence imaging instrument (LI-COR) using the 700 nm-channel (λ_{exc}=685 nm with λ_{em}= 705 nm). Concentration of NP was interpolated from the NP-siScr-Dy677-CTX fluorescence standard curve.

6.2.11 Immunohistochemistry

Mice brains were collected and fixed in 4% formaldehyde for 24 hr before placed in 30% sucrose until fully saturated. Afterwards, the brains were frozen in OCT embedding medium (Sakura) at -80 ℃ before sectioned using a *cryostat* (Leica Biosystems). Frozen sections (5–10 μm thickness) were stained with primary antibodies (anti-CD31, MGMT, CD44, Nestin, Sox-2) (Abcam) followed by fluorophore conjugated secondary antibody (Abcam), and DAPI was used for nuclei staining. Brain sections were then photographed under a Zeiss 510 META confocal microscope.

6.2.12 In Vivo Toxicity Studies

Wild-type C57 BL/6 mice were injected with NP-siMGMT-CTX through tail vein at 10 μg siRNA daily for 4 days. Twenty-four hours after administration of the last dose, the animals were sacrificed and blood was collected by cardiac puncture. Blood samples were delivered to Phoenix Central Laboratory for hematology analysis. Representative organ tissues from each group were excised and fixed in 10% (v/v) formalin saline and processed for routine histopathological procedures. Paraffin embedded specimen were cut into 8 μm sections and stained with hematoxylin and eosin (H&E) for histopathological evaluations.

6.2.13 Orthotopic Xenograft Tumor Model and Therapy Response Experiments

All xenograft therapy evaluations were conducted using a GBM6 orthotopic tumor model. The human GBM6 tumor was kindly provided by Dr. Jann N. Sarkaria (Mayo Clinic). The procedure for establishing intracranial tumors was described previously [239, 240]. In brief, flank GBM6 tumor xenografts were harvested, mechanically disaggregated and stereotactically injected into the frontal lobe of 6-week-old female NOD-SCID mice (Jackson Laboratories). The injection coordinates are as follows: 3 mm to the right of the midline, 2 mm anterior to the coronal suture and 3 mm in depth. Each animal received 2 μL injections of approximately 1×10^6 cells. At about 4 weeks post-tumor implantation, animals with similar tumor size as evaluated from Magnetic Resonance Imaging (MRI) were randomized to one treatment group consisting of NP-siMGMT-CTX + TMZ, and two control groups consisting of either NP-siGFP-CTX + TMZ or

untreated. 100 µl NP-siRNA via tail vein at a concentration that allowed for 10 µg per mice was performed daily for 4 days. Temozolomide (TMZ, TCI AMERICA) was administered by oral gavage (100 mg/kg mouse weight daily, with methyl cellulose used as the carrier) starting from the second day of the NP-siRNA-CTX injections. All mice used for therapy response evaluations were observed daily and euthanized at the time of reaching a moribund condition.

6.2.14 In Vivo Knockdown of MGMT

MGMT suppression was evaluated by western blot and MGMT activity assays. In brief, mice bearing GBM6 intracranial tumors were injected with NP-siGFP-CTX/NP-siMGMT-CTX through tail vein at 10 µg siRNA daily for 4 days. Untreated mice served as control. Twenty-four hours after the last treatment, animals were euthanized and tumors were isolated and flash froze in liquid N_2.

For western blot assay, tumor tissue were solubilized by incubation for 15 min on ice in 0.1% Triton X-100 in PBS (pH 7.4). Tumor lysis was diluted 1:1 with Laemmli sample loading buffer containing 2% β-mercaptoethanol. After heating at 100 ℃ for 5 min, 10 µg of extract protein was resolved by SDS-PAGE and transferred onto nitrocellulose membranes. Membranes washed three times with TBS were incubated with 3% QuickBlocker (Chemicon) in TBS for 1 hr at room temperature and then incubated overnight at 4 ℃ with 1 µg/mL antibody against MGMT or β-actin (Abcam) in TTBS containing 3% QuickBlocker. Membranes were washed with TTBS before being incubated for 1 h at room temperature with alkaline phosphatase-conjugated goat anti-rabbit secondary antibody (Bio-Rad) diluted 1:3000 in 3% QuickBlocker. Membranes were then washed thrice with TTBS and antibody binding visualized by chemiluminescence (Immun-Star detection kit; Bio-Rad) and quantified using the ChemiDoc system running the Quantity One software package (Bio-Rad).

The MGMT activity assay was conducted in a standard biochemical assay that quantifies the transfer of radioactivity from a DNA substrate containing [methyl^{3}H]O^6-methylguanine (specific activity, 80 Ci/mmol) to protein as detailed previously [241]. Frozen tissue was homogenized followed by sonication in isotonic buffer. DNA was quantified in crude homogenates by the diphenylamine method that measures deoxyribose following degradation of DNA with heat and acid [242]. The homogenates were cleared by centrifugation at 10,000 × g for 30 min. Activity

was normalized to cell number using a conversion factor of 6 pg DNA per human cell. All activities are the mean of at least 4 determinations that generally differed by no more than 20%.

6.2.15 In Vivo Tumor Targeting Evaluation

For evaluation of tumor targeting, mice were administrated with NP-siScr-Dy677-CTX by tail vein injection. Three hours-post injection, brains were collected and imaged using Xenogen IVIS system. Representative brain tissues were processed for frozen sections and stained with DAPI as described previously. Brain slides were imaged using a Nikon ECLIPSE TE2000-S microscope.

6.2.16 In Vivo Apoptosis Analysis

The *in vivo* response to the combination of NP-siMGMT-CTX and TMZ was assessed by determining the level of apoptosis in the tumors using Annexin V assay. Mice with intracranially established GBM6 tumor xenografts were treated following the indicated treatment schedules given in **Figure 32a**, and tumors were isolated on 3 days after the last TMZ treatment. Tumor cells were dissociated and passed through a 70 μm cell strainer (Thermo Fisher Scientific) to acquire single cell suspension. They were then subjected to double staining with GSC marker, anti-CD44-PE (Abcam) and Annexin V (Life Technologies) following the manufacturer's protocol, and analyzed by flow cytometry using a BD FACS Canto flow cytometer. All data were analyzed with Flow Jo.

6.2.17 MRI

Imaging acquisition was started at two weeks after tumor implantation. Mice were anesthetized with isoflurane (Piramal Healthcare), and positioned in an MRI-integrated respiratory system, with nose-cone for anesthetic and oxygen delivery, ear bar head holder, circulating bath for temperature control, abdominal pad for respiratory monitoring (SA Instruments; MR-compatible small animal monitoring and gating system), and vacuum line for expiratory gas extraction. MR images to determine tumor volume were obtained once per week, up to 7 weeks after tumor

implantation. Total session time under anesthesia per mouse was about 15 min. Mice were divided into treatment groups based on maximum tumor width at 4 weeks, with partitioning performed to equilibrate average pre-treatment tumor size between groups. Images were acquired on a Bruker 14 Tesla vertical-bore imaging system (Ultrashield 600 WB Plus), using a 25 mm single-channel ^{1}H radiofrequency receive coil (PB Micro 2.5). A T2-weighted rapid acquisition with refocused echoes (RARE) sequence was used with the following parameters: TR/TE = 4000/27 ms, in-plane resolution = 52 x 78 μm^2, matrix = 384 x 256. 2-D slices of 0.5 mm thickness were used. 14 slices were obtained for each mouse, and centered on the tumor volume as visualized on a localizer sequence. Scanning time for the T2-weighted sequence was about 4 min. Manual regions of interest surrounding the external tumor margin were generated on a slice-by-slice basis using Bruker Paravision imaging software under high-magnification of the acquired images. ROIs were produced by users blinded to the treatment group of each mouse, and inter-user comparison between manually generated ROIs yielded a volume estimate difference < 5%. Scans with reduced slice thickness of 0.2 mm were also obtained on individual tumors, to compare the variability size estimation of small and large tumors using the chosen 0.5 mm slice thickness.

6.2.18 Statistical Analysis

For statistical analysis, acquired data are expressed as mean ± SD. Statistical significance was determined using the Student's *t*-test. Significant values were designated as follows: $P \leq 0.05$. Statistics for overall survival in mouse studies was calculated with the log-rank (Mantel-Cox) test. Statistical significance was established at $P \leq 0.01$.

6.3 RESULTS AND DISCUSSION

6.3.1 Physicochemical Properties of NP

Polycationic polymer based nanoparticles are believed to be feasible siRNA delivery reagents [69, 243]. Previous studies have demonstrated that PEI modified with other bioactive substances, such as chitosan, was able to efficiently deliver DNA with significantly reduced toxicity as

compared to free PEI [102, 244]. Therefore, we proposed to evaluate the feasibility of siRNA delivery using the IOSPM coated with PEI modified by CP. **Figure 24** shows the schematic of CP-PEI coating on IOSPM, herein called NP, and complexation of NP with siRNA through electrostatic interaction between negatively charged siRNA and positively charged polymer coating to generate the NP-siRNA complex. The structure of CP-PEI copolymer was verified by proton NMR (1H-NMR). The characteristic 1H-NMR peak at 3.7 ppm (peak I) representing ethylene group of PEG is resolved on the CP spectrum and ethylenimine (-NH2-CH2-CH2-) repeat unit of PEI is present at 2.6-3.1 ppm (highlighted peaks) (**Figure 24a**).

Site-specific siRNA delivery is extremely important for GBM treatment due to the highly infiltrative and invasive nature of GBM. One effective strategy is through the attachment of targeting ligands such as tumor-targeting antibodies, small molecules, and peptides [245-247]. Chlorotoxin (CTX), a cationic peptide originally purified from the venom of the *Leiurus quinquestriatus* scorpion, is well established in its ability to target GBM [6, 70]. Notably, CTX-targeted NPs are able to bypass BBB and accumulate specifically within brain tumors [8]. Thus, we attached CTX to NP-siRNA and evaluated the physicochemical properties of the resultant NP-siRNA-CTX. The success of CTX conjugation was verified by SDS-PAGE (**Figure 24b**). TEM images revealed well-formed spherical morphologies of the NPs with a core size of 10-12 nm before (**Figure 24c**) and after (**Figure 24d**) cationic polymer conjugations and siRNA loading. Additionally, NPs were well dispersed in aqueous medium without agglomeration, mainly attributed to the PEG in the copolymer coating.

In order to successfully reach tumor sites, NPs have to overcome multiple physiological barriers of the human body, such as liver, kidneys, and spleen. Therefore, hydrodynamic sizes of NP should be between 10 and 100 nm to avoid being eliminated by these clearance organs [154]. To test the ability of the NPs to stably bind siRNA and remain at a desirable size, hydrodynamic size was determined using dynamic light scattering (DLS). NP-siRNA complex had similar size with NP at about 45.5 $\pm$ 2.5 nm **(Figure 24e)**, suggesting the strong complexing capability of NP with siRNA and the ability of NP-siRNA to bypass the physiological barriers. Zeta potential is another important factor indicating NP physicochemical properties [111]. The positive surface charge directly correlates with the capacities of NP to complex and transfect siRNA into cells. NPs exhibited a zeta potential of 27.7 $\pm$ 2.1 mV (**Figure 24f**), mostly corresponding to the

primary amine groups on PEI. In agreement with the hydrodynamic size measurements, zeta potential of NP-siRNA complex was close to NP, demonstrating their high binding efficiency.

siRNA complexation with NPs was also assessed using an electrophoresis mobility assay, where complexation was inferred from the retardation of siRNA mobility. NP-siRNA complexes were prepared at varying NP:siRNA weight ratios before electrophoresing on a polyacrylamide gel. As shown in **Figure 24g**, migration of siRNA was completely retarded at all tested ratios, implying successful binding of siRNA on NPs. To verify the presence of siRNA in complexes, heparin sodium, a competing poly-anion that induces decomplexation of condensed siRNA, was added. As expected, all samples exhibited similar band density with naked siRNA after heparin treatment indicating total release of electrostatically bound siRNA. Incubation of naked siRNA with serum containing medium resulted in fully degradation as indicated by the arrow **(Figure 24g)**. In addition, siRNA was released from complexes after heparin treatment and the band densities were similar across all binding conditions, revealing that NP-siRNA complexes led to complete protection of siRNA against degradation by RNases in serum. The long term stability of NP-siRNA complex in both PBS buffer and cell culture medium containing serum was evaluated by DLS. As shown in **Figure 24h**, NP-siRNA complexes had consistently small sizes in PBS buffer throughout the 16-day's period, while they doubled their sizes after 2 days in serum condition but remained at around 75 nm throughout the rest of the assay time.

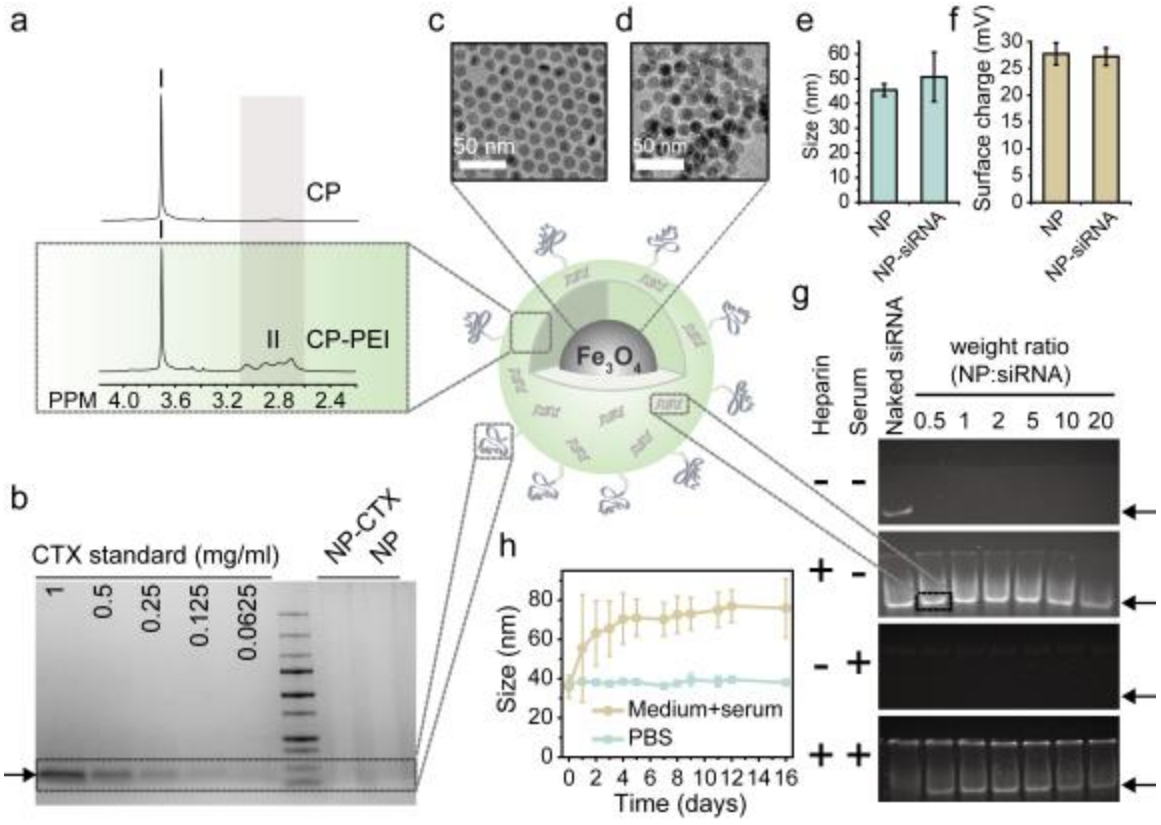

Figure 24. Schematic and characteristics of the NP. (a) Proton NMR analysis of CP and CP-PEI showing the incorporation of PEI onto CP. The characteristic peak of the -O-CH2-CH2- group of PEG (peak I) on CP and -NH2-CH2-CH2- group of PEI (highlighted peak) are all present in the CP-PEI spectrum. All samples were analyzed in D_2O. (b) SDS gel electrophoresis was used to verify CTX binding on NP; TEM images were acquired for IOSPM (c) and NP (d). Hydrodynamic size (e) and zeta potential (f) of NP measured by DLS. (g) Electrophoresis mobility assay analyzing NP-siRNA attachment and siRNA protection by NP from serum at different NP-siRNA weight ratios. (h) Stability of NP-siRNA complex was evaluated in PBS and serum containing cell culture medium.

6.3.2 In Vitro Evaluation of NP-Mediated MGMT siRNA Delivery

Prior to investigating therapeutics of NP-siRNA, we evaluated their cytotoxicity to determine potential side effects. Human SF763 cells were used because of their high MGMT activity [218], which was also confirmed by immunocytochemistry (**Figure 25**). After treatment with NP-

siRNA for 48 hr, about 80% of the cells remained viable as determined by Alamar blue assay, demonstrating the limited cytotoxicity of the NPs (**Figure 26a**).

The gene-silencing efficiency of NP-siRNA was investigated by quantifying MGMT mRNA and protein levels using qRT-PCR and a MGMT biochemical activity assay. As shown in **Figure 26b**, control siRNA had no effect on MGMT expression since the corresponding mRNA level was comparable to untreated cells, whereas siRNA targeting MGMT (siMGMT) resulted in an 80% reduction in mRNA transcripts. This knockdown correlated with a decrease in MGMT activity as there was an 81% decrease in MGMT activity in NP-siMGMT treated cells (**Figure 26c**). MGMT knockdown was also confirmed by immunohistochemistry (IHC), which showed suppressed MGMT protein levels only in NP-siMGMT treated cells (**Figure 26d**).

Having established that NP mediated delivery of siMGMT yields knockdown, their ability to sensitize human GBM cells to TMZ was evaluated using clonogenic assays. As indicated by the clonogenic survival curve in **Figure 26e**, NP-siMGMT transfected SF763 cells became more sensitive to TMZ, while the control siRNA did not alter their TMZ resistance. The LD_{50} was about 14.29 μM, 183.26 μM and 193.15 μM for NP-siMGMT, untreated, and NP-siGFP treated cells, respectively, revealing a greater than 13-fold increase in sensitivity. To test the specificity of MGMT knockdown to TMZ sensitization, the response to doxorubicin and oxaliplatin, which do not methylate DNA, were tested. No increase in sensitivity to either drug was observed in SF763 cells as the slope of survival curves among treatments was identical (**Figure 26f and g**). In addition, no sensitization to TMZ was observed between NP-siMGMT and control treatments in A1235, a human GBM cell line with low MGMT expression [248] (**Figure 26h**). Clinical benefit of GBM treatment with TMZ in patients with methylated *MGMT* promoter has been well recognized [230, 249-251]. The current *in vitro* studies confirm our speculation that NP-siMGMT induced MGMT depletion can improve sensitivity of human GBM cells to TMZ.

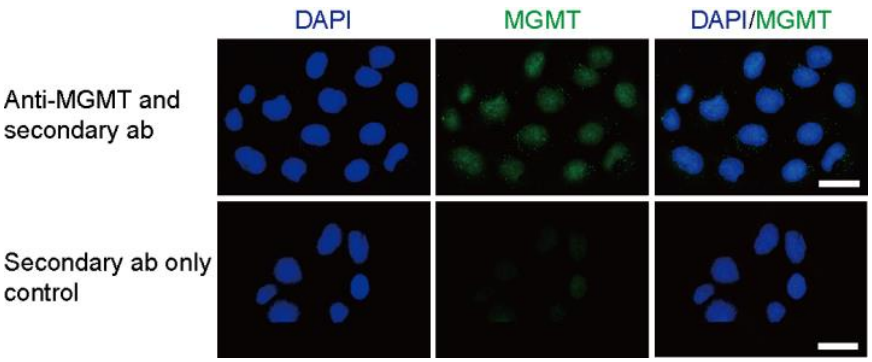

Figure 25. MGMT expression in human SF763 GBM cells. SF763 Cells were labeled with primary antibody (ab) anti-MGMT and FITC-coupled secondary ab (top panel). Cells labeled only with the FITC-coupled secondary ab (bottom panel) were used to confirm that the secondary ab does not bind non-specifically. Blue represents DAPI staining on nuclei. Scale bars, 20 μm.

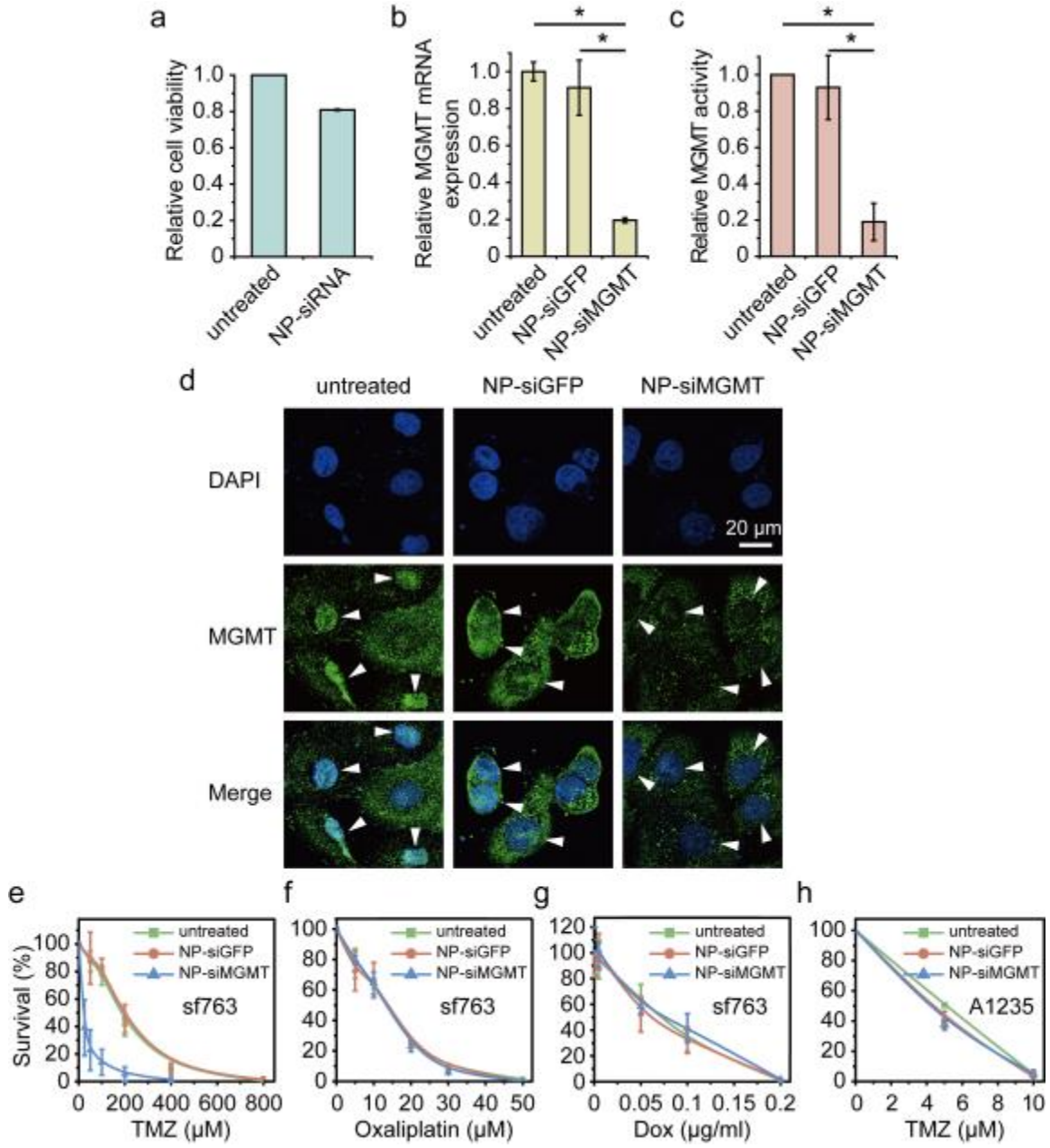

Figure 26. *In vitro* characteristics of NP-siMGMT. (a) Cell viability as a result of NP-siRNA treatment by AB assay. (b) MGMT mRNA expression and protein activity (c) of SF763 cells at 48 hr post NP-siRNA transfection, * represents $p < 0.01$. (d) Confocal laser scanning microscopy fluorescence images of SF763 cells after NP-siRNA treatment. Blue fluorescence represents nuclei labeled with DAPI, green fluorescence represents MGMT. Scale bars = 20 μm. Cell survival of SF763 in response to TMZ (e), doxorubicin (f) and oxaliplatin (g) measured by

clonogenic assay. (h) Clonogenic survival of A1235 to TMZ. Results were from three independent experiments.

6.3.3 Biodistribution and BBB Penetration of NP-siRNA-CTX In Vivo

Prior to evaluating the therapeutic efficacy of NP-siRNA-CTX *in vivo*, we first examined the behavior of NPs in immune-proficient mice. In order to determine biodistribution and BBB penetration of NP delivered siRNA, NPs were loaded with Dy677 fluorophore conjugated siRNA and injected into wild type (WT) black/6 mice using a previously reported non-radioactive approach [252]. Organs were collected prior to, 2 hr post and 48 hr post injection of NPs and imaged using the Xenogen IVIS imaging system to measure NP-mediated siRNA delivery (**Figure 27a**). Two hours post-injection the majority of siRNA on NPs was observed in the liver and some in the kidneys and spleen, as expected with the liver being the main elimination route for NPs of this size. After 48 hr, most siRNA on NPs was no longer apparent in these clearance organs. Quantification of fluorescence intensities in organs revealed a minor amount of siRNA fluorescence remaining after 48 hr in the liver but reached background levels in the kidneys, spleen (**Figure 27b**) and blood (**Figure 28**). This shows the siRNA on the NPs is cleared and eliminated from the body within 48 hr and does not persist in off-target, healthy organs.

Fluorescence images of mice brains were shown in **Figure 27c**. High signal from the fluorophore labeled siRNA was observed in the brain 2 hr after injection and was undetectable after 48 hr, indicating the NPs do not accumulate in healthy brain. To visualize whether the NPs remained in the blood vessels in the brain or were able to cross the BBB, brains were collected at 10 min and 6 hr after injection and frozen sections were prepared for immunostaining of CD31, an endothelial cell marker. Confocal imaging revealed NPs in the brain parenchyma near blood vessels 10 min post-injection, which had mostly cleared by 6 hr (**Figure 27d**). This suggests the NPs are able to cross the BBB as they were observed in the brains of healthy animals, similar to our previous observation in tumor bearing animals [8]. However, NPs did not accumulate in healthy brain as few NPs were observed at 6 hr post-injection and all fluorescent signal vanished after 48 hr. This finding is extremely important for developing more effective GBM treatments as the single cancer cells that have invaded the healthy brain beyond the resection cavity must be

eliminated. A NP that can cross the BBB and penetrate into healthy brain will have the best chance of attaching to these single cancer cells to deliver treatment.

To test the safety of the NPs in healthy animals, we injected animals with NPs daily for four days and measured several standard hematology markers, including white blood cells (WBC), hemoglobin (HGB), hematocrit (HCT), platelets (PLT), mean corpuscular volume (MCV), albumin, alanine transaminase (ALT), aspartate transaminase (AST), alkaline phosphatase (ALP), bilirubin, blood urea nitrogen (BUN), and glucose. No observed toxicity was seen in any of the blood tests indicating the safety of NP-siRNA-CTX (**Figure 27e-p**). Examination of sectioned liver, lung, spleen and heart revealed no structural abnormalities, providing additional evidence that NP-siMGMT-CTX is not grossly cytotoxic (**Figure 29**).

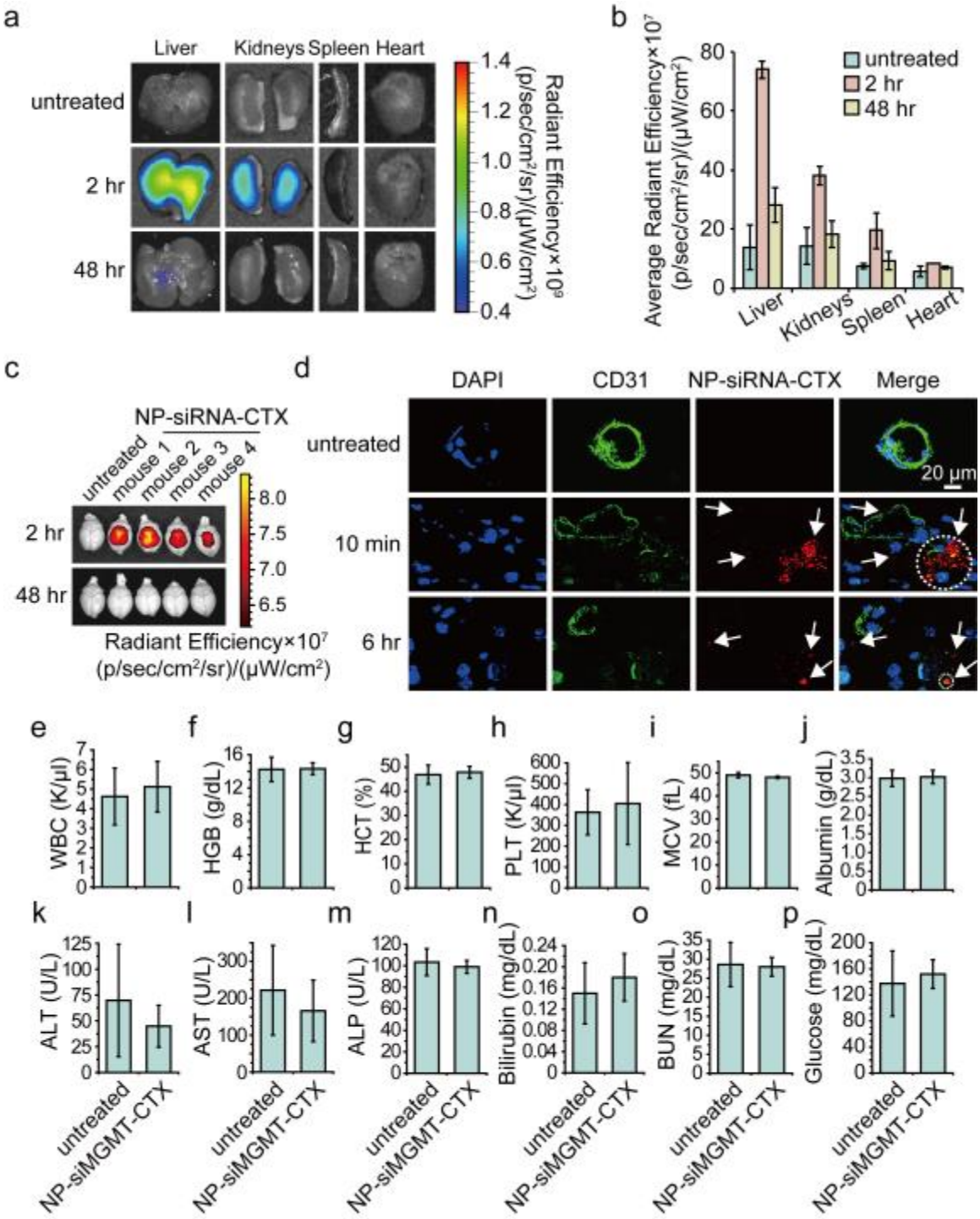

Figure 27. Biodistribution, BBB penetration, and toxicity of NP-siRNA-CTX in wild-type C57 BL/6 mice. (a) Biodistribution of fluorophore labeled siRNA loaded NPs in black/6 WT mice at 2 hr and 48 hr after injection indicated by optical images taken with IVIS Lumina II system. (b)

Fluorescence quantification of NP-siRNA-CTX in different organs, graph bars show mean values ± SD. (c) Accumulation of NP-siRNA-CTX in brains of WT mice at 2 hr and 48 hr after injection (n = 3 per condition. (d) Confocal laser scanning microscopy images of BALB/c WT mice brain tissue sections at different time points post-NP-siRNA-CTX treatment, Blue, nuclei labeled with DAPI; green, endothelial cells stained with anti-CD31 antibody labeled with Alexa 488; red, Dy677-labeled siRNA complexed with NP. Scale bars represent 20 μm. (e-p) Hematology results from untreated and NP-siRNA-CTX treated WT mice at 24hr after the last injection. Bars represent mean ± standard deviation. Abbreviations: WBC, white blood cells; HGB, hemoglobin; HCT, hematocrit; PLT, platelet; MCV, mean corpuscular volume; ALT, alanine transaminase; AST, aspartate transaminase; ALP, alkaline phosphatase; BUN, blood urea nitrogen.

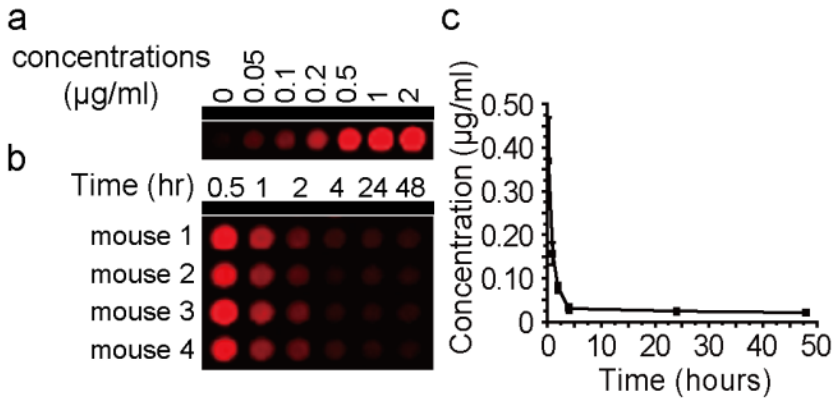

Figure 28. Evaluation of NP concentration in blood circulation. (a) Fluorescence intensity of NP-siScr-Dy677-CTX standard used for quantifying NP concentration in blood using an Odyssey NIR fluorescence imaging instrument. (b) Fluorescence intensity of blood samples as a function of time. (c) Quantification of NP-siScr-Dy677-CTX concentration in the blood over time.

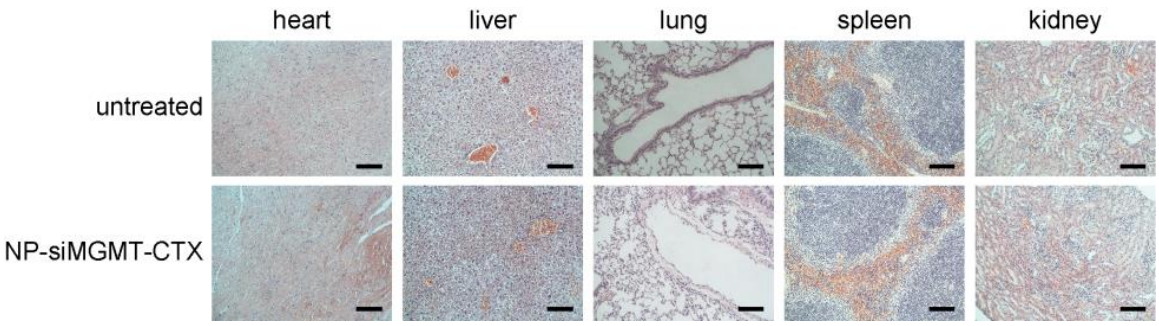

Figure 29. Pharmacological evaluation of NP-siMGMT-CTX. Representative H&E stained tissue sections of mouse heart, liver, lung, spleen, and kidney from untreated animals (top row) and from those injected with NP-siMGMT-CTX (bottom row). Scale bar corresponds to 100 μm.

6.3.4 In Vivo Delivery of MGMT siRNA Suppresses MGMT Activity and Induces Apoptosis in GSC Tumors

An intracranial GBM tumor model from serially passaged orthotopic GBM6 xenografts was used for *in vivo* studies because they retain the heterogeneity of GBMs and are known for their high MGMT activity (**Figure 30**) [239, 240, 253]. Additionally, this primary tumor is a good representative for GSCs [254, 255], which we further validated here through IHC of GSC markers including Nestin, CD44, and Sox-2 [256-259]. The high expression of these three GSC markers confirms the stem-like properties of this tumor model (**Figure 31a**). Brain tumor bearing nude mice injected with fluorophore labeled siRNA loaded NPs were used to visualize NPs in the tumor. After three hours, brain tumors showed significant accumulation of NPs (**Figure 31b**), which were well distributed throughout the tumor based on fluorescence imaging and Perl's Prussian blue staining of brain slices (**Figure 31c and d**).

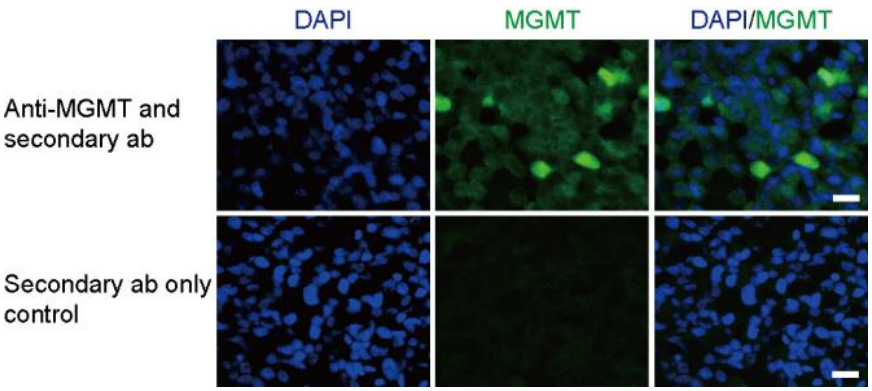

Figure 30. MGMT IHC on brain slides bearing GBM6 tumors. Brain slides bearing GBM6 tumors were labeled with primary antibody (ab) anti-MGMT and FITC-coupled secondary ab (top panel). Tumors labeled only with the FITC-coupled secondary ab (bottom panel) confirmed that the secondary ab does not bind non-specifically. Nuclei were counterstained with DAPI. Scale bars are 50 μm.

To validate the therapeutic efficacy of NP treatment, we randomly sorted mice bearing similar sized GBM6 tumors, as determined by MRI, into three groups: untreated (control), NP-siGFP-CTX+TMZ, and NP-siMGMT-CTX+TMZ. NPs were administrated intravenously according to the scheme in **Figure 32a**. Firstly, to determine if NPs taken up into the tumor could deliver siRNA intracellularly to knock down MGMT expression, tumors were removed from animals and MGMT expression analyzed by Western blot and activity measured using a biochemical assay. NP-siMGMT-CTX treated animals showed significantly reduced MGMT expression and activity (**Figure 31e and f**) indicating the NPs delivered functional siRNA into the RNAi pathway.

GSCs are implicated in tumor initiation, propagation, recurrence, and resistance to chemotherapy and radiation [260, 261]. To further characterize the antitumor response of the combination treatment and to identify a mechanism of tumor regrowth, the degree of induced apoptosis in the GSC and non-GSC population of GBM6 intracranial tumors was determined through Annexin V and CD44 co-staining. CD44 has been employed as a GSC marker of GBM [256, 257] as its expression is closely correlated with the histopathologic grade of GBM and the tumor-initiating capacity of GSC [256, 262, 263]. Tumors from all animals were collected and disaggregated 3 days after the completion of NP-siRNA-CTX and TMZ treatment (8 days after

the start of treatments). Single cell suspensions were stained using anti-CD44 antibody (PE) and Annexin V (Alexa 647) and analyzed using flow cytometry. Flow cytometry revealed that tumor cells from mice treated with NP-siMGMT-CTX displayed significantly more Annexin V stained cells that expressing CD44 than untreated or NP-siGFP-CTX treated controls (**Figure 31g**). This indicates the NPs are able to target the GSC population of cells and induce greater sensitivity towards TMZ. Previous studies demonstrated that GBM GSCs are resistant to TMZ due to mechanisms such as ABCG2 overexpression that removes TMZ from cells [264], or *TP53* mutation and BCL-2 overexpression that lead to resistance to apoptosis [265, 266]. Therefore, a combination siRNA treatment strategy will likely be required to affect this resistant population of cells.

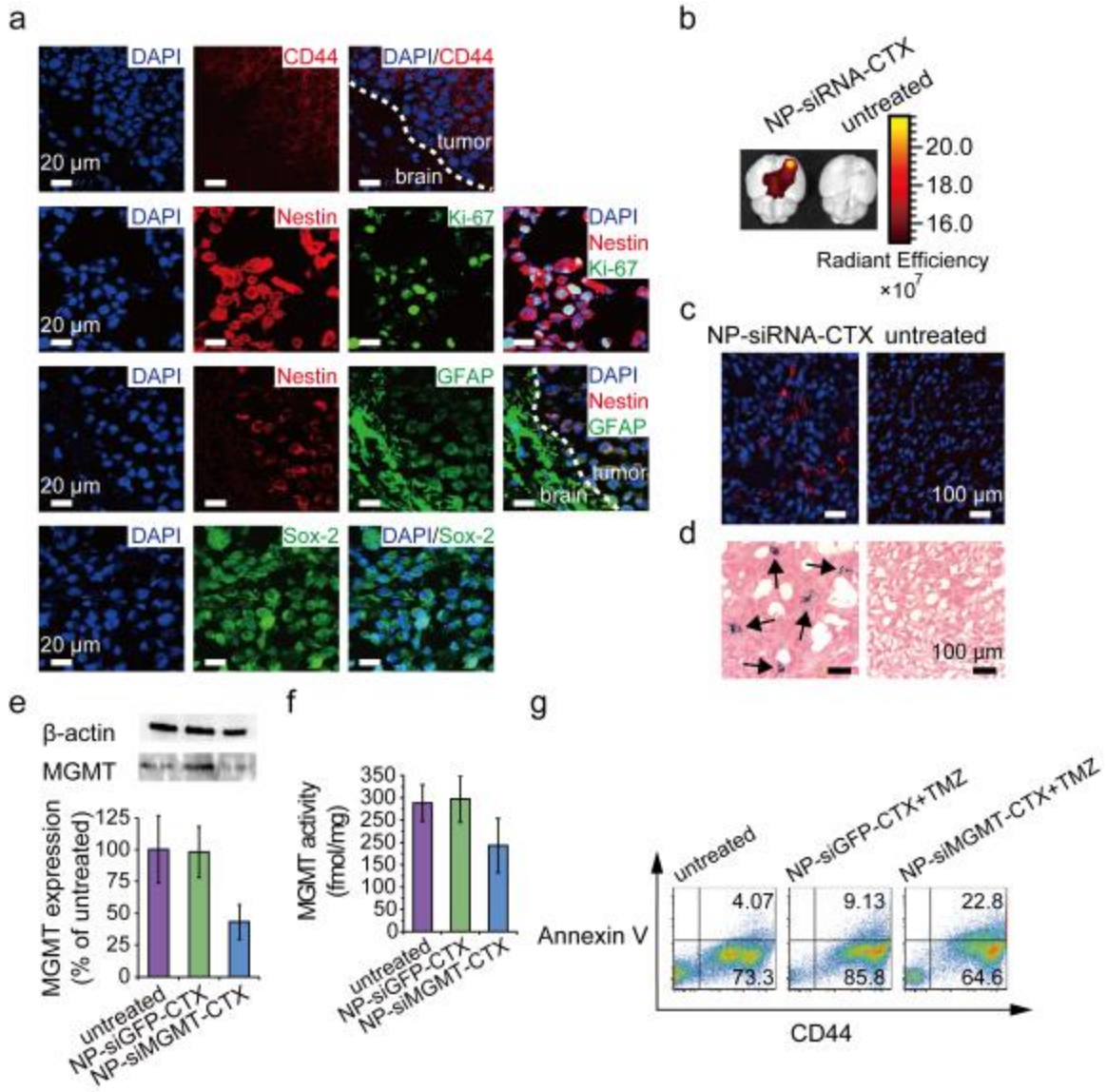

Figure 31. NP-siMGMT-CTX sensitizes GBM6 xenograft cells expressing GBM stem cell (GSC) markers to TMZ. (a) Immunofluorescence of GBM6 tumor slides. GSC markers CD44, Nestin, and Sox-2, differentiation marker GFAP, proliferation marker Ki67 [267] and DAPI staining were conducted on GBM6 tumor under different combination. Scale bars represent 20 μm. (b) Xenogen IVIS fluorescence images of brains from nude mice bearing GBM6 tumors at 3 hr after injection. (c) Representative fluorescence microscopy images of brain sections demonstrate Dy755 labeled NP-siRNA-CTX (red) distribution in tumor. Scare bars represent 100 μm. (d) Accumulation of NP-siRNA-CTX in tumor as revealed by Prussian blue staining. The scale bars represent 100 μm. (e) Western blot analysis of MGMT and β-actin protein levels from

GBM6 intracranial tumors 24 hr after the last treatment with either NP-siGFP-CTX or NP-siMGMT-CTX. Densitometric quantification of the Western blot is shown in the lower panel in which MGMT expression is compared to that of the untreated control. (f) MGMT activity of GBM6 intracranial tumors at 24 hr post the last treatment with NP-siGFP-CTX or NP-siMGMT-CTX. (g) Flow cytometry analysis of apoptosis in GBM6 GSC by anti-CD44 and Annexin V double staining. Numbers indicate the percentages of Annexin V-positive and negative cells in CD44 positive GBM6 tumors treated with NP-siGFP-CTX+TMZ, NP-siMGMT-CTX+TMZ or left untreated. Experiments were repeated three times.

6.3.5 In Vivo Delivery of MGMT siRNA Extends Survival and Decreases Tumor Burden

Examination of tumor growth rate after treatment was conducted using high-resolution MRI. Tumor-bearing mice were followed with serial MR scans starting two weeks after implantation of GBM6 cells. T2-weighted images of two representative examples of tumor development from each group are shown in **Figure 32b**. The initiation of tumor formation at around week 4 is indicated as the arrows. The rapidly expanded tumor from untreated and control siRNA treated groups corresponds to their growth curve. The NP-siMGMT-CTX + TMZ treated animals showed obviously smaller tumors at week 7. H&E histology on brain tumor slides confirms the accuracy and reliability of MRI quantification. Together these results revealed a correlation between improved survival and reduction in tumor burden. Tumor growth curves for all included mice are displayed in **Figure 32c**. The treatment of mice was selected to begin at week 4 after implantation (black arrow), at which time tumor growth was visualized on MRI in all mice (average volume 2.7 mm^3). The examination of the group averages of tumor size demonstrates a relative similarity of growth curves between the control NP-siGFP-CTX + TMZ group and untreated group. At 6 weeks, the average tumor size of the NP-siMGMT-CTX + TMZ treated mice was 11 ± 3.3 cm^3, compared to an average tumor size of 61 ± 16 cm^3 for the aggregate 5 mice in the two control groups, a 5.5-fold reduction in tumor volume. Between 6-7 weeks, 2 of 3 mice in the untreated group met criteria for sacrifice due to critical tumor-related illness. Accordingly, the final data point in the untreated group reflects the tumor size of a single surviving mouse. We also noticed the tumor in one of the NP-siMGMT-CTX treated mice almost disappeared. This data point likely underestimates the extrapolated size of untreated

tumors at week 7, assuming that critical illness had not limited the continued monitoring of these mice.

We then tested the survival benefit of mice receiving NP-siMGMT-CTX in combination with TMZ. Both untreated mice and mice receiving both control NP-siGFP-CTX and TMZ exhibited the same survival rate of 11.5 ± 1.9 and 10.1 ± 2.5 days, respectively (**Figure 32d**). Treatment with NP-siMGMT-CTX and TMZ led to a significant improvement in animal survival as compared to both untreated and control siRNA treated animals, achieving a 3-fold extended median survival (37.8 ± 7.7, $P < 0.01$). Notably, one animal survived almost 80 days after its tumor nearly disappeared. This treatment strategy could have a dramatic impact in the treatment of GBM patients with unmethylated MGMT promoters to give them the same survival benefit with TMZ as patients with methylated MGMT promoters.

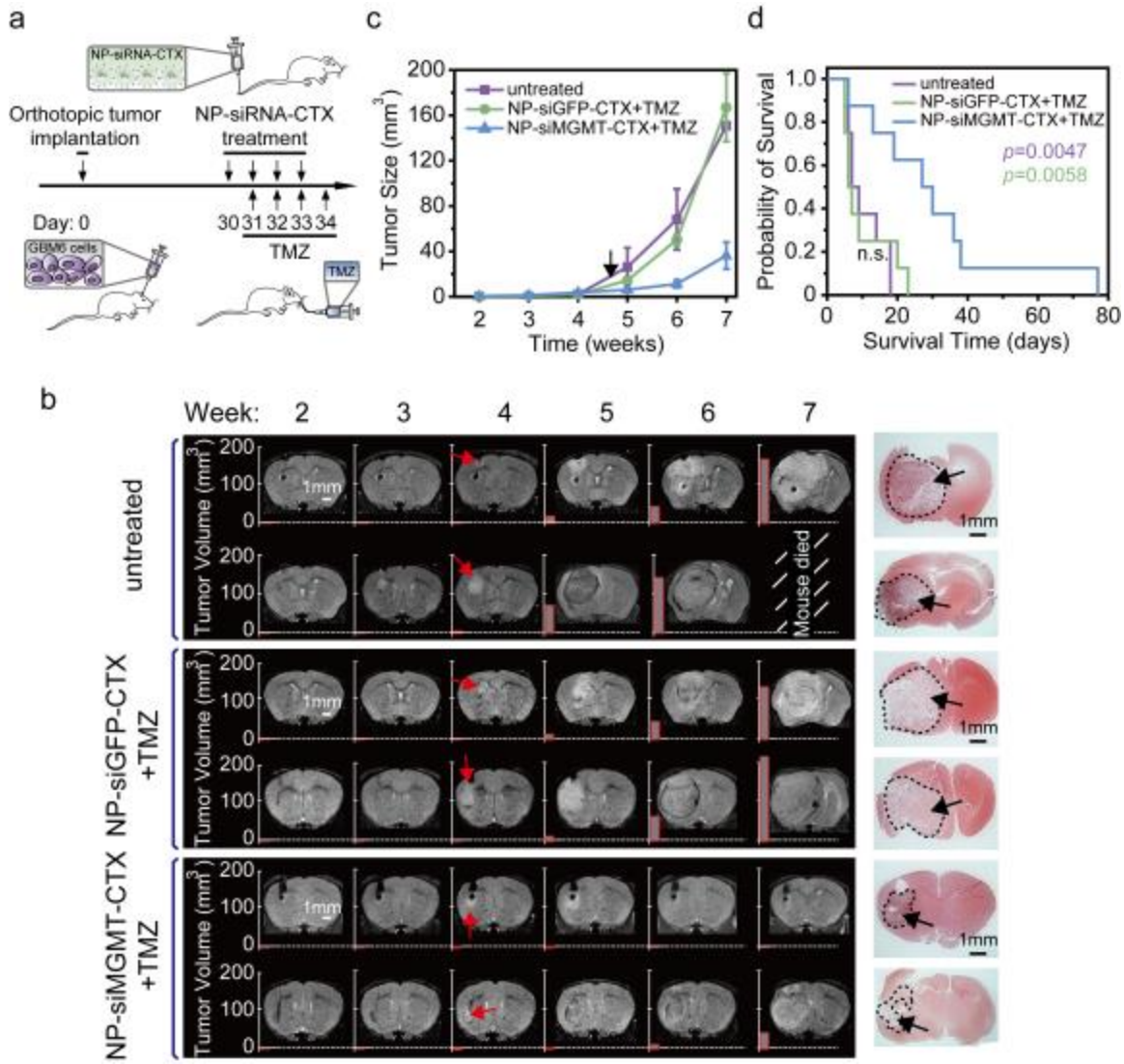

Figure 32. NP-siMGMT-CTX increases TMZ sensitivity and prolongs survival. (a) Scheme of tumor implantation and NP-siRNA-CTX+TMZ treatment. Mice were orthotopically injected with GBM6 cells for tumor formation (day 0) followed by four intravenous injections of NP-siRNA-CTX and four TMZ treatments through oral gavage. (b) Representative examples of tumor development obtained from untreated control group, NP-siGFP-CTX+TMZ control group, and NP-siMGMT-CTX+TMZ group. T2-weighted images for each mouse are displayed over the full time course of imaging, from week 2 post-tumor implantation until week 7. Tumor volume at each week, as calculated over the entire 3-dimensional extent of the mass, is displayed in the bar graph alongside corresponding images. Note that the images displayed are the individual slice of maximum tumor diameter. Red arrow in each row marks the first appearance of tumor

for each mouse. H&E staining was conducted on brain slides from animals at the end of survival studies. (c) Average tumor sizes for treatment and control conditions. Black arrow indicates the start of treatment. Open square data point in untreated group highlights the presence of only one surviving mouse at this time point. Error bars represent standard deviation. (d) Kaplan-Meier survival curves of untreated mice (n = 8) and mice treated with NP-siGFP-CTX + TMZ (n = 8) and NP-siMGMT-CTX + TMZ (n = 8). *P* value was calculated with the log-rank test.

6.4 CONCLUSIONS

In summary, we designed a polycationic copolymer based superparamagnetic nanovector. The NP was demonstrated to be capable of efficiently condensing siRNA and the complex displayed excellent stability and payload protection in serum. NP-mediated silencing of MGMT using siRNA significantly sensitized GBM cells to TMZ *in vitro* and extended survival of animals bearing GBM6 tumor *in vivo*. The systemic administration of MGMT-specific NP to intracranial tumor also exhibited selectivity and favorable toxicity, which may enable the siRNA delivery to GBM patients. Considering the urgent need of novel therapeutics for GBM treatment and lack of efficient RNAi delivery strategies, such findings establish the NP system as a promising gene therapy agent for GBM.

7. THREE-DIMENSIONAL SCAFFOLDS AS IN VITRO TUMOR MODELS FOR THE EVALUATION OF NANOPARTICLE-MEDIATED GENE DELIVERY

The cationic nanoparticles (NPs) for targeted gene delivery is conventionally evaluated using 2D *in vitro* cultures. However, this does not translate well to corresponding *in vivo* studies because of the marked difference in NP behavior in the presence of the tumor microenvironment. In this study, we investigated if prostate cancer (PCa) cells cultured in three-dimensional (3D) chitosan-alginate (CA) porous scaffolds could model cationic nanoparticle-mediated gene targeted delivery to tumors *in vitro*. We assessed i*n vitro* tumor cell proliferation, formation of tumor spheroids, and expression of marker genes that promote tumor malignancy in CA scaffolds. The efficacy of NP targeted gene delivery was evaluated in PCa cells in 2D cultures, PCa tumor spheroids grown in CA scaffolds, and PCa tumors in a mouse TRAMP-C2 flank tumor model. PCa cells cultured in CA scaffolds grew into tumor spheroids and displayed characteristics of higher malignancy as compared to those in 2D cultures. Significantly, targeted gene delivery was only observed in cells cultured in CA scaffolds whereas cells cultured on 2D plates showed no difference in gene delivery between targeted and non-target control NPs. *In vivo* NP evaluation confirmed targeted gene delivery indicating that only CA scaffolds correctly modeled NP-mediated targeted delivery *in vivo*. These findings suggest that CA scaffolds serve as a better *in vitro* platform than 2D cultures for evaluation of NP-mediated targeted gene delivery to PCa.

7.1 INTRODUCTION

Prostate cancer (PCa) is the second leading cause of cancer death among the male population in the United States with approximately 29,000 deaths each year [268]. Current treatment for PCa often involves radical prostatectomy, radiation, and hormone therapy [269]. Surgery is highly invasive and might increase the risk of metastasis, whereas radiation therapy generates systemic toxicity [270, 271]. Additionally, PCa can develop resistance to hormone therapy, leading to the

relapse of fatal hormone refractory cancer [272, 273]. Substantial efforts have been devoted to identifying novel treatment modalities, among which gene therapy is particularly appealing as it holds a number of advantages over traditional therapies, including the ability to overcome drug resistance, reduced systemic toxicity, and most importantly, improved target specificity [81]. Several clinical trials that used suicide genes, immunomodulatory genes, and tumor suppressor genes have demonstrated the potential of gene therapy for PCa [273, 274]. Nevertheless, translation of potential therapeutics into the clinic remains challenging due to the lack of a safe and efficient delivery strategy [275, 276].

Nanoparticles (NPs), including gold NPs, quantum dots, liposomes, and polymer-based nanovectors, have been extensively studied as gene delivery vehicles [277, 278]. Superparamagnetic iron oxide NPs have shown significant promise as gene delivery vehicles that can be tracked using magnetic resonance imaging [6, 154]. Typically, NP development is initiated with *in vitro* analysis using two-dimensional (2D) cell cultures followed by extensive *in vivo* evaluation in animals prior to clinical trials. However, successful NP delivery observed in 2D cell culture studies does not usually translate well to *in vivo* studies due to the intrinsic limitation of 2D monolayer cultures that fail to account for the extracellular barriers that are present *in vivo* [73].

To bridge the gap between *in vitro* and *in vivo* analyses, three-dimensional (3D) cell cultures are being developed because they can provide a more realistic model of the *in vivo* tumor microenvironment than cells in 2D culture [5, 74]. There are many types of 3D cell culture systems that are mostly scaffolds composed of natural materials such as collagen, gelatin, and polysaccharides, as well as synthetic materials such as polystyrene, polycaprolactone, and poly(lactic-co-glycolic acid) [75, 279-281]. Of note, we have demonstrated that 3D porous scaffolds composed of a polyelectrolyte chitosan–alginate (CA) complex are able to mimic the tumor microenvironment and improve the tumorigenic potential of cultured cancer cells, including PCa [9, 10, 282-284]. Both chitosan and alginate are FDA approved for broad tissue engineering applications in view of their biocompatibility, biodegradability, and limited immunogenicity [285, 286]. Their structure resembles glycosaminoglycans (GAGs), which are essential components of the extracellular matrix (ECM) [287], which makes these polymers promising choices for *in vitro* modeling of the tumor microenvironment.

We hypothesized that PCa cells cultured in 3D CA scaffolds can better replicate the response to targeted gene delivery *in vivo* and thus can be used in preclinical studies to reduce the number of animals required for preclinical tests. In this study, we assessed i*n vitro* tumor cell proliferation, formation of tumor spheroids, and expression of marker genes that promote tumor malignancy in CA scaffolds. We then assessed the NP–mediated gene transfection in PCa cells in CA scaffold culture systems as compared with those in PCa tumors *in vivo*.

7.2 EXPERIMENTAL

7.2.1 Materials

All chemicals and reagents were purchased from Sigma-Aldrich and all tissue culture reagents were purchased from Life Technologies unless otherwise specified.

7.2.2 Plasmid DNA Preparation

The plasmid pDsRed-Max-N1 vector containing red fluorescent protein (RFP) encoding DNA under the control of the cytomegalovirus (CMV) promoter was purchased from Addgene [288], and was propagated in DH5α E. Coli and purified using the Plasmid Giga Kit (Qiagen).

7.2.3 Scaffold Synthesis

CA scaffolds were prepared as described previously [9, 289]. Briefly, 4 wt % CA *solutions were* casted in molds and lyophilized prior to being cut in 2 mm thick disks and crosslinked in 0.2 M $CaCl_2$ solution. The CA scaffolds were then washed with excess deionized water and sterilized in 70% ethanol overnight. The scaffolds were then washed three times with Dulbecco's phosphate-buffered saline (DPBS), immersed in 500 mL DPBS, and shaken on an orbital shaker at 100 rpm overnight to remove remaining ethanol.

7.2.4 NP Synthesis

PEG-grafted-chitosan (CP) copolymer and NPs were synthesized using the methods reported previously [6, 165]. Briefly, CP-coated iron oxide NPs were prepared in presence of CP by co-precipitation of ferrous and ferric chlorides with ammonium hydroxide followed by buffer exchange into thiolation buffer (0.1 M sodium bicarbonate, pH 8.0, 5 mM EDTA) through S-200 Sephacryl resin (GE Healthcare). PEI (1.2 kDa) was conjugated to NPs through the formation of a thioether bond between 2-iminothiolane (Traut's Reagent, Molecular Biosciences) modified NPs and succinimidyl iodoacetate (SIA, Molecular Biosciences) modified PEI, then NPs purified to remove excess PEI through size exclusion chromatography using S-200 Sephacryl resin equilibrated with 20 mM HEPES buffer (pH 7.4). NPs were then complexed with RFP encoding plasmid DNA at a NP:DNA weight ratio of 10:1 by mixing NPs and DNA in reaction buffer (20 mM of HEPES, pH 7.4) for 30 min. Chlorotoxin (CTX, Alamone Laboratories) was conjugated to DNA-loaded NPs using NHS-PEG12-maleimide (Thermo Scientific). Finally, unreacted CTX was washed away using S-200 Sephacryl resin equilibrated with 20 mM of HEPES buffer (pH 7.4) to form NP-CTX.

7.2.5 Cell Culture

Mouse TRAMP-C2 (TC-2) PCa cells were purchased from American Type Culture Collection. TC-2 cells were cultured in Dulbecco's Modified Eagle's Medium (DMEM) supplemented with 10% FBS, and 1% penicillin/streptomycin at 37 ℃ in a humidified atmosphere with 5% CO_2. The medium was changed every 2–3 days. For CA scaffold culture, 50,000 cells were seeded on each scaffold in 12-well plates and allowed to grow for 10–14 days to form tumor spheroids before conducting transfection. The medium was changed every 3–4 days. TC-2 cells were seeded at 50,000 cells per well in 12-well plates as 2D control for all in vitro assays, and they were subcultured every 4 days once they reached confluency.

RFP expressing TC-2 cells ($TC\text{-}2^{RFP}$) were generated by transfecting TC-2 cells with pDsRed-Max-N1 plasmid using Lipofectamine 2000 following the manufacture's protocol (Life Technologies). Three days after transfection, the regular DMEM medium was replaced by DMEM containing 1 mg/ml G418 disulfate (TOKU-E). Cells were maintained in the selective

medium for three weeks prior to sorting with a BD FACSAria II cell sorter (BD Biosciences). The stably transfected TC-2^{RFP} cells were cultured in a complete medium supplemented with 0.5 mg/ml G418 disulfate.

7.2.6 Live Cell Imaging

TC-2^{RFP} cells grown on 2D and in CA scaffolds were imaged at 10× and 20× magnification with a phase contrast fluorescence microscope (Nikon ECLIPSE TE2000-S).

7.2.7 Cell Proliferation Assay

The Alamar blue (AB) assay was used to evaluate cell proliferation on both 2D cultures and CA scaffolds following the manufacture's protocol (Life Technologies). Briefly, cells were cultured as described above. Cells were washed with DPBS three times before adding 10% AB solution in the complete growth medium to the wells. The samples were incubated at 37℃ for a predetermined time for each culture method (3 hr for 2D cultures and 4.5 hr for CA scaffolds). Then the AB solution was transferred to a 96-well plate, and the fluorescence at an excitation wavelength of 556 nm and an emission wavelength of 586 nm was measured on a SpectraMax M5 microplate reader (Molecular Devices). The cell number was calculated according to standard curves generated separately for 2D cultures and CA scaffold cultures.

7.2.8 Evaluation of CTX Binding Efficiency In Vitro

Flow cytometry was used to assess the binding efficiency of CTX in PCa cells. Alexa Fluor 647 (AF647, Life Technologies) was conjugated to CTX according to the manufacturer's protocol. In brief, 160 μg of AF647 was mixed with 0.5 ml of 1 mg/ml CTX, and reacted for 1 hr at room temperature (pH 8.0) to form the CTX-AF647 conjugates. Unreacted fluorophore was removed using Zeba spin desalting columns (Thermo Scientific) and the number of AF647 per CTX was quantified by UV-Vis. TC-2 cells on 2D culture were incubated with CTX-AF647 conjugates at CTX concentrations of 1 μM, 2 μM and 4 μM. Free AF647 was used at the fluorophore concentrations equivalent to that on CTX-AF647 conjugates. Incubation was conducted for 1 hr

at 37 ℃, and then cells were washed and collected for flow cytometry analysis. At least 10,000 cells from each condition were analyzed. Experiments were repeated three times.

7.2.9 In Vitro Gene Transfection

For 2D conditions, 24 hr after plating TC-2 cells at a concentration of 50,000 cells/ml (0.5 ml/well) in 12 well plates, transfection was performed by replacing the cell culture medium with 0.5 ml of NP:DNA complex-containing medium (2 μg plasmid DNA per well). After 4 hr of transfection, the complex-containing medium was removed and replaced with the regular cell culture medium. For cells growing in CA scaffolds, the medium was removed and 50 μl of NP:DNA complex was added drop-wise onto the tops of scaffolds with 4 μg plasmid DNA per well. 2 ml of fresh medium was added to each well 4 hr later.

7.2.10 Quantitative RT-PCR (qRT-PCR)

RNA was extracted from TC-2 cells cultured in CA scaffolds for 12 days using the Qiagen RNeasy kit. cDNA was prepared using the iScript cDNA synthesis kit (Bio-Rad) following the manufacturer's protocol. Mouse β-actin served as the house-keeping gene. SYBR Green PCR Master mix (Bio-Rad) was used for template amplification with a primer for each of the transcripts in a Bio-Rad CFX96 real-time PCR detection system. Quantitative amplification was monitored by the level of fluorescence reflecting the cycle number at the detection threshold (crossing point) using a standard curve. Thermocycling for all targets was carried out in a solution of 20 μl containing 0.5 μM primers (Integrated DNA Technologies) and 4 pg of cDNA from the reverse transcription reaction under following conditions: 95 ℃ for 2 min, 40 cycles of denaturation (15 sec, 95 ℃), annealing (30 sec, 58 ℃), and extension (30 sec, 72 ℃). The primers are listed in Table 1. Relative gene expression was analyzed using the 2 (*–delta delta* C(T)) method.

Table 1. Primers used for qRT-PCR

Genes	Forward	Reverse

β-actin [290]	CGGTTCCGATGCCCTGAGGCTCTT	CGTCACACTTCATGATGGAATTGA
Col1a1 [291]	GCAACAGTCGCTTCACCTACA	CAATGTCCAAGGGAGCCACAT
Laminin α5 [292]	ACCCAAGGACCCACCTGTAG	TCATGTGTGCGTAGCCTCTC
Snail [293]	TCCAAACCCACTCGGATGTGAAGA	TTGGTGCTTGTGGAGCAAGGACAT
Slug [293]	CACATTCGAACCCACACATTGCCT	TGTGCCCTCAGGTTTGATCTGTCT
Sip1 [294]	ATGGCAACACATGGGTTTAGTGGC	ATTGGACTCTGAGCAGATGGGTGT
TWIST [295]	AATTCACAAGAATCAGGGCGTGGG	TCTATCAGAATGCAGAGGTGTGGG
E-cadherin [296]	AAGTGACCGATGATGATGCC	CTTCTCTGTCCATCTCAGCG

7.2.11 Animal Model

All animal studies were performed in accordance with the University of Washington Office of Animal Welfare guidelines for the use of animals, and all procedures were reviewed and approved by the Institutional Animal Care and Use Committee. For the flank syngeneic model, 8-week-old female black-6 mice (Jackson Laboratories) were anesthetized using 1.5% inhaled isoflurane and one million TC-2 cells were injected into the right flank of the animal in Matrigel matrix (BD Biosciences). Imaging was performed using an IVIS Lumina II system (PerkinElmer) to monitor RFP expression.

7.2.12 Scanning Electron Microscopy (SEM)

Samples for SEM analysis were fixed with 2.5% glutaraldehyde in fully supplemented media for 30 min at 37 ℃. The samples were then fixed in 2.5% glutaraldehyde in 0.1 M sodium cacodylate buffer overnight at 4 ℃. The samples were dehydrated in a series of ethanol washes (0%, 30%, 50%, 70%, 85%, 95%, 100%), with each wash performed twice. The samples were critical point dried, mounted, and sputter coated with platinum, and then imaged with a JSM-7000F SEM (JEOL).

7.2.13 Histological Analysis

CA scaffolds containing TC-2 tumor spheroids were fixed in 4% formaldehyde for 24 hr and placed in 30% sucrose until fully saturated. Afterwards, the scaffolds were cut into small pieces and frozen in optimal cutting temperature compound (OCT) embedding medium (Sakura) at –80 ℃. The frozen sections (12 μm thickness) were stained with hematoxylin and eosin (H&E) and photographed under a Nikon ECLIPSE TE2000-S microscope.

7.2.14 Statistical Analysis

All of the data was statistically analyzed to express the mean ± standard deviation (SD) of the mean. Statistical significance was set at $p < 0.05$ and tested with Student's *t*-test.

7.3 RESULTS AND DISCUSSION

7.3.1 Characterization and Growth Features of TC-2 PCa Cells Cultured in 2D and 3D

A 3D culture system should offer an environment in which the alterations of tumor cell phenotype are similar to those associated with tumor progression [297, 298]. It is therefore critical to assess the development of a tumor-like structure in CA scaffolds to evaluate their potential as an *in vitro* model for cancer research. Cell growth patterns and morphological changes were monitored after mouse TC-2^{RFP} PCa cells were cultured in 2D TCPs and 3D CA scaffolds. TC-2^{RFP} tumor spheroids were observed in CA scaffolds (**Figure 33**). In contrast, TC-2^{RFP} cells in 2D cultures in TCPS exhibited characteristics of adherent epithelial cells. The morphology of TC-2^{RFP} cells was also observed with SEM. TC-2 cells in 2D cultures grew as flat monolayers (**Figure 34a and b**), whereas they formed tumor spheroids in the pores of the porous CA scaffolds (**Figure 34c and d**) and grew to >100 μm in diameter in 12 days (**Figure 34d**). This was further confirmed by H&E staining of a cross section of the scaffold, where tumor spheroids were located both inside (**Figure 35a-b**) and towards the exterior (**Figure 35c-d**) of CA scaffolds. The ability of PCa cells to form tumor spheroids in 3D cultures demonstrated that CA scaffolds provided a better mimic of the *in vivo* tumor environment than 2D cultures.

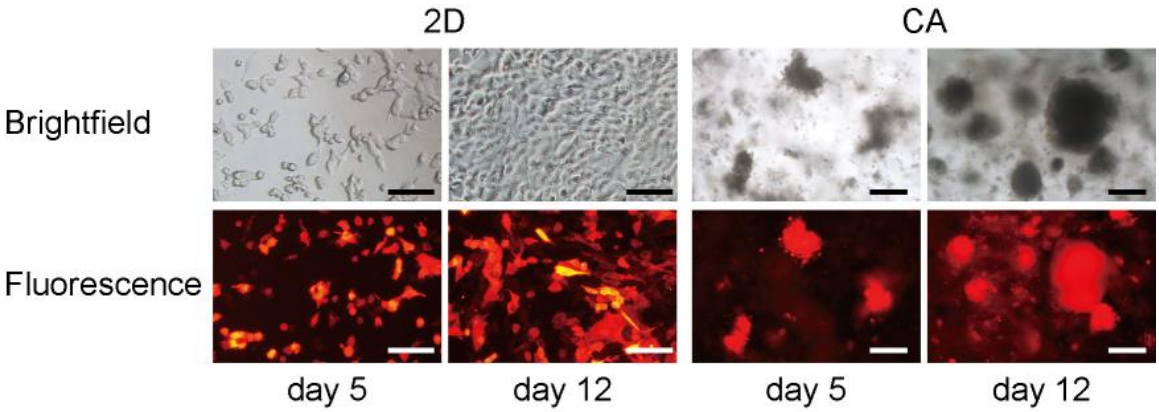

Figure 33. Optical (top row) and fluorescent (bottom row) images of the tumor cells/spheroids of TC-2^{RFP} cultured in 2D cultures and CA scaffolds for 5 and 12 days. Scale bars represent 100 μm.

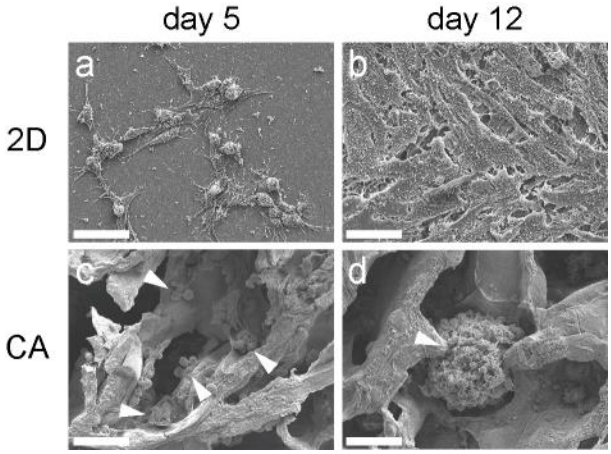

Figure 34. SEM images of TC-2 cells cultured in 2D (a-b) and CA scaffolds (c-d) for 5 and 12 days. Scale bars represent 50 μm.

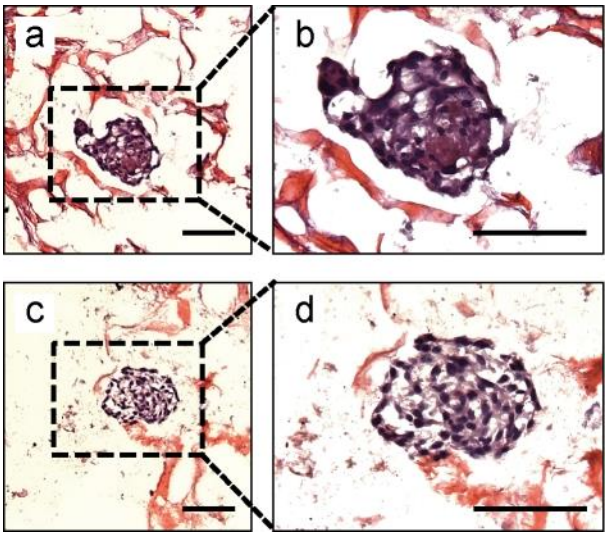

Figure 35. H&E staining of TC-2 tumor spheroids grown in CA scaffolds for 12 days. Tumor spheres were observed (a-b) inside and (c-d) close to the surface of scaffolds. Scare bars represent 100 μm.

Although cancer research has been mainly conducted using cells cultured as monolayers on TCPS, the distinct physicochemical properties of 3D cell culture platforms can efficiently bridge the simplified *in vitro* 2D models and complex *in vivo* models [73, 74]. Various engineering methods have been developed to facilitate tumor spheroid formation. Tumor cells can form aggregates when confined in "hanging drops", in rotating-wall vessels on orbital shakers, or centrifuged in well plates with round or conical bottoms [299-302]. However, many of these systems were designed for cells to self-aggregate to form spheroids generating loose pack of cells without the distinct features of tumors. In the current study, TC-2 cells were trypsinized and resuspended as single cell suspensions before seeding onto CA scaffolds. CA scaffolds have pore sizes of 100–300 μm [289]. Observed under the microscope, cells were well distributed throughout the entire scaffolds after seeding. Therefore, we speculated that unlike the other 3D culturing systems, the naturally formed tumor-like spheroids observed in CA scaffolds originated from single PCa cells. We proposed that cell-cell interactions, production of ECM, and cell proliferation from the exterior to the spheroid center in CA scaffolds are more representative of what occur in the tumor milieu *in vivo*. We have previously demonstrated that in addition to maintaining tumor cell morphology, CA scaffolds can also increase tumor cell malignancy [9,

10, 284]. This further emphasized the important role of CA scaffolds as an *in vitro* tumor culture system that can better represent the tumor microenvironment than 2D TCPS.

7.3.2 PCa Cell Proliferation in CA Scaffolds

To further evaluate the behavior of cancer cells in the CA culture system, we monitored the growth kinetics of the naturally formed TC-2 tumor spheroids. Cell proliferation in 2D and CA cultures was determined using the AB assay. TC-2 cells in 2D cultures had a high proliferation rate and became highly confluent in three days (**Figure 36**), which corresponds with the growth kinetics of most established cancer cell lines on conventional 2D culture systems [303, 304]. In contrast, TC-2 cells cultured in CA scaffolds showed a greatly reduced growth rate, better matching the *in vivo* growth of tumors [74]. It was speculated that PCa cells in 2D cultures were exposed to sufficient nutrients and oxygen whereas CA scaffolds had limited nutrient and oxygen transport and removal of cell wastes, which is similar to the *in vivo* milieu as tumors must recruit blood vessels before they can begin to proliferate rapidly. In fact, this agrees with previous studies that the 3D microenvironment provided by porous scaffolds promotes malignancy of tumor cells *in vitro* and *in vivo*, which contributes to the decreased cell proliferation and a better mimic tumor *in vivo* conditions than the rapidly proliferating cells in standard 2D culture [74, 305]. The current hurdle of PCa drug development lies in the lack of predictability of tumor behavior, which is due to the discordance between traditional cell culture and the *in vivo* microenvironment. The features of TC-2 cell growth in CA scaffolds better reflect the *in vivo* physiological situation in human cancer tissues than conventional 2D cultures.

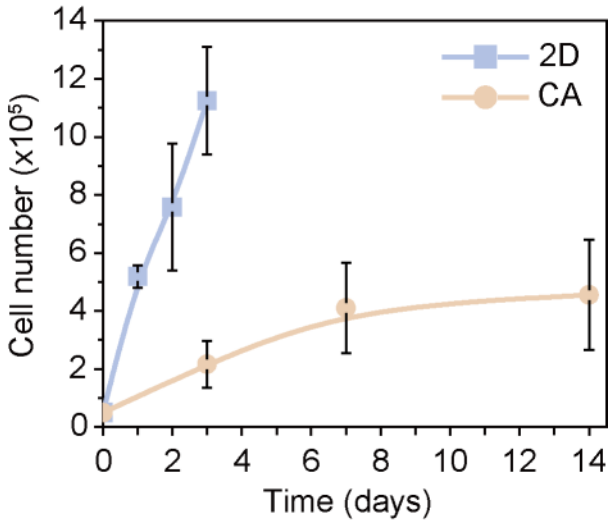

Figure 36. Growth kinetics of TC-2 cells in 2D cultures and in CA scaffolds as determined by the AB assay.

7.3.3 ECM and Cell-Matrix Interactions of PCa Cells in CA Scaffolds

In vitro 3D cultures may serve as a more representative model of the *in vivo* system than standard 2D cultures. In fact, the local tumor microenvironment is primarily composed of endogenous ECM.[306] Collagen and laminin are both important components of the ECM and have been used in producing 3D culture systems [307-310]. These two ECM related genes in cells cultured in 2D cultures and 3D scaffolds were quantified with qRT-PCR. A 20% (collagen) and 81% (laminin) increase in mRNA expression was observed in cells cultured in CA scaffolds relative to 2D cultures (**Figure 37a**). This suggests that in addition to resembling the architecture of solid tumors, the CA scaffolds also promoted the expression of ECM genes.

An epithelial-mesenchymal transition (EMT) is a developmental process of cells switching from epithelial to mesenchymal status [311]. Additionally, the EMT is activated by carcinoma cells during their course of invasion and metastasis [312]. Recent studies have demonstrated the role of the EMT in facilitating progression and metastasis of PCa as it increases motility and invasiveness of the cancer cells [313, 314]. We have previously shown that culture of brain and liver cancer cells on CA scaffolds increases their malignancy and chemo-resistance [10, 283], which was caused by transition to a more-stem like state through an EMT [10]. Therefore, to

better recapitulate the *in vivo* situation *in vitro*, 3D culture systems should be able to induce the EMT in PCa cells. We measured the expression levels of EMT related genes in PCa cells grown in CA scaffolds and 2D cultures.

Snail mediates the EMT through downregulation of cell adhesion molecules, and its expression increases with PCa progression [315, 316]. A 20% increase in Snail expression was demonstrated in CA scaffolds over 2D cultures as determined by qRT-PCR (**Figure 37b**), suggesting the CA culture system promoted the EMT of PCa cells.

Slug plays a critical role in the EMT and its upregulation is associated with advanced-stage PCa [317, 318], and Twist expression is positively correlated with Gleason grading of PCa, suggesting its role in tumorigenesis [319]. Twist is a highly conserved basic helix-loop-helix transcription factor in PCa that promotes the EMT [320]. The expression patterns of these two gene markers were similar to that of Snail, where the increased expression in CA scaffolds was approximately 34% and 90% higher than in 2D cultures (**Figure 37b**). Slug can also suppress the proliferation of PCa cells [321], which is in line with the decreased proliferation rate of TC-2 cells in CA scaffolds shown above (**Figure 36**).

Sip1, a member of the δEF-1 family of two-handed zinc finger nuclear factors, is another protein involved in the EMT of PCa [322]. Sip1 expression correlates with PCa cell migration and invasion [323, 324]. Sip1 mRNA expression in TC-2 cells cultured in CA scaffolds increased 2.2-fold as compared to those in 2D cultures (**Figure 37b**).

In addition to the upregulation of the mesenchymal markers, we also observed a 2.7-fold increase in mRNA expression of an epithelial marker E-cadherin (**Figure 37c**). High expression of E-cadherin is speculated to occur at the late stage of EMT, when the disseminated mesenchymal tumor cells recapitulate the pathology of their corresponding primary tumors at the metastatic sites [325]. In fact, E-cadherin upregulation can induce a more stem-like state in PCa cells [325-327]. Furthermore, upregulation of E-cadherin has been detected in advanced metastatic PCa, and is considered to be correlated with tumor invasion and poor patient prognosis [328, 329].

Overall, the upregulation of these EMT related transcriptional factors induced by culture in CA scaffolds shows the increased migratory potential and the ability of cells to invade an artificial scaffold, a typical phenotypic feature of PCa. Previous studies have demonstrated that the expression levels of these factors were induced by microenvironmental stimuli [330]. This

phenomenon observed in CA cultures suggests the potential of 3D CA scaffolds to act as a mimic of *in vivo* tumor microenvironment.

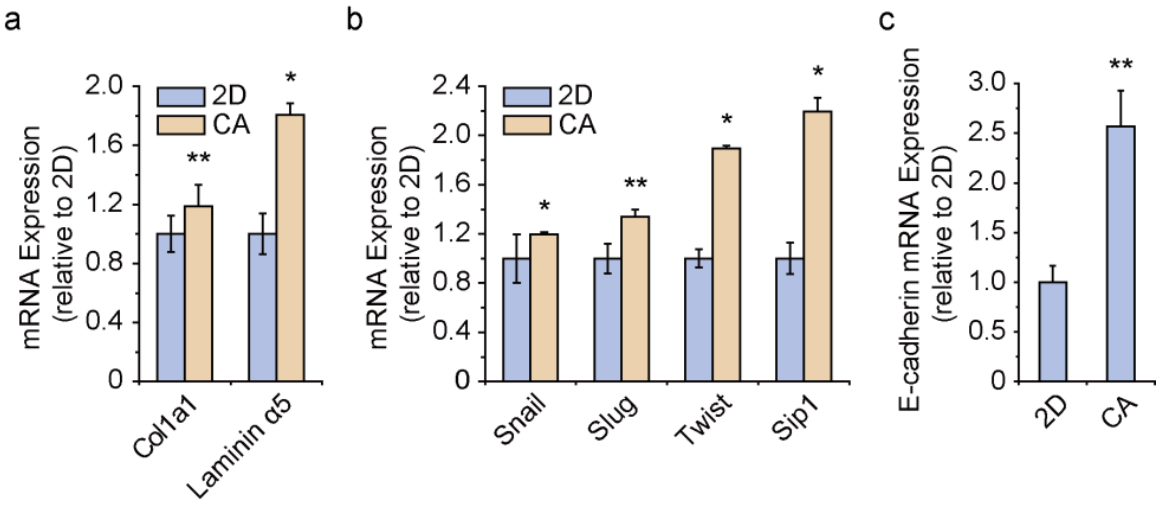

Figure 37. Expression of (a) ECM and (b and c) EMT gene markers quantified by qRT-PCR. Cells were grown in 2D cultures and CA scaffolds for 12 days prior to collection and analysis. Asterisks indicate significance as determined by Student's *t*-test: $*P < 0.01$ and $** P < 0.05$. Results are from 3 independent experiments run in triplicate.

7.3.4 Analyzing Plasmid Delivery in CA Scaffolds

Our previous studies demonstrated that CTX conjugated NPs are able to enhance delivery specifically to brain tumors by increasing the distribution and cell uptake of the NP throughout the tumor [6, 70]. It has also been reported that CTX is able to target PCa through specific interactions with cell surface receptors MMP-2 or Annexin A2 [104, 331]. To determine if CTX can target TC-2 PCa cells, the cells growing on 2D cultures were incubated with CTX-AF647 conjugate and free AF647 fluorophore at different concentrations for 1 hr and the binding of CTX-AF647 to PCa cells was assessed using flow cytometry. Here the free fluorophore served as the control to determine the background cellular uptake. Little binding of the free fluorophore to PCa cells was observed at the three fluorophore concentrations tested (**Figure 38a and b**). On the other hand, the binding of CTX-AF647 conjugates to PCa cells at the three concentrations of

CTX with the fluorophore amounts equivalent to the three free fluorophore concentrations was substantially higher than free AF647 and demonstrated strong dose-dependence. PCa cells treated with CTX-AF647 exhibited an approximate 3-, 4-, and 6-fold higher fluorescence intensity at the three fluorophore concentrations, respectively, compared to the untreated PCa cells, while free AF647 showed less than 1 fold increase in fluorescence intensity for all three concentrations of fluorophores as compared to the untreated cells (**Figure 38b**).

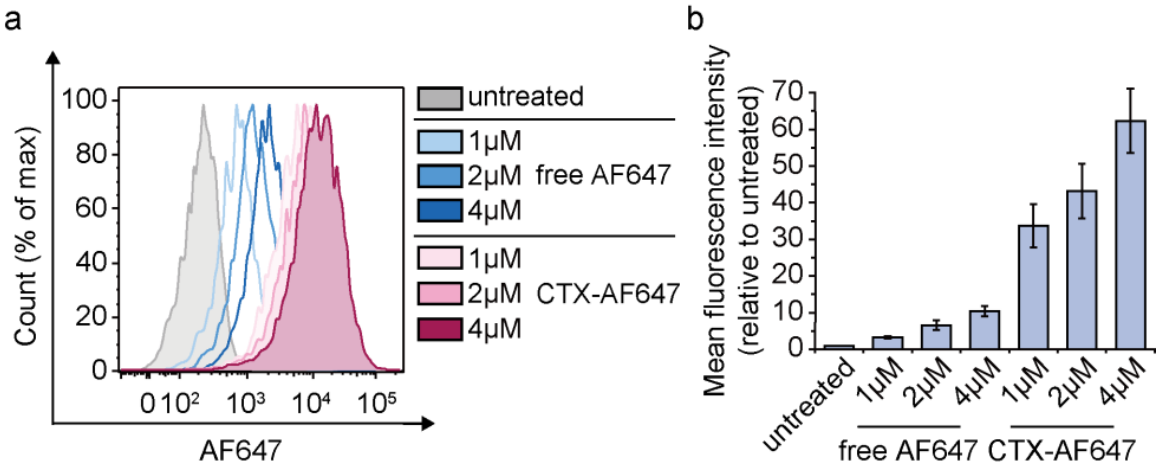

Figure 38. *In vitro* evaluation of tumor targeting of CTX to TC-2 cells. (a) Flow cytometry analysis of 2D cultured TC-2 cells incubated with free AF647 fluorophore and AF647 conjugated CTX (CTX-AF647) at different concentrations of CTX. (b) Normalized mean fluorescence intensity of TC-2 cells from (a).

To reveal the difference in mimicking the tumor microenvironment between 2D cultures and CA scaffolds for tumor targeted NPs as gene delivery carriers, PCa cells cultured in both 2D cultures and CA scaffolds were treated with RFP encoding plasmid DNA loaded NPs with (NP-CTX) or without CTX (NP-control) conjugated. The transfection efficiency was evaluated three days post-inoculation of NPs by measuring RFP fluorescence in solubilized cells using a microplate reader (**Figure 39a and b**). NP-CTX showed no cell targeting effect in 2D cultures whereas an 80% increase in RFP fluorescence intensity was observed in NP-CTX treated cells cultured in CA scaffolds as compared with NP-control treated cells. This is consistent with the fluorescence microscopy images that show more RFP expressing TC-2 cells in CA scaffolds

treated with NP-CTX than those treated with NP-control, while a similar percentage of RFP positive cells in 2D cultures was detected with both treatments (**Figure 39c**). Perls' Prussian blue staining also revealed that NP-CTX has higher affinity to TC-2 tumor spheres than NP-control, whereas cellular uptake is similar between NP-control and NP-CTX in 2D cultures (**Figure 39d**). In accord with our previous findings [6, 70], CTX promoted the distribution of NP inside the tumor, suggesting the high penetration capacity of NP-CTX in solid tumor.

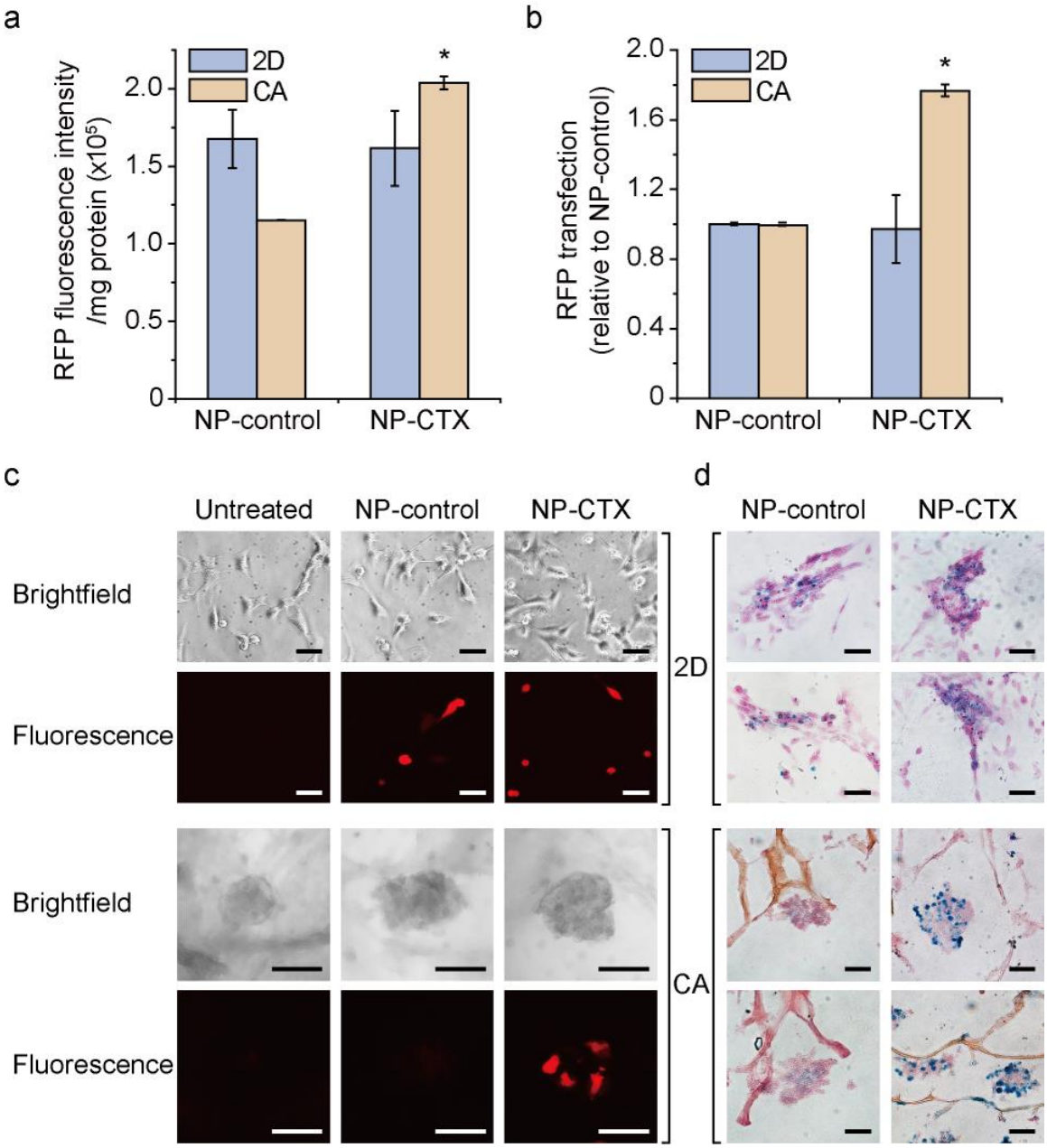

Figure 39. *In vitro* evaluation of targeted delivery of RFP plasmid to TC-2 cells in 2D cultures and CA scaffolds using NP-control and NP-CTX. (a) RFP transfection of TC-2 cells induced by NP-control and NP-CTX in 2D cultures and CA scaffolds. RFP fluorescence in TC-2 cells was measured using a microplate reader and normalized to total protein content. (b) RFP fluorescence intensity from NP-CTX and NP-control treated TC-2 cells growing in 2D and CA scaffolds acquired from (a) was normalized to the NP-control. Asterisk indicates significance as determined by Student's *t*-test: $*P < 0.01$. (c) Brightfield and fluorescence images of NP-control and NP-CTX transfected TC-2 cells growing in 2D cultures and CA scaffolds. Scale bars represent 100 μm. (d) NP-control and NP-CTX were also detected by staining with Perls' Prussian blue. TC-2 cells were counterstained with nuclear fast red. Scale bars correspond to 100 μm.

The lack of tumor cell targeting of NP-CTX in 2D cultures was likely due to the direct interaction between each cell and the positively charged NPs and to the absence of other materials in 2D cultures. The uptake of NP-CTX by each tumor cell was caused by both receptor–mediated (CTX and tumor cell surface receptors) and absorptive-mediated (positively charged NPs and negatively charged cells) endocytosis. Absorptive-mediated endocytosis dominates cellular uptake of NPs when NPs are highly positively charged, which has been observed with several other cationic gene delivery agents [7, 332]. When NPs were incubated with PCa tumor spheroids in CA scaffolds, positively charged NPs interact with cells as well as CA scaffolds. The tumor-targeted NP-CTX had high affinity to the PCa cells through specific interactions with cell surface receptors MMP-2 or Annexin A2 [104, 331] whereas non-targeted NP-control had similar affinity to the cell surface, CA scaffold, and ECMs produced by tumor cells through electrostatic interactions. Thus, the cellular uptake of NP-CTX in CA scaffolds was via both receptor- and adsorptive-mediated endocytosis while the cellular uptake of NP-control was via adsorptive-mediated endocytosis only. Additionally, the higher malignancy of PCa cells in 3D CA scaffolds as compared to 2D cultures likely caused increased expression of MMP-2 [333] so provided a higher number of cell surface receptors for NP-CTX to attach to. Thus, NP-CTX would have stronger affinity to PCa cells in tumor spheroids than PCa cells in 2D cultures [334-336].

7.3.5 In Vivo Delivery of RFP Using NP-CTX

Abnormal vasculature, elevated interstitial fluid pressure, and ECM are three unique architectural features of solid tumors that restrict mobility of a nanomedicine through malignant tissue [334, 335]. NPs can escape blood vessels by the enhanced permeation and retention (EPR) effect. Following extravasation from blood vessels, the transport of NP through the extracellular space to reach target cells is hindered by the complex structure of ECM in solid tumors comprising fibrous macromolecules such as collagen and GAGs [336]. Without a targeting ligand, positively charged NPs have a strong affinity to both ECM and target cells. Therefore, a targeting ligand is important for enabling the specific attachment of the NPs to the tumor cells. Our studies revealed that CTX enhanced NP-mediated transfection on cancer cells cultured in CA scaffolds.

We expected that the 3D model would serve as a good indicator of gene transfection efficiency *in vivo*. After establishing that the NP-CTX could enhance the delivery of plasmid DNA into cells in CA culture, we evaluated targeted gene delivery of NP-CTX in mice bearing TC-2 PCa tumors. NP-CTX and NP-control complexed with RFP plasmid were injected intravenously through the tail vein. After 48 hr, tumors were collected and imaged using the IVIS Lumina II system. 1.6-fold increase in fluorescence intensity was observed in the NP-CTX treated tumor as compared to cells treated with NP-control, demonstrating the increased transfection efficiency in the tumor as a result of targeting ability of CTX in PCa (**Figure 40a and b**). Perls' Prussian blue staining corroborated these results and showed accumulation of NP-CTX at a higher level than NP-control in tumor sections (**Figure 40c and d**). These results showed that NP-control and NP-CTX in PCa tumors behave similar to that in CA scaffolds *in vitro* (**Figure 39c and d**). Importantly, the increased transfection efficiency observed in the PCa tumor was target specific as RFP expression in liver, kidney, spleen, heart and lung was not affected by the presence of CTX (**Figure 41**).

Various strategies have been developed to facilitate efficient NP penetration into tumors. Size has been found to be a crucial factor that affects the permeability of nanodrugs [337, 338]. Additionally, targeting ligands have been shown to improve the delivery of NPs throughout the tumor [6, 339, 340]. The targeting capacity of CTX to human brain tumors is well established [6, 126]. Some evidence also indicates that CTX can target PCa *in vivo* [331]. When conjugated

onto NPs, CTX did not facilitate targeted gene delivery in PCa cells cultured on standard 2D TCPS surfaces. Instead, these *in vitro* results falsely predicted CTX is not a good targeting agent to use on the surface of cationic NPs to target PCa even though CTX itself showed high uptake in PCa cells. However, in agreement with the previous studies, our results demonstrate that CTX conjugated NPs had high binding efficiency in PCa tumors and were readily taken up and well distributed throughout PCa tumors while not affecting non-specific uptake in healthy tissues. Importantly, the *in vivo* targeting corresponded well to the *in vitro* NP-CTX delivery in CA scaffolds, revealing that NP-CTX mediated gene delivery in this *in vitro* cell culture model could replicate the *in vivo* targeting effect. It also indicated that this 3D cell culture model could be applied in the study of penetration and transport of anticancer nanomedicines in order to better predict their targeting efficiency *in vivo*.

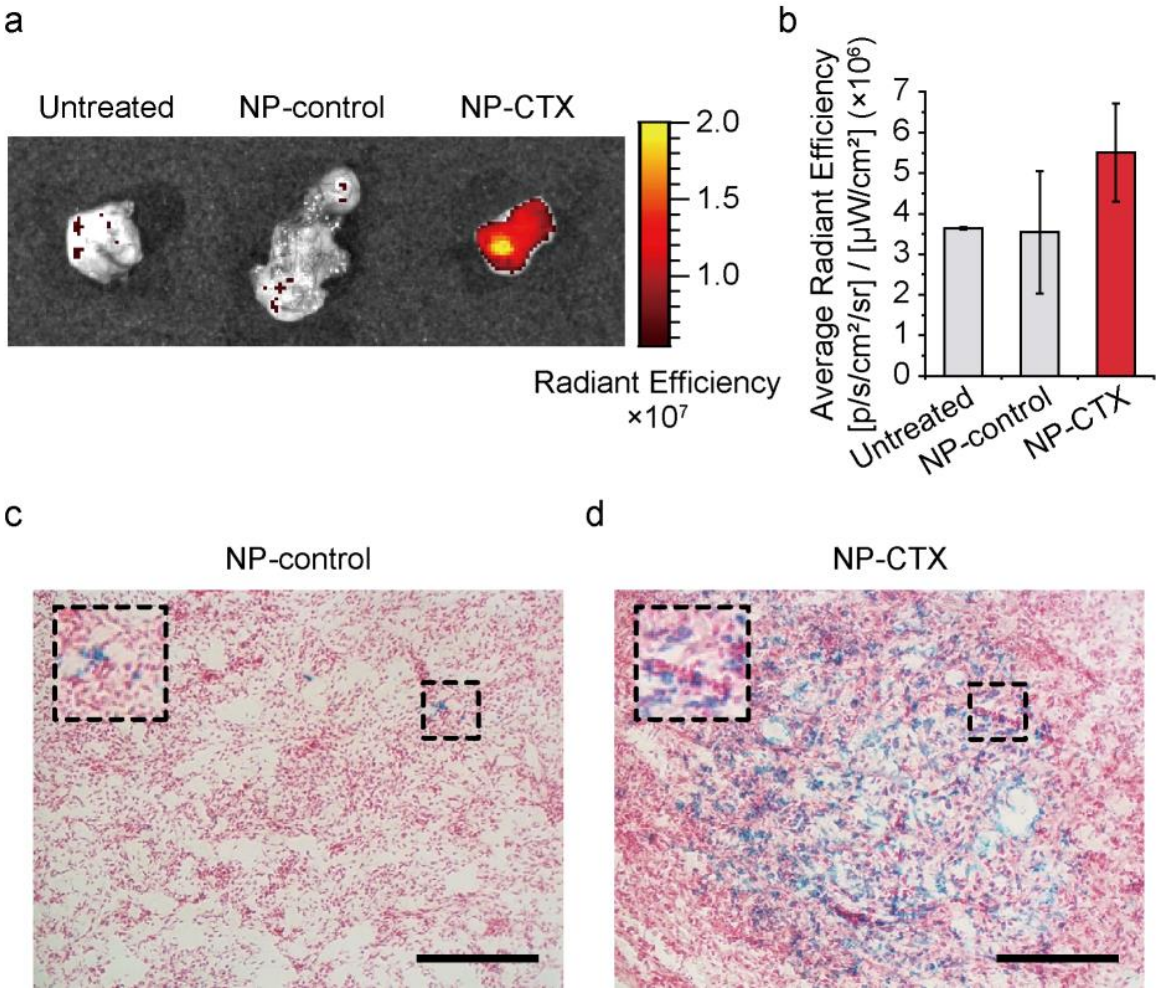

Figure 40. Accumulation and transfection efficiency of NP-control and NP-CTX in tumors. (a) Xenogen imaging of tumors from untreated, NP-control, and NP-CTX treated animals. (b) Quantification of fluorescence intensities (photons/sec/cm^2/steradian)/(μW/cm^2) of tumors from untreated mice and mice treated with NP-control and NP-CTX. (c-d) Perls' Prussian blue staining indicating the accumulation of NP. Scale bars represent 100 μm.

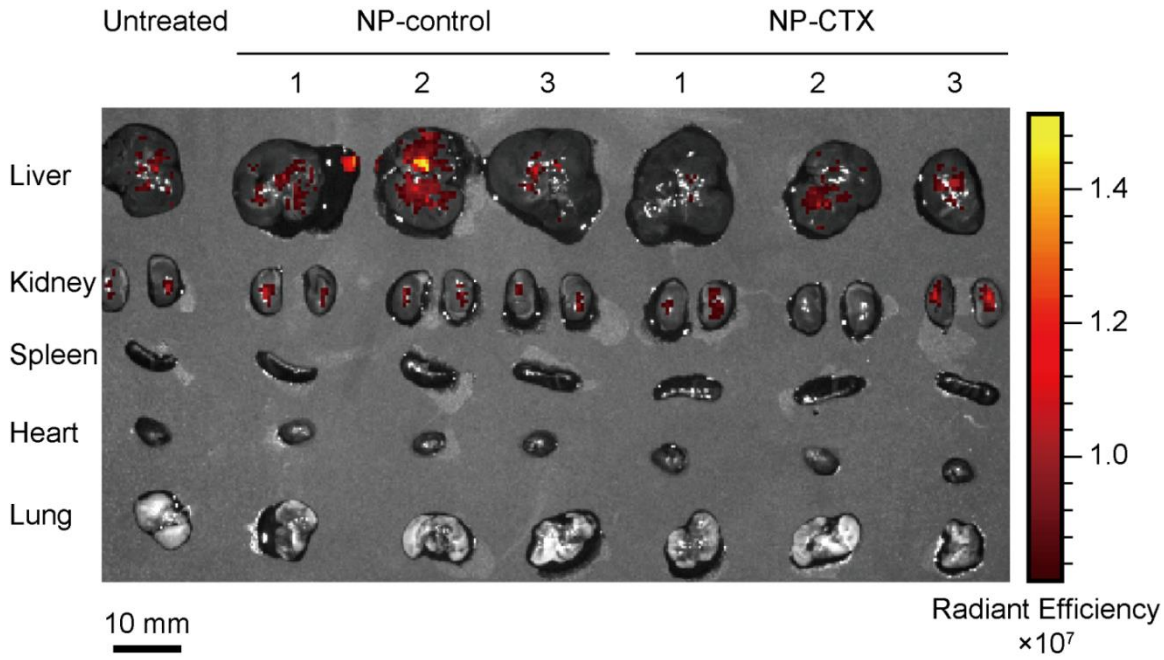

Figure 41. Xenogen images of harvested livers, kidneys, spleens, hearts, and lungsfrom untreated mice and mice treated with NP-control or NP-CTX (n = 3).

7.4 CONCLUSIONS

In the present study, we demonstrated that PCa TC-2 cells cultured in CA scaffolds *in vitro* more accurately predict *in vivo* targeted nanoparticle-mediated gene delivery. TC-2 PCa cells formed tumor spheroids when cultured in CA scaffolds and showed upregulation of ECM and EMT gene markers as compared to standard 2D culture on TCPS. Targeted nanoparticle-mediated delivery of RFP plasmid DNA into TC-2 tumor spheroids was achieved with CTX in cells cultured in CA scaffolds but not on 2D cultures in TCPS. This underscores the utility of the 3D culture when testing positively-charged targeted NPs as the standard 2D culture on TCPS did not show the targeting effect of CTX. Significantly, the *in vitro* targeted transfection results seen using CA scaffolds matched the *in vivo* targeted transfection efficiency observed in PCa tumors. Taken together, our results provide strong evidence that this *in vitro* cell culture system can serve as a

useful 3D tumor model that mimics the *in vivo* tumor microenvironment structure and accurately predicts *in vivo* targeting efficiency. Thus, this 3D scaffold culture system should be used in the initial screening of tumor targeted NP delivery vehicles.

8. SUMMARY OF MAJOR FINDINGS

Gene therapy possesses the potential to overcome many of the shortcomings of current cancer treatments, such as low therapeutic ratio and dose limiting toxicity [341]. The application of nanotechnology to cancer gene therapy has the potential to improve its efficacy while limiting off target toxicity. The aim of this dissertation was to design and develop multifunctional nanomaterials to improve nonviral gene delivery to cancer cells *in vitro* and *in vivo* as well as develop a better *in vitro* 3D scaffold that better mimics *in vivo* growth in order to evaluate nanoparticle-mediated gene delivery under more physiological conditions.

The development of an iron oxide nanoparticle system for non-viral gene delivery was presented in Chapter 3. It was demonstrated that nanoparticle coated with copolymer comprising biocompatible chitosan, PEG, and PEI with further modification of a targeting peptide called chlorotoxin was able to delivery plasmid DNA with limited toxicity. Targeted delivery of a suicide gene, TRAIL, can induce obvious toxicity *in vitro* and significantly inhibit tumor growth of a human GBM mouse xenograft model. We then applied this nanoparticle system in RNAi-mediated gene therapy in Chapter 4. By using a luciferase reporter system, we showed that the nanoparticle could deliver siRNA to tumor in a target-specific manner and efficiently suppress the target gene both *in vitro* and *in vivo*. In order to expand the work, we identified two therapeutic siRNA-based treatments *in vitro* in Chapter 5. The knock-down of both EGFR and β-catenin expression inhibited GBM cell proliferation, migration, and invasion while increasing apoptosis. The delivery of siRNA against MGMT significantly sensitized GBM cells *in vitro* to the clinical methylating agent temozolomide by about 5-fold. Thus, we also evaluated treatment with anti-MGMT siRNA *in vivo* in Chapter 6. We found that nanoparticle-mediated delivery of MGMT siRNA successfully inhibited MGMT expression in an intracranial human GBM mouse xenograft, delayed the tumor growth, and prolonged animal survival.

Finally, the growth of human tumor cells cultured on three-dimensional (3D) scaffolds fabricated with chitosan and alginate better mimicked that of tumors *in vivo* was reported in Chapter 7. Tumor cells cultured on 3D scaffolds demonstrated higher expression of genes associated with tumor malignancy and treatment resistance compared to cells cultured as adherent monolayers. Nanoparticle-mediated gene delivery was demonstrated in cells grown on

scaffolds, suggesting that the scaffolds could be used for inexpensive, high-throughput screening of nanomedicines prior to *in vivo* evaluation in costly animal models.

9. **REFERENCES**

[1] Siegel RL, Miller KD, Jemal A. Cancer statistics, 2015. CA Cancer J Clin. 2015;65:5-29.

[2] Holohan C, Van Schaeybroeck S, Longley DB, Johnston PG. Cancer drug resistance: an evolving paradigm. Nat Rev Cancer. 2013;13:714-26.

[3] Davis ME, Chen Z, Shin DM. Nanoparticle therapeutics: an emerging treatment modality for cancer. Nat Rev Drug Discov. 2008;7:771-82.

[4] Wang AZ, Langer R, Farokhzad OC. Nanoparticle delivery of cancer drugs. Annu Rev Med. 2012;63:185-98.

[5] Pampaloni F, Reynaud EG, Stelzer EHK. The third dimension bridges the gap between cell culture and live tissue. Nat Rev Mol Cell Biol. 2007;8:839-45.

[6] Kievit FM, Veiseh O, Fang C, Bhattarai N, Lee D, Ellenbogen RG, et al. Chlorotoxin labeled magnetic nanovectors for targeted gene delivery to glioma. ACS Nano. 2010;4:4587-94.

[7] Lungwitz U, Breunig M, Blunk T, Göpferich A. Polyethylenimine-based non-viral gene delivery systems. Eur J Pharm Biopharm. 2005;60:247-66.

[8] Veiseh O, Sun C, Fang C, Bhattarai N, Gunn J, Kievit F, et al. Specific targeting of brain tumors with an optical/magnetic resonance imaging nanoprobe across the blood-brain barrier. Cancer Res. 2009;69:6200-7.

[9] Florczyk SJ, Liu G, Kievit FM, Lewis AM, Wu JD, Zhang M. 3D porous chitosan-alginate scaffolds: a new matrix for studying prostate cancer cell-lymphocyte interactions in vitro. Adv Healthcare Mater. 2012;1:590-9.

[10] Kievit FM, Florczyk SJ, Leung MC, Veiseh O, Park JO, Disis ML, et al. Chitosan-alginate 3D scaffolds as a mimic of the glioma tumor microenvironment. Biomaterials. 2010;31:5903-10.

[11] Friedmann T. A brief history of gene therapy. Nat Genet. 1992;2:93-8.

[12] Hollon T. Researchers and regulators reflect on first gene therapy death. Nat Med. 2000;6:6.

[13] Edwards BK, Noone A-M, Mariotto AB, Simard EP, Boscoe FP, Henley SJ, et al. Annual Report to the Nation on the status of cancer, 1975-2010, featuring prevalence of comorbidity and impact on survival among persons with lung, colorectal, breast, or prostate cancer. Cancer. 2014;120:1290-314.

[14] Chabner BA, Roberts TG. Chemotherapy and the war on cancer. Nat Rev Cancer. 2005;5:65-72.

[15] Stubbe CE, Valero M. Complementary strategies for the management of radiation therapy side effects. J Adv Pract Oncol. 2013;4:219-31.

[16] Ginn SL, Alexander IE, Edelstein ML, Abedi MR, Wixon J. Gene therapy clinical trials worldwide to 2012-an update. J Gene Med. 2013;15:65-77.

[17] Heise C, Sampson-Johannes A, Williams A, McCormick F, Von Hoff DD, Kirn DH. ONYX-015, an E1B gene-attenuated adenovirus, causes tumor-specific cytolysis and antitumoral efficacy that can be augmented by standard chemotherapeutic agents. Nat Med. 1997;3:639-45.

[18] Haupt RM, Sings HL. The efficacy and safety of the quadrivalent human papillomavirus 6/11/16/18 vaccine gardasil. J Adolesc Health. 2011;49:467-75.

[19] Kantoff PW, Higano CS, Shore ND, Berger ER, Small EJ, Penson DF, et al. Sipuleucel-T immunotherapy for castration-resistant prostate cancer. N Engl J Med. 2010;363:411-22.

[20] Bumcrot D, Manoharan M, Koteliansky V, Sah DWY. RNAi therapeutics: a potential new class of pharmaceutical drugs. Nat Chem Biol. 2006;2:711-9.

[21] Davis ME, Zuckerman JE, Choi CHJ, Seligson D, Tolcher A, Alabi CA, et al. Evidence of RNAi in humans from systemically administered siRNA via targeted nanoparticles. Nature. 2010;464:1067-70.

[22] Kouraklis G. Review: gene therapy for cancer. Dig Dis Sci. 2000;45:1045-52.

[23] Flintoft L. Gene therapy: gene editors deliver. Nat Rev Genet. 2007;8:908-9.

[24] Daka A, Peer D. RNAi-based nanomedicines for targeted personalized therapy. Adv Drug Deliv Rev. 2012;64:1508-21.

[25] Burnett JC, Rossi JJ, Tiemann K. Current progress of siRNA/shRNA therapeutics in clinical trials. Biotechnol J. 2011;6:1130-46.

[26] Burnett John C, Rossi John J. RNA-based therapeutics: current progress and future prospects. Chem Biol. 2012;19:60-71.

[27] Cowen RL, Williams JC, Emery S, Blakey D, Darling JL, Lowenstein PR, et al. Adenovirus vector-mediated delivery of the prodrug-converting enzyme carboxypeptidase G2 in a secreted or GPI-anchored form: high-level expression of this active conditional cytotoxic enzyme at the plasma membrane. Cancer Gene Ther. 2002;9:897-907.

[28] Adams JM, Cory S. The Bcl-2 protein family: arbiters of cell survival. Science. 1998;281:1322-6.

[29] King GD, Curtin JF, Candolfi M, Kroeger K, Lowenstein PR, Castro MG. Gene therapy and targeted toxins for glioma. Curr Gene Ther. 2005;5:535-57.

[30] Wei S-J, Chao Y, Hung Y-M, Lin W-c, Yang D-M, Shih Y-L, et al. S- and G2-phase cell cycle arrests and apoptosis induced by ganciclovir in murine melanoma cells transduced with herpes simplex virus thymidine kinase. Exp Cell Res. 1998;241:66-75.

[31] Beltinger C, Fulda S, Kammertoens T, Meyer E, Uckert W, Debatin K-M. Herpes simplex virus thymidine kinase/ganciclovir-induced apoptosis involves ligand-independent death receptor aggregation and activation of caspases. Proc Natl Acad Sci U S A. 1999;96:8699-704.

[32] Tang W, He Y, Zhou S, Ma Y, Liu G. A novel bifidobacterium infantis -mediated TK/GCV suicide gene therapy system exhibits antitumor activity in a rat model of bladder cancer. J Exp Clin Cancer Res. 2009;28:1-7.

[33] Kakinoki K, Nakamoto Y, Kagaya T, Tsuchiyama T, Sakai Y, Nakahama T, et al. Prevention of intrahepatic metastasis of liver cancer by suicide gene therapy and chemokine ligand 2/monocyte chemoattractant protein-1 delivery in mice. J Gene Med. 2010;12:1002-13.

[34] Chen LS, Wang M, Ou WC, Fung CY, Chen PL, Chang CF, et al. Efficient gene transfer using the human JC virus-like particle that inhibits human colon adenocarcinoma growth in a nude mouse model. Gene Ther. 2010;17:1033-41.

[35] Greish K, Frandsen J, Scharff S, Gustafson J, Cappello J, Li D, et al. Silk-elastinlike protein polymers improve the efficacy of adenovirus thymidine kinase enzyme prodrug therapy of head and neck tumors. J Gene Med. 2010;12:572-9.

[36] Mullen CA, Coale MM, Lowe R, Blaese RM. Tumors expressing the cytosine deaminase suicide gene can be eliminated in vivo with 5-fluorocytosine and induce protective immunity to wild type tumor. Cancer Res. 1994;54:1503-6.

[37] Bentires-Alj M, Hellin AC, Lechanteur C, Princen F, Lopez M, Fillet G, et al. Cytosine deaminase suicide gene therapy for peritoneal carcinomatosis. Cancer Gene Ther. 2000;7:20-6.

[38] Ichikawa T, Tamiya T, Adachi Y, Ono Y, Matsumoto K, Furuta T, et al. In vivo efficacy and toxicity of 5-fluorocytosine/cytosine deaminase gene therapy for malignant gliomas mediated by adenovirus. Cancer Gene Ther. 2000;7:74-82.

[39] Topf N, Worgall S, Hackett NR, Crystal RG. Regional 'pro-drug' gene therapy: intravenous administration of an adenoviral vector expressing the E. coli cytosine deaminase gene and

systemic administration of 5-fluorocytosine suppresses growth of hepatic metastasis of colon carcinoma. Gene Ther. 1998;5:507-13.

[40] Li X, Marani M, Yu J, Nan B, Roth JA, Kagawa S, et al. Adenovirus-mediated bax overexpression for the induction of therapeutic apoptosis in prostate cancer. Cancer Res. 2001;61:186-91.

[41] Kobayashi T, Sawa H, Morikawa J, Zhang W, Shiku H. Bax induction activates apoptotic cascade via mitochondrial cytochrome c release and Bax overexpression enhances apoptosis induced by chemotherapeutic agents in DLD-1 colon cancer cells. Jpn J Cancer Res. 2000;91:1264-8.

[42] Skirnisdóttir I, Sorbe B, Seidal T. P53, bcl-2, and bax: their relationship and effect on prognosis in early stage epithelial ovarian carcinoma. Int J Gynecol Cancer. 2001;11:147-58.

[43] Huh WK, Gomez-Navarro J, Arafat WO, Xiang J, Mahasreshti PJ, Alvarez RD, et al. Bax-induced apoptosis as a novel gene therapy approach for carcinoma of the cervix. Gynecol Oncol. 2001;83:370-7.

[44] Lowe SL, Rubinchik S, Honda T, McDonnell TJ, Dong JY, Norris JS. Prostate-specific expression of Bax delivered by an adenoviral vector induces apoptosis in LNCaP prostate cancer cells. Gene Ther. 2001;8:1363-71.

[45] Johnstone RW, Frew AJ, Smyth MJ. The TRAIL apoptotic pathway in cancer onset, progression and therapy. Nat Rev Cancer. 2008;8:782-98.

[46] Ashkenazi A. Targeting death and decoy receptors of the tumour-necrosis factor superfamily. Nat Rev Cancer. 2002;2:420-30.

[47] Ashkenazi A, Dixit VM. Apoptosis control by death and decoy receptors. Curr Opin Cell Biol. 1999;11:255-60.

[48] Sasportas LS, Kasmieh R, Wakimoto H, Hingtgen S, van de Water JAJM, Mohapatra G, et al. Assessment of therapeutic efficacy and fate of engineered human mesenchymal stem cells for cancer therapy. Proc Natl Acad Sci U S A. 2009;106:4822-7.

[49] Dorsey JF, Mintz A, Tian X, Dowling ML, Plastaras JP, Dicker DT, et al. Tumor necrosis factor–related apoptosis-inducing ligand (TRAIL) and paclitaxel have cooperative in vivo effects against glioblastoma multiforme cells. Mol Cancer Ther. 2009;8:3285-95.

[50] Bader AG, Brown D, Stoudemire J, Lammers P. Developing therapeutic microRNAs for cancer. Gene Ther. 2011;18:1121-6.

[51] Price C, Chen J. MicroRNAs in cancer biology and therapy: current status and perspectives. Genes Dis. 2014;1:53-63.

[52] Naidu S, Magee P, Garofalo M. MiRNA-based therapeutic intervention of cancer. J Hematol Oncol. 2015;8:68.

[53] Varela-Rohena A, Carpenito C, Perez EE, Richardson M, Parry RV, Milone M, et al. Genetic engineering of T cells for adoptive immunotherapy. Immunol Res. 2008;42:166-81.

[54] Stauss HJ, Morris EC. Immunotherapy with gene-modified T cells: limiting side effects provides new challenges. Gene Ther. 2013;20:1029-32.

[55] Johnson LA, Morgan RA, Dudley ME, Cassard L, Yang JC, Hughes MS, et al. Gene therapy with human and mouse T-cell receptors mediates cancer regression and targets normal tissues expressing cognate antigen. Blood. 2009;114:535-46.

[56] Rapoport AP, Stadtmauer EA, Binder-Scholl GK, Goloubeva O, Vogl DT, Lacey SF, et al. NY-ESO-1-specific TCR-engineered T cells mediate sustained antigen-specific antitumor effects in myeloma. Nat Med. 2015;21:914-21.

[57] Waehler R, Russell SJ, Curiel DT. Engineering targeted viral vectors for gene therapy. Nat Rev Genet. 2007;8:573-87.

[58] Wei MQ, Mengesha A, Good D, Ann é J. Bacterial targeted tumour therapy-dawn of a new era. Cancer Lett. 2008;259:16-27.

[59] Baban CK, Cronin M, O'Hanlon D, O'Sullivan GC, Tangney M. Bacteria as vectors for gene therapy of cancer. Bioeng Bugs. 2010;1:385-94.

[60] Chan JKY, Lam PYP. Human mesenchymal stem cells and their paracrine factors for the treatment of brain tumors. Cancer Gene Ther. 2013;20:539-43.

[61] Wang C, Natsume A, Lee HJ, Motomura K, Nishimira Y, Ohno M, et al. Neural stem cell-based dual suicide gene delivery for metastatic brain tumors. Cancer Gene Ther. 2012;19:796-801.

[62] Immordino ML, Dosio F, Cattel L. Stealth liposomes: review of the basic science, rationale, and clinical applications, existing and potential. Int J Nanomed. 2006;1:297-315.

[63] Barenholz Y. Doxil®-The first FDA-approved nano-drug: lessons learned. J Controlled Release. 2012;160:117-34.

[64] Liechty WB, Kryscio DR, Slaughter BV, Peppas NA. Polymers for drug delivery systems. Annu Rev Chem Biomol Eng. 2010;1:149-73.

[65] Jain S, Hirst DG, O'Sullivan JM. Gold nanoparticles as novel agents for cancer therapy. Br J Radiol. 2012;85:101-13.

[66] Gupta AK, Gupta M. Synthesis and surface engineering of iron oxide nanoparticles for biomedical applications. Biomaterials. 2005;26:3995-4021.

[67] Hodges BL, Serra D, Hu H, Begy CA, Chamberlain JS, Amalfitano A. Multiply deleted [E1, polymerase-, and pTP-] adenovirus vector persists despite deletion of the preterminal protein. J Gene Med. 2000;2:250-9.

[68] Kay MA, Holterman A-X, Meuse L, Gown A, Ochs HD, Linsley PS, et al. Long-term hepatic adenovirus-mediated gene expression in mice following CTLA4Ig administration. Nat Genet. 1995;11:191-7.

[69] Pecot CV, Calin GA, Coleman RL, Lopez-Berestein G, Sood AK. RNA interference in the clinic: challenges and future directions. Nat Rev Cancer. 2011;11:59-67.

[70] Veiseh O, Kievit FM, Fang C, Mu N, Jana S, Leung MC, et al. Chlorotoxin bound magnetic nanovector tailored for cancer cell targeting, imaging, and siRNA delivery. Biomaterials. 2010;31:8032-42.

[71] Kievit FM, Zhang M. Surface engineering of iron oxide nanoparticles for targeted cancer therapy. Accounts of chemical research. 2011;44:853-62.

[72] Zhang J, Yang PL, Gray NS. Targeting cancer with small molecule kinase inhibitors. Nat Rev Cancer. 2009;9:28-39.

[73] Yamada KM, Cukierman E. Modeling tissue morphogenesis and cancer in 3D. Cell. 2007;130:601-10.

[74] Fischbach C, Chen R, Matsumoto T, Schmelzle T, Brugge JS, Polverini PJ, et al. Engineering tumors with 3D scaffolds. Nat Methods. 2007;4:855-60.

[75] Malafaya PB, Silva GA, Reis RL. Natural–origin polymers as carriers and scaffolds for biomolecules and cell delivery in tissue engineering applications. Adv Drug Deliv Rev. 2007;59:207-33.

[76] Goodman TT, Ng CP, Pun SH. 3-D tissue culture systems for the evaluation and optimization of nanoparticle-based drug carriers. Bioconjugate Chem. 2008;19:1951-9.

[77] Gilbertson Richard J. Driving glioblastoma to drink. Cell. 2014;157:289-90.

[78] Stupp R, Mason WP, van den Bent MJ, Weller M, Fisher B, Taphoorn MJB, et al. Radiotherapy plus concomitant and adjuvant temozolomide for glioblastoma. N Engl J Med. 2005;352:987-96.

[79] Huse JT, Holland EC. Targeting brain cancer: advances in the molecular pathology of malignant glioma and medulloblastoma. Nat Rev Cancer. 2010;10:319-31.

[80] Holland EC. Glioblastoma multiforme: the terminator. Proc Natl Acad Sci U S A. 2000;97:6242-4.

[81] Flintoft L. Gene therapy: gene editors deliver. Nat Rev Genet. 2007;8:908-9.

[82] Kwiatkowska A, Nandhu M, Behera P, Chiocca E, Viapiano M. Strategies in gene therapy for glioblastoma. Cancers. 2013;5:1271-305.

[83] Sheridan C. Gene therapy finds its niche. Nat Biotech. 2011;29:121-8.

[84] Rieger J, Naumann U, Glaser T, Ashkenazi A, Weller M. APO2 ligand: a novel lethal weapon against malignant glioma? FEBS Letters. 1998;427:124-8.

[85] Herbst RS, Eckhardt SG, Kurzrock R, Ebbinghaus S, O'Dwyer PJ, Gordon MS, et al. Phase I dose-escalation study of recombinant human Apo2L/TRAIL, a dual proapoptotic receptor agonist, in patients with advanced cancer. J Clin Oncol. 2010;28:2839-46.

[86] Ashkenazi A, Pai RC, Fong S, Leung S, Lawrence DA, Marsters SA, et al. Safety and antitumor activity of recombinant soluble Apo2 ligand. J Clin Invest. 1999;104:155-62.

[87] Walczak H, Miller RE, Ariail K, Gliniak B, Griffith TS, Kubin M, et al. Tumoricidal activity of tumor necrosis factor-related apoptosis-inducing ligand in vivo. Nat Med. 1999;5:157-63.

[88] Pan Y, Xu R, Peach M, Huang C, Branstetter D, Durbin B, et al. Application of pharmacodynamic assays in a phase Ia trial of Apo2L/TRAIL in patients with advanced tumors. Journal of Clinical Oncology. 2007;25:3535.

[89] Camidge D, Herbst RS, Gordon M, Eckhardt S, Kurzroc R, Durbin B, et al. A phase I safety and pharmacokinetic study of apomab, a human DR5 agonist antibody, in patients with advanced cancer. J Clin Oncol. 2007;25:3582.

[90] Herbst RS, Mendolson DS, Ebbinghaus S, Gordon MS, O'Dwyer P, Lieberman G, et al. A phase I safety and pharmacokinetic (PK) study of recombinant Apo2L/TRAIL, an apoptosis-inducing protein in patients with advanced cancer. J Clin Oncol. 2006;24:3013.

[91] Yamanaka T, Shiraki K, Sugimoto K, Ito T, Fujikawa K, Ito M, et al. Chemotherapeutic agents augment TRAIL-induced apoptosis in human hepatocellular carcinoma cell lines. Hepatology. 2000;32:482-90.

[92] Perlstein B, Finniss SA, Miller C, Okhrimenko H, Kazimirsky G, Cazacu S, et al. TRAIL conjugated to nanoparticles exhibits increased anti-tumor activities in glioma cells and glioma stem cells in vitro and in vivo. Neuro Oncol. 2013;15:29-40.

[93] Kim H, Jeong D, Kang HE, Lee KC, Na K. A sulfate polysaccharide/TNF-related apoptosis-inducing ligand (TRAIL) complex for the long-term delivery of TRAIL in poly (lactic-co-glycolic acid) (PLGA) microspheres. J Pharm Pharmacol. 2013;65:11-21.

[94] Kim TH, Jo YG, Jiang HH, Lim SM, Youn YS, Lee S, et al. PEG-transferrin conjugated TRAIL (TNF-related apoptosis-inducing ligand) for therapeutic tumor targeting. J Controlled Release. 2012;162:422-8.

[95] Jaganathan J, Petit JH, Lazio BE, Singh SK, Chin LS. Tumor necrosis factor-related apoptosis-inducing ligand-mediated apoptosis in established and primary glioma cell lines. Neurosurgical focus. 2002;13:ecp1.

[96] Wohlfahrt ME, Beard BC, Lieber A, Kiem HP. A capsid-modified, conditionally replicating oncolytic adenovirus vector expressing TRAIL leads to enhanced cancer cell killing in human glioblastoma models. Cancer Res. 2007;67:8783-90.

[97] Jiang M, Liu Z, Xiang Y, Ma H, Liu S, Liu Y, et al. Synergistic antitumor effect of AAV-mediated TRAIL expression combined with cisplatin on head and neck squamous cell carcinoma. BMC Cancer. 2011;11:54-.

[98] Hu Y-L, Huang B, Zhang T-Y, Miao P-H, Tang G-P, Tabata Y, et al. Mesenchymal stem cells as a novel carrier for targeted delivery of gene in cancer therapy based on nonviral transfection. Mol Pharmaceutics. 2012;9:2698-709.

[99] Wong HL, Wu XY, Bendayan R. Nanotechnological advances for the delivery of CNS therapeutics. Adv Drug Deliv Rev. 2012;64:686-700.

[100] Sun CR, Du K, Fang C, Bhattarai N, Veiseh O, Kievit F, et al. PEG-mediated synthesis of highly dispersive multifunctional superparamagnetic nanoparticles: their physicochemical properties and function in vivo. ACS Nano. 2010;4:2402-10.

[101] Weissleder R, Stark DD, Engelstad BL, Bacon BR, Compton CC, White DL, et al. Superparamagnetic iron oxide: pharmacokinetics and toxicity. AJR, Am J Roentgenol. 1989;152:167-73.

[102] Kievit FM, Veiseh O, Bhattarai N, Fang C, Gunn JW, Lee D, et al. PEI-PEG-chitosan-copolymer-coated iron oxide nanoparticles for safe gene delivery: synthesis, complexation, and transfection. Adv Funct Mater. 2009;19:2244-51.

[103] Veiseh O, Gunn JW, Kievit FM, Sun C, Fang C, Lee JSH, et al. Inhibition of tumor-cell invasion with chlorotoxin-bound superparamagnetic nanoparticles. Small. 2009;5:256-64.

[104] Kesavan K, Ratliff J, Johnson EW, Dahlberg W, Asara JM, Misra P, et al. Annexin A2 is a molecular target for TM601, a peptide with tumor-targeting and anti-angiogenic effects. J Biol Chem. 2010;285:4366-74.

[105] Stephen ZR, Kievit FM, Veiseh O, Chiarelli PA, Fang C, Wang K, et al. Redox-responsive magnetic nanoparticle for targeted convection-enhanced delivery of O6-benzylguanine to brain tumors. ACS Nano. 2014;8:10383-95.

[106] Kagawa S, He C, Gu J, Koch P, Rha S-J, Roth JA, et al. Antitumor activity and bystander effects of the tumor necrosis factor-related apoptosis-inducing ligand (TRAIL) gene. Cancer Res. 2001;61:3330-8.

[107] Bhattarai N, Ramay HR, Gunn J, Matsen FA, Zhang M. PEG-grafted chitosan as an injectable thermosensitive hydrogel for sustained protein release. Journal of Controlled Release. 2005;103:609-24.

[108] Fang C, Bhattarai N, Sun C, Zhang M. Functionalized nanoparticles with long-term stability in biological media. Small. 2009;5:1637-41.

[109] Longmire M, Choyke PL, Kobayashi H. Clearance properties of nano-sized particles and molecules as imaging agents: considerations and caveats. Nanomedicine. 2008;3:703-17.

[110] Ruoslahti E, Bhatia SN, Sailor MJ. Targeting of drugs and nanoparticles to tumors. J Cell Biol. 2010;188:759-68.

[111] Doane TL, Chuang CH, Hill RJ, Burda C. Nanoparticle zeta-potentials. Acc Chem Res. 2012;45:317-26.

[112] Ehtesham M, Kabos P, Gutierrez MAR, Chung NHC, Griffith TS, Black KL, et al. Induction of glioblastoma apoptosis using neural stem cell-mediated delivery of tumor necrosis factor-related apoptosis-inducing ligand. Cancer Res. 2002;62:7170-4.

[113] Zhang Y, Ma CH, Liu H, Zhang XM, Sun WS. pVAX1 plasmid vector-mediated gene transfer of soluble TRAIL suppresses human hepatocellular carcinoma growth in nude mice. Acta biochimica Polonica. 2007;54:307-13.

[114] Lemke J, von Karstedt S, Zinngrebe J, Walczak H. Getting TRAIL back on track for cancer therapy. Cell Death Differ. 2014;21:1350-64.

[115] Song JH, Song DK, Pyrzynska B, Petruk KC, Van Meir EG, Hao C. TRAIL triggers apoptosis in human malignant glioma cells through extrinsic and intrinsic pathways. Brain Pathol. 2003;13:539-53.

[116] Villalonga-Planells R, Coll-Mulet L, Martínez-Soler F, Castaño E, Acebes J-J, Giménez-Bonafé P, et al. Activation of p53 by nutlin-3a induces apoptosis and cellular senescence in human glioblastoma multiforme. PLoS ONE. 2011;6:e18588.

[117] Ehrhardt H, Wachter F, Grunert M, Jeremias I. Cell cycle-arrested tumor cells exhibit increased sensitivity towards TRAIL-induced apoptosis. Cell Death Dis. 2013;4:e661.

[118] Kim M, Liao J, Dowling ML, Voong KR, Parker SE, Wang S, et al. TRAIL inactivates the mitotic checkpoint and potentiates death induced by microtubule-targeting agents in human cancer cells. Cancer Res. 2008;68:3440-9.

[119] Dou Y, Wang Y, Xu J, Li Z, Sun P, Meng Q. Experiment research on inhibition of glioma with sTRAIL in vitro. Artif Cells Nanomed Biotechnol. 2014;42:186-91.

[120] Vilimanovich U, Bumbasirevic V. TRAIL induces proliferation of human glioma cells by c-FLIPL-mediated activation of ERK1/2. Cell Mol Life Sci. 2008;65:814-26.

[121] Tsamis KI, Alexiou GA, Vartholomatos E, Kyritsis AP. Combination treatment for glioblastoma cells with tumor necrosis factor-related apoptosis-inducing ligand and oncolytic adenovirus delta-24. Cancer Invest. 2013;31:630-8.

[122] Kastan MB, Onyekwere O, Sidransky D, Vogelstein B, Craig RW. Participation of p53 protein in the cellular response to DNA damage. Cancer Res. 1991;51:6304-11.

[123] Taylor WR, Stark GR. Regulation of the G2/M transition by p53. Oncogene. 2001;20:1803-15.

[124] Choi CHJ, Alabi CA, Webster P, Davis ME. Mechanism of active targeting in solid tumors with transferrin-containing gold nanoparticles. Proc Natl Acad Sci U S A. 2010;107:1235-40.

[125] Kirpotin DB, Drummond DC, Shao Y, Shalaby MR, Hong K, Nielsen UB, et al. Antibody targeting of long-circulating lipidic nanoparticles does not increase tumor localization but does increase internalization in animal models. Cancer Res. 2006;66:6732-40.

[126] Veiseh O, Sun C, Gunn J, Kohler N, Gabikian P, Lee D, et al. Optical and MRI multifunctional nanoprobe for targeting gliomas. Nano Lett. 2005;5:1003-8.

[127] Safdar S, Taite LJ. Targeted diazeniumdiolates: localized nitric oxide release from glioma-specific peptides and proteins. Int J Pharm. 2012;422:264-70.

[128] Safdar S, Payne CA, Tu NH, Taite LJ. Targeted nitric oxide delivery preferentially induces glioma cell chemosensitivity via altered p53 and O6-methylguanine-DNA methyltransferase activity. Biotechnol Bioeng. 2013;110:1211-20.

[129] Shen S, Khazaeli MB, Gillespie GY, Alvarez V. Radiation dosimetry of 131I-chlorotoxin for targeted radiotherapy in glioma-bearing mice. J Neurooncol. 2005;71:113-9.

[130] Zhai H, Acharya S, Gravanis I, Mehmood S, Seidman RJ, Shroyer KR, et al. Annexin A2 promotes glioma cell invasion and tumor progression. J Neurosci. 2011;31:14346-60.

[131] Walczak H, Miller RE, Ariail K, Gliniak B, Griffith TS, Kubin M, et al. Tumoricidal activity of tumor necrosis factor-related apoptosis-inducing ligand in vivo. Nat Med. 1999;5:157-63.

[132] Stuckey DW, Shah K. TRAIL on trial: preclinical advances in cancer therapy. Trends Mol Med. 2013;19:685-94.

[133] French LE, Tschopp J. The TRAIL to selective tumor death. Nat Med. 1999;5:146-7.

[134] Roberts LR. Sorafenib in liver cancer--just the beginning. N Engl J Med. 2008;359:420-2.

[135] Forner A, Llovet JM, Bruix J. Hepatocellular carcinoma. Lancet. 2012;379:1245-55.

[136] El-Serag HB. Hepatocellular carcinoma. N Engl J Med. 2011;365:1118-27.

[137] Villanueva A, Hernandez-Gea V, Llovet JM. Medical therapies for hepatocellular carcinoma: a critical view of the evidence. Nat Rev Gastroenterol Hepatol. 2013;10:34-42.

[138] Llovet JM, Ricci S, Mazzaferro V, Hilgard P, Gane E, Blanc JF, et al. Sorafenib in advanced hepatocellular carcinoma. N Engl J Med. 2008;359:378-90.

[139] Xie B, Wang D, Spechler S. Sorafenib for treatment of hepatocellular carcinoma: a systematic review. Dig Dis Sci. 2012;57:1122-9.

[140] Benson AB, Abrams TA, Ben-Josef E, Bloomston PM, Botha JF, Clary BM, et al. Hepatobiliary cancers. J Natl Compr Canc Netw. 2009;7:350-91.

[141] Bruix J, Raoul J-L, Sherman M, Mazzaferro V, Bolondi L, Craxi A, et al. Efficacy and safety of sorafenib in patients with advanced hepatocellular carcinoma: subanalyses of a phase III trial. J Hepatol. 2012;57:821-9.

[142] Zender L, Xue W, Zuber J, Semighini CP, Krasnitz A, Ma B, et al. An oncogenomics-based in vivo RNAi screen identifies tumor suppressors in liver cancer. Cell. 2008;135:852-64.

[143] Tabernero J, Shapiro GI, LoRusso PM, Cervantes A, Schwartz GK, Weiss GJ, et al. First-in-humans trial of an RNA interference therapeutic targeting VEGF and KSP in cancer patients with liver involvement. Cancer Discovery. 2013;3:406-17.

[144] Rudalska R, Dauch D, Longerich T, McJunkin K, Wuestefeld T, Kang T-W, et al. In vivo RNAi screening identifies a mechanism of sorafenib resistance in liver cancer. Nat Med. 2014;20:1138-46.

[145] Xu CR, Lee SA, Chen X. RNA interference as therapeutics for hepatocellular carcinoma. Recent Pat Anticancer Drug Discov. 2011;6:106-15.

[146] Li J-M, Zhao M-X, Su H, Wang Y-Y, Tan C-P, Ji L-N, et al. Multifunctional quantum-dot-based siRNA delivery for HPV18 E6 gene silence and intracellular imaging. Biomaterials. 2011;32:7978-87.

[147] Whitehead KA, Langer R, Anderson DG. Knocking down barriers: advances in siRNA delivery. Nat Rev Drug Discovery. 2009;8:129-38.

[148] Hsu S-h, Yu B, Wang X, Lu Y, Schmidt CR, Lee RJ, et al. Cationic lipid nanoparticles for therapeutic delivery of siRNA and miRNA to murine liver tumor. Nanomedicine. 2013;9:1169-80.

[149] Wu C, Gong F, Pang P, Shen M, Zhu K, Cheng D, et al. An RGD-modified MRI-visible polymeric vector for targeted siRNA delivery to hepatocellular carcinoma in nude mice. PLoS ONE. 2013;8:e66416.

[150] Chen J, Zhu S, Tong L, Li J, Chen F, Han Y, et al. Superparamagnetic iron oxide nanoparticles mediated 131I-hVEGF siRNA inhibits hepatocellular carcinoma tumor growth in nude mice. BMC Cancer. 2014;14:114.

[151] Dudek H, Wong DH, Arvan R, Shah A, Wortham K, Ying B, et al. Knockdown of β-catenin with dicer-substrate siRNAs reduces liver tumor burden in vivo. Mol Ther. 2014;22:92-101.

[152] Bogorad RL, Yin H, Zeigerer A, Nonaka H, Ruda VM, Zerial M, et al. Nanoparticle-formulated siRNA targeting integrins inhibits hepatocellular carcinoma progression in mice. Nat Commun. 2014;5.

[153] Ding Y, Wang W, Feng M, Wang Y, Zhou J, Ding X, et al. A biomimetic nanovector-mediated targeted cholesterol-conjugated siRNA delivery for tumor gene therapy. Biomaterials. 2012;33:8893-905.

[154] Kievit FM, Zhang M. Surface engineering of iron oxide nanoparticles for targeted cancer therapy. Acc Chem Res. 2011;44:853-62.

[155] Liu YJ, Chen ZJ, Liu CX, Yu DX, Lu ZJ, Zhang N. Gadolinium-loaded polymeric nanoparticles modified with anti-VEGF as multifunctional MRI contrast agents for the diagnosis of liver cancer. Biomaterials. 2011;32:5167-76.

[156] Diez S, Navarro G, de Ilarduya CT. In vivo targeted gene delivery by cationic nanoparticles for treatment of hepatocellular carcinoma. J Gene Med. 2009;11:38-45.

[157] Liu P, Li Z, Zhu M, Sun Y, Li Y, Wang H, et al. Preparation of EGFR monoclonal antibody conjugated nanoparticles and targeting to hepatocellular carcinoma. J Mater Sci: Mater Med. 2010;21:551-6.

[158] Park JO, Stephen Z, Sun C, Veiseh O, Kievit FM, Fang C, et al. Glypican-3 targeting of liver cancer cells using multifunctional nanoparticles. Mol Imaging. 2011;10:69-77.

[159] Howard KA, Rahbek UL, Liu X, Damgaard CK, Glud SZ, Andersen MO, et al. RNA interference in vitro and in vivo using a chitosan/siRNA nanoparticle system. Mol Ther. 2006;14:476-84.

[160] Rinaudo M. Chitin and chitosan: properties and applications. Prog Polym Sci. 2006;31:603-32.

[161] Nakatsura T, Yoshitake Y, Senju S, Monji M, Komori H, Motomura Y, et al. Glypican-3, overexpressed specifically in human hepatocellular carcinoma, is a novel tumor marker. Biochem Biophys Res Commun. 2003;306:16-25.

[162] Capurro MI, Xiang YY, Lobe C, Filmus J. Glypican-3 promotes the growth of hepatocellular carcinoma by stimulating canonical Wnt signaling. Cancer Res. 2005;65:6245-54.

[163] Sham JG, Kievit FM, Grierson JR, Miyaoka RS, Yeh MM, Zhang M, et al. Glypican-3-targeted 89Zr PET imaging of hepatocellular carcinoma. J Nucl Med. 2014;55:799-804.

[164] Sham JG, Kievit FM, Grierson JR, Chiarelli PA, Miyaoka RS, Zhang M, et al. Glypican-3-targeting F(ab′)2 for (89)Zr PET of hepatocellular carcinoma. J Nucl Med. 2014;55:2032-7.

[165] Bhattarai N, Ramay HR, Gunn J, Matsen FA, Zhang M. PEG-grafted chitosan as an injectable thermosensitive hydrogel for sustained protein release. J Controlled Release. 2005;103:609-24.

[166] Kievit FM, Stephen ZR, Wang K, Dayringer CJ, Sham JG, Ellenbogen RG, et al. Nanoparticle mediated silencing of DNA repair sensitizes pediatric brain tumor cells to γ-irradiation. Mol Oncol. 2015;9:1071-80.

[167] Popović Z, Liu W, Chauhan VP, Lee J, Wong C, Greytak AB, et al. A nanoparticle size series for in vivo fluorescence imaging. Angew Chem Int Ed Engl. 2010;49:8649-52.

[168] Godbey WT, Wu KK, Mikos AG. Poly(ethylenimine) and its role in gene delivery. J Controlled Release. 1999;60:149-60.

[169] Kojiro M. Histopathology of liver cancers. Best Pract Res, Clin Gastroenterol. 2005;19:39-62.

[170] Maeda H, Bharate GY, Daruwalla J. Polymeric drugs for efficient tumor-targeted drug delivery based on EPR-effect. Eur J Pharm Biopharm. 2009;71:409-19.

[171] Cho KJ, Wang X, Nie SM, Chen Z, Shin DM. Therapeutic nanoparticles for drug delivery in cancer. Clin Cancer Res. 2008;14:1310-6.

[172] Jokerst JV, Lobovkina T, Zare RN, Gambhir SS. Nanoparticle PEGylation for imaging and therapy. Nanomedicine. 2011;6:715-28.

[173] Albanese A, Tang PS, Chan WCW. The effect of nanoparticle size, shape, and surface chemistry on biological systems. Annu Rev Biomed Eng. 2012;14:1-16.

[174] Wang K, Kievit FM, Florczyk SJ, Stephen ZR, Zhang M. 3D porous chitosan-alginate scaffolds as an in vitro model for evaluating nanoparticle-mediated tumor targeting and gene delivery to prostate cancer. Biomacromolecules. 2015;16:3362-72.

[175] Wang K, Park JO, Zhang M. Treatment of glioblastoma multiforme using a combination of small interfering RNA targeting epidermal growth factor receptor and β-catenin. J Gene Med. 2013;15:42-50.

[176] Budhu A, Jia H-L, Forgues M, Liu C-G, Goldstein D, Lam A, et al. Identification of metastasis-related microRNAs in hepatocellular carcinoma. Hepatology. 2008;47:897-907.

[177] Ye Q-H, Qin L-X, Forgues M, He P, Kim JW, Peng AC, et al. Predicting hepatitis B virus-positive metastatic hepatocellular carcinomas using gene expression profiling and supervised machine learning. Nat Med. 2003;9:416-23.

[178] Shand N, Weber F, Mariani L, Bernstein M, Gianella-Borradori A, Long Z, et al. A phase 1-2 clinical trial of gene therapy for recurrent glioblastoma multiforme by tumor transduction with the herpes simplex thymidine kinase gene followed by ganciclovir. GLI328 European-Canadian Study Group. Hum Gene Ther. 1999;10:2325-35.

[179] Chin L, Meyerson M, Aldape K, Bigner D, Mikkelsen T, VandenBerg S, et al. Comprehensive genomic characterization defines human glioblastoma genes and core pathways. Nature. 2008;455:1061-8.

[180] Kummar S, Chen HX, Wright J, Holbeck S, Millin MD, Tomaszewski J, et al. Utilizing targeted cancer therapeutic agents in combination: novel approaches and urgent requirements. Nat Rev Drug Discov. 2010;9:843-56.

[181] Haas-Kogan DA, Prados MD, Tihan T, Eberhard DA, Jelluma N, Arvold ND, et al. Epidermal growth factor receptor, protein kinase B/Akt, and glioma response to erlotinib. J Natl Cancer Inst. 2005;97:880-7.

[182] Mellinghoff IK, Wang MY, Vivanco I, Haas-Kogan DA, Zhu SJ, Dia EQ, et al. Molecular determinants of the response of glioblastomas to EGFR kinase inhibitors. N Engl J Med. 2005;353:2012-24.

[183] Zhu H, Acquaviva J, Ramachandran P, Boskovitz A, Woolfenden S, Pfannl R, et al. Oncogenic EGFR signaling cooperates with loss of tumor suppressor gene functions in gliomagenesis. Proc Natl Acad Sci U S A. 2009;106:2712-6.

[184] Shinojima N, Tada K, Shiraishi S, Kamiryo T, Kochi M, Nakamura H, et al. Prognostic value of epidermal growth factor receptor in patients with glioblastoma multiforme. Cancer Res. 2003;63:6962-70.

[185] Smith JS, Tachibana I, Passe SM, Huntley BK, Borell TJ, Iturria N, et al. PTEN mutation, EGFR amplification, and outcome in patients with anaplastic astrocytoma and glioblastoma multiforme. J Natl Cancer Inst. 2001;93:1246-56.

[186] van den Bent MJ, Brandes AA, Rampling R, Kouwenhoven MCM, Kros JM, Carpentier AF, et al. Randomized phase II trial of erlotinib versus temozolomide or carmustine in recurrent glioblastoma: EORTC brain tumor group study 26034. J Clin Oncol. 2009;27:1268-74.

[187] Lassman AB, Rossi MR, Razier JR, Abrey LE, Lieberman FS, Grefe CN, et al. Molecular study of malignant gliomas treated with epidermal growth factor receptor inhibitors: tissue analysis from North American Brain Tumor Consortium Trials 01-03 and 00-01. Clin Cancer Res. 2005;11:7841-50.

[188] Franceschi E, Cavallo G, Lonardi S, Magrini E, Tosoni A, Grosso D, et al. Gefitinib in patients with progressive high-grade gliomas: a multicentre phase II study by Gruppo Italiano Cooperativo di Neuro-Oncologia (GICNO). Br J Cancer. 2007;96:1047-51.

[189] Kreisl TN, Kim L, Moore K, Duic P, Royce C, Stroud I, et al. Phase II trial of single-agent bevacizumab followed by bevacizumab plus irinotecan at tumor progression in recurrent glioblastoma. J Clin Oncol. 2009;27:740-5.

[190] Hasselbalch B, Lassen U, Poulsen HS, Stockhausen MT. Cetuximab insufficiently inhibits glioma cell growth due to persistent EGFR downstream signaling. Cancer Invest. 2010;28:775-87.

[191] Reya T, Clevers H. Wnt signalling in stem cells and cancer. Nature. 2005;434:843-50.

[192] Moon RT, Kohn AD, Ferrari GVD, Kaykas A. WNT and beta-catenin signalling: diseases and therapies. Nat Rev Genet. 2004;5:691-701.

[193] Sareddy GR, Panigrahi M, Challa S, Mahadevan A, Babu PP. Activation of Wnt/β-catenin/Tcf signaling pathway in human astrocytomas. Neurochem Int. 2009;55:307-17.

[194] Liu C, Tu YY, Sun XY, Jiang J, Jin XD, Bo XF, et al. Wnt/beta-Catenin pathway in human glioma: expression pattern and clinical/prognostic correlations. Clin Exp Med. 2011;11:105-12.

[195] Liu X, Wang L, Zhao S, Ji X, Luo Y, Ling F. β-Catenin overexpression in malignant glioma and its role in proliferation and apoptosis in glioblastma cells. Med Oncol. 2010;28:608-14.

[196] Pu P, Zhang Z, Kang C, Jiang R, Jia Z, Wang G, et al. Downregulation of Wnt2 and β-catenin by siRNA suppresses malignant glioma cell growth. Cancer Gene Ther. 2008;16:351-61.

[197] Shi Z, Qian X, Li L, Zhang J, Zhu S, Zhu J, et al. Nuclear translocation of β-catenin is essential for glioma cell survival. J Neuroimmune Pharmacol. 2012:1-12.

[198] Yang W, Xia Y, Ji H, Zheng Y, Liang J, Huang W, et al. Nuclear PKM2 regulates β-catenin transactivation upon EGFR activation. Nature. 2011;478:118-22.

[199] Hu T, Li C. Convergence between Wnt-beta-catenin and EGFR signaling in cancer. Mol Cancer. 2010;9:1476-4598.

[200] Yue X, Lan F, Yang W, Yang Y, Han L, Zhang A, et al. Interruption of β-catenin suppresses the EGFR pathway by blocking multiple oncogenic targets in human glioma cells. Brain Res. 2010;1366:27-37.

[201] Diermeier S, Schmidt-Bruecken E, Kubbies M, Kunz-Schughart LA, Brockhoff G. Exposure to continuous bromodeoxyuridine (BrdU) differentially affects cell cycle progression of human breast and bladder cancer cell lines. Cell Prolif. 2004;37:195-206.

[202] Gao L, Li F, Dong B, Zhang J, Rao Y, Cong Y, et al. Inhibition of STAT3 and ErbB2 suppresses tumor growth, enhances radiosensitivity, and induces mitochondria-dependent apoptosis in glioma cells. Int J Radiat Oncol Biol Phys. 2010;77:1223-31.

[203] Geback T, Schulz MMP, Koumoutsakos P, Detmar M. TScratch: a novel and simple software tool for automated analysis of monolayer wound healing assays. Biotechniques. 2009;46:265-74.

[204] Ji H, Wang J, Nika H, Hawke D, Keezer S, Ge Q, et al. EGF-induced ERK activation promotes CK2-mediated disassociation of α-catenin from β-catenin and transactivation of β-catenin. Mol Cell. 2009;36:547-59.

[205] Tan X, Apte U, Micsenyi A, Kotsagrelos E, Luo J-H, Ranganathan S, et al. Epidermal growth factor receptor: a novel target of the Wnt/β-catenin pathway in liver. Gastroenterology. 2005;129:285-302.

[206] Clevers H. Wnt/β-catenin signaling in development and disease. Cell. 2006;127:469-80.

[207] MacDonald BT, Tamai K, He X. Wnt/β-catenin signaling: components, mechanisms, and diseases. Dev Cell. 2009;17:9-26.

[208] Vollmann A, Vornlocher HP, Stempfl T, Brockhoff G, Apfel R, Bogdahn U. Effective silencing of EGFR with RNAi demonstrates non-EGFR dependent proliferation of glioma cells. Int J Oncol. 2006;28:1531-42.

[209] Kang CS, Pu PY, Li YH, Zhang ZY, Qiu MZ, Huang Q, et al. An in vitro study on the suppressive effect of glioma cell growth induced by plasmid-based small interference RNA (siRNA) targeting human epidermal growth factor receptor. J Neurooncol. 2005;74:267-73.

[210] Lefranc F, Brotchi J, Kiss R. Possible future issues in the treatment of glioblastomas: special emphasis on cell migration and the resistance of migrating glioblastoma cells to apoptosis. J Clin Oncol. 2005;23:2411-22.

[211] Lefranc F, Sadeghi N, Camby I, Metens T, Dewitte O, Kiss R. Present and potential future issues in glioblastoma treatment. Expert Rev Anticancer Ther. 2006;6:719-32.

[212] Li XQ, Lu Y, Pan TH, Fan Z. Roles of autophagy in cetuximab-mediated cancer therapy against EGFR. Autophagy. 2010;6:1066-77.

[213] Eimer S, Belaud-Rotureau MA, Airiau K, Jeanneteau M, Laharanne E, Veron N, et al. Autophagy inhibition cooperates with erlotinib to induce glioblastoma cell death. Cancer Biol Ther. 2011;11:1017-27.

[214] Klionsky D. Methods in enzymology Vol 453: autophagy in disease and clinical applications, Pt C. San Diego: Elsevier Academic Press Inc; 2009. p. 1-481.

[215] Rappl A, Piontek G, Schlegel J. EGFR-dependent migration of glial cells is mediated by reorganisation of N-cadherin. J Cell Sci. 2008;121:4089-97.

[216] Lyu J, Lee KS, Joo CK. Transactivation of EGFR mediates insulin-stimulated ERK1/2 activation and enhanced cell migration in human corneal epithelial cells. Mol Vis. 2006;12:1403-10.

[217] Roth W, Wild-Bode C, Platten M, Grimmel C, Melkonyan HS, Dichgans J, et al. Secreted frizzled-related proteins inhibit motility and promote growth of human malignant glioma cells. Oncogene. 2000;19:4210-20.

[218] Silber JR, Bobola MS, Blank A, Schoeler KD, Haroldson PD, Huynh MB, et al. The apurinic/apyrimidinic endonuclease activity of Ape1/Ref-1 contributes to human glioma cell resistance to alkylating agents and is elevated by oxidative stress. Clin Cancer Res. 2002;8:3008-18.

[219] Stupp R, Hegi ME, Mason WP, van den Bent MJ, Taphoorn MJB, Janzer RC, et al. Effects of radiotherapy with concomitant and adjuvant temozolomide versus radiotherapy alone on survival in glioblastoma in a randomised phase III study: 5-year analysis of the EORTC-NCIC trial. Lancet Oncol. 2009;10:459-66.

[220] Stupp R, Mason WP, van den Bent MJ, Weller M, Fisher B, Taphoorn MJB, et al. Radiotherapy plus concomitant and adjuvant temozolomide for glioblastoma. N Engl J Med. 2005;352:987-96.

[221] Bobola MS, Tseng SH, Blank A, Berger MS, Silber JR. Role of O6-methylguanine-DNA methyltransferase in resistance of human brain tumor cell lines to the clinically relevant methylating agents temozolomide and streptozotocin. Clin Cancer Res. 1996;2:735-41.

[222] Gerson SL. MGMT: its role in cancer aetiology and cancer therapeutics. Nat Rev Cancer. 2004;4:296-307.

[223] Silber JR, Bobola MS, Blank A, Chamberlain MC. O6-methylguanine-DNA methyltransferase in glioma therapy: promise and problems. Biochim Biophys Acta, Rev Cancer. 2012;1826:71-82.

[224] Calabrese C, Poppleton H, Kocak M, Hogg TL, Fuller C, Hamner B, et al. A perivascular niche for brain tumor stem cells. Cancer Cell. 2007;11:69-82.

[225] Vescovi AL, Galli R, Reynolds BA. Brain tumour stem cells. Nat Rev Cancer. 2006;6:425-36.

[226] Pistollato F, Abbadi S, Rampazzo E, Persano L, Della Puppa A, Frasson C, et al. Intratumoral hypoxic gradient drives stem cells distribution and MGMT expression in glioblastoma. Stem Cells. 2010;28:851-62.

[227] Beier D, Schulz J, Beier C. Chemoresistance of glioblastoma cancer stem cells-much more complex than expected. Mol Cancer. 2011;10:128.

[228] Chen J, McKay RM, Parada LF. Malignant glioma: lessons from genomics, mouse models, and stem cells. Cell. 2012;149:36-47.

[229] Chen J, Li Y, Yu T-S, McKay RM, Burns DK, Kernie SG, et al. A restricted cell population propagates glioblastoma growth after chemotherapy. Nature. 2012;488:522-6.

[230] Hegi ME, Diserens A, Gorlia T, Hamou M, de Tribolet N, Weller M, et al. MGMT gene silencing and benefit from temozolomide in glioblastoma. N Engl J Med. 2005;352:997-1003.

[231] Esteller M, Garcia-Foncillas J, Andion E, Goodman SN, Hidalgo OF, Vanaclocha V, et al. Inactivation of the DNA-repair gene MGMT and the clinical response of gliomas to alkylating agents. N Engl J Med. 2000;343:1350-4.

[232] Schold SC, Kokkinakis DM, Chang SM, Berger MS, Hess KR, Schiff D, et al. O6-benzylguanine suppression of O6-alkylguanine-DNA alkyltransferase in anaplastic gliomas. Neuro Oncol. 2004;6:28-32.

[233] Quinn JA, Jiang SX, Reardon DA, Desjardins A, Vredenburgh JJ, Rich JN, et al. Phase II trial of temozolomide plus O6-benzylguanine in adults with recurrent, temozolomide-resistant malignant glioma. J Clin Oncol. 2009;27:1262-7.

[234] Quinn JA, Jiang SX, Reardon DA, Desjardins A, Vredenburgh JJ, Rich JN, et al. Phase I trial of temozolomide plus O6-benzylguanine 5-day regimen with recurrent malignant glioma. Neuro Oncol. 2009;11:556-61.

[235] Glover DJ, Lipps HJ, Jans DA. Towards safe, non-viral therapeutic gene expression in humans. Nat Rev Genet. 2005;6:299-310.

[236] Ogris M, Wagner E. Targeting tumors with non-viral gene delivery systems. Drug Discovery Today. 2002;7:479-85.

[237] de Fougerolles A, Vornlocher H-P, Maraganore J, Lieberman J. Interfering with disease: a progress report on siRNA-based therapeutics. Nat Rev Drug Discov. 2007;6:443-53.

[238] Kanasty R, Dorkin JR, Vegas A, Anderson D. Delivery materials for siRNA therapeutics. Nat Mater. 2013;12:967-77.

[239] Carlson BL, Grogan PT, Mladek AC, Schroeder MA, Kitange GJ, Decker PA, et al. Radiosensitizing effects of temozolomide observed *in vivo* only in a subset of O6-methylguanine-DNA methyltransferase methylated glioblastoma multiforme xenografts. Int J Radiat Oncol, Biol, Phys. 2009;75:212-9.

[240] Carlson BL, Pokorny JL, Schroeder MA, Sarkaria JN. Establishment, maintenance and in vitro and in vivo applications of primary human glioblastoma multiforme (GBM) xenograft models for translational biology studies and drug discovery. Curr Protoc Pharmacol. 2011;52:1-14.

[241] Bobola MS, Alnoor M, Chen JYS, Kolstoe DD, Silbergeld DL, Rostomily RC, et al. O6-methylguanine-DNA methyltransferase activity is associated with response to alkylating agent therapy and with MGMT promoter methylation in glioblastoma and anaplastic glioma. BBA Clinical. 2015;3:1-10.

[242] Burton K. A study of the conditions and mechanism of the diphenylamine reaction for the colorimetric estimation of deoxyribonucleic acid. Biochem J. 1956;62:315-23.

[243] Blow N. Small RNAs: Delivering the future. Nature. 2007;450:1117-20.

[244] Jager M, Schubert S, Ochrimenko S, Fischer D, Schubert US. Branched and linear poly(ethylene imine)-based conjugates: synthetic modification, characterization, and application. Chem Soc Rev. 2012;41:4755-67.

[245] Davis ME, Zuckerman JE, Choi CHJ, Seligson D, Tolcher A, Alabi CA, et al. Evidence of RNAi in humans from systemically administered siRNA via targeted nanoparticles. Nature. 2010;464:1067-U140.

[246] Song EW, Zhu PC, Lee SK, Chowdhury D, Kussman S, Dykxhoorn DM, et al. Antibody mediated in vivo delivery of small interfering RNAs via cell-surface receptors. Nat Biotechnol. 2005;23:709-17.

[247] Medarova Z, Pham W, Farrar C, Petkova V, Moore A. In vivo imaging of siRNA delivery and silencing in tumors. Nat Med. 2007;13:372-7.

[248] Stupp R, Hegi ME, Mason WP, van den Bent MJ, Taphoorn MJB, Janzer RC, et al. Effects of radiotherapy with concomitant and adjuvant temozolomide versus radiotherapy alone on survival in glioblastoma in a randomised phase III study: 5-year analysis of the EORTC-NCIC trial. Lancet Oncol. 2009;10:459-66.

[249] Hegi ME, Diserens AC, Godard S, Dietrich PY, Regli L, Ostermann S, et al. Clinical trial substantiates the predictive value of O-6-methylguanine-DNA methyltransferase promoter methylation in glioblastoma patients treated with temozolomide. Clin Cancer Res. 2004;10:1871-4.

[250] Gerson SL. Clinical relevance of MGMT in the treatment of cancer. J Clin Oncol. 2002;20:2388-99.

[251] Weller M, Stupp R, Reifenberger G, Brandes AA, van den Bent MJ, Wick W, et al. MGMT promoter methylation in malignant gliomas: ready for personalized medicine? Nat Rev Neurol. 2010;6:39-51.

[252] Lee MJ-E, Veiseh O, Bhattarai N, Sun C, Hansen SJ, Ditzler S, et al. Rapid pharmacokinetic and biodistribution studies using cholorotoxin-conjugated iron oxide nanoparticles: a novel non-radioactive method. PLoS ONE. 2010;5.

[253] Sarkaria JN, Carlson BL, Schroeder MA, Grogan P, Brown PD, Giannini C, et al. Use of an orthotopic xenograft model for assessing the effect of epidermal growth factor receptor amplification on glioblastoma radiation response. Clin Cancer Res. 2006;12:2264-71.

[254] Higgins DM, Wang R, Milligan B, Schroeder M, Carlson B, Pokorny J, et al. Brain tumor stem cell multipotency correlates with Nanog expression and extent of passaging in human glioblastoma xenografts. Oncotarget. 2013;4.

[255] Allen C, Opyrchal M, Aderca I, Schroeder MA, Sarkaria JN, Domingo E, et al. Oncolytic measles virus strains have significant antitumor activity against glioma stem cells. Gene Ther. 2013;20:444-9.

[256] Anido J, Saez-Borderias A, Gonzalez-Junca A, Rodon L, Folch G, Carmona MA, et al. TGF-β receptor inhibitors target the CD44(high)/Id1(high) glioma-initiating cell population in human glioblastoma. Cancer Cell. 2010;18:655-68.

[257] Pietras A, Katz AM, Ekstrom EJ, Wee B, Halliday JJ, Pitter KL, et al. Osteopontin-CD44 signaling in the glioma perivascular niche enhances cancer stem cell phenotypes and promotes aggressive tumor growth. Cell Stem Cell. 2014;14:357-69.

[258] Fan X, Khaki L, Zhu TS, Soules ME, Talsma CE, Gul N, et al. NOTCH pathway blockade depletes CD133-positive glioblastoma cells and inhibits growth of tumor neurospheres and xenografts. Stem Cells. 2010;28:5-16.

[259] Woolard K, Fine HA. Glioma stem cells: better flat than round. Cell Stem Cell. 2009;4:466-7.

[260] Cheng L, Huang Z, Zhou W, Wu Q, Donnola S, Liu James K, et al. Glioblastoma stem cells generate vascular pericytes to support vessel function and tumor growth. Cell. 2013;153:139-52.

[261] Meacham CE, Morrison SJ. Tumour heterogeneity and cancer cell plasticity. Nature. 2013;501:328-37.

[262] Yoshida T, Matsuda Y, Naito Z, Ishiwata T. CD44 in human glioma correlates with histopathological grade and cell migration. Pathol Int. 2012;62:463-70.

[263] Soeda A, Park M, Lee D, Mintz A, Androutsellis-Theotokis A, McKay RD, et al. Hypoxia promotes expansion of the CD133-positive glioma stem cells through activation of HIF-1[alpha]. Oncogene. 2009;28:3949-59.

[264] Bleau AM, Huse JT, Holland EC. The ABCG2 resistance network of glioblastoma. Cell Cycle. 2009;8:2936-44.

[265] Zheng HW, Ying HQ, Yan HY, Kimmelman AC, Hiller DJ, Chen AJ, et al. p53 and Pten control neural and glioma stem/progenitor cell renewal and differentiation. Nature. 2008;455:1129-U13.

[266] Katoh Y, Katoh M. Hedgehog target genes: mechanisms of carcinogenesis induced by aberrant hedgehog signaling activation. Curr Mol Med. 2009;9:873-86.

[267] Cen L, Carlson BL, Schroeder MA, Ostrem JL, Kitange GJ, Mladek AC, et al. p16-Cdk4-Rb axis controls sensitivity to a cyclin-dependent kinase inhibitor PD0332991 in glioblastoma xenograft cells. Neuro Oncol. 2012;14:870-81.

[268] Siegel R, Ma J, Zou Z, Jemal A. Cancer statistics, 2014. CA Cancer J Clin. 2014;64:9-29.

[269] Heidenreich A, Bellmunt J, Bolla M, Joniau S, Mason M, Matveev V, et al. EAU guidelines on prostate cancer. part 1: screening, diagnosis, and treatment of clinically localised disease. Eur Urol. 2011;59:61-71.

[270] Zelefsky MJ, Fuks Z, Hunt M, Yamada Y, Marion C, Ling CC, et al. High-dose intensity modulated radiation therapy for prostate cancer: Early toxicity and biochemical outcome in 772 patients. Int J Radiat Oncol, Biol, Phys. 2002;53:1111-6.

[271] Kuban DA, Tucker SL, Dong L, Starkschall G, Huang EE, Cheung MR, et al. Long-term results of the M. D. Anderson randomized dose-escalation trial for prostate cancer. Int J Radiat Oncol, Biol, Phys. 2008;70:67-74.

[272] Djavan B, Nasu Y. Prostate cancer gene therapy-what have we learned and where are we going? Rev Urol. 2001;3:179-86.

[273] Schenk E, Essand M, Bangma CH, Barber C, Behr JP, Briggs S, et al. Clinical adenoviral gene therapy for prostate cancer. Hum Gene Ther. 2010;21:807-13.

[274] Freytag SO, Movsas B, Aref I, Stricker H, Peabody J, Pegg J, et al. Phase I trial of replication-competent adenovirus-mediated suicide gene therapy combined with IMRT for prostate cancer. Mol Ther. 2007;15:1016-23.

[275] Harrington KJ, Spitzweg C, Bateman AR, Morris JC, Vile RG. Gene therapy for prostate cancer: current status and future prospects. J Urol. 2001;166:1220-33.

[276] Steiner MS, Gingrich JR. Gene therapy for prostate cancer: where are we now? J Urol. 2000;164:1121-36.

[277] Boisselier E, Astruc D. Gold nanoparticles in nanomedicine: preparations, imaging, diagnostics, therapies and toxicity. Chem Soc Rev. 2009;38:1759-82.

[278] Gao XH, Cui YY, Levenson RM, Chung LWK, Nie SM. In vivo cancer targeting and imaging with semiconductor quantum dots. Nat Biotechnol. 2004;22:969-76.

[279] Chia SL, Tay CY, Setyawati MI, Leong DT. Biomimicry 3D gastrointestinal spheroid platform for the assessment of toxicity and inflammatory effects of zinc oxide nanoparticles. Small. 2015;11:702-12.

[280] Leong DT, Ng KW. Probing the relevance of 3D cancer models in nanomedicine research. Adv Drug Deliv Rev. 2014;79–80:95-106.

[281] Astashkina AI, Jones CF, Thiagarajan G, Kurtzeborn K, Ghandehari H, Brooks BD, et al. Nanoparticle toxicity assessment using an in vitro 3-D kidney organoid culture model. Biomaterials. 2014;35:6323-31.

[282] Phan-Lai V, Florczyk SJ, Kievit FM, Wang K, Gad E, Disis ML, et al. Three-dimensional scaffolds to evaluate tumor associated fibroblast-mediated suppression of breast tumor specific T cells. Biomacromolecules. 2013;14:1330-7.

[283] Leung M, Kievit F, Florczyk S, Veiseh O, Wu J, Park J, et al. Chitosan-alginate scaffold culture system for hepatocellular carcinoma increases malignancy and drug resistance. Pharm Res. 2010;27:1939-48.

[284] Kievit FM, Florczyk SJ, Leung MC, Wang K, Wu JD, Silber JR, et al. Proliferation and enrichment of CD133(+) glioblastoma cancer stem cells on 3D chitosan-alginate scaffolds. Biomaterials. 2014;35:9137-43.

[285] Muzzarelli RAA. Chitosan composites with inorganics, morphogenetic proteins and stem cells, for bone regeneration. Carbohydr Polym. 2011;83:1433-45.

[286] Rinaudo M. Main properties and current applications of some polysaccharides as biomaterials. Polym Int. 2008;57:397-430.

[287] Scott JE. Supramolecular organization of extracellular matrix glycosaminoglycans, in vitro and in the tissues. Faseb J. 1992;6:2639-45.

[288] Strack RL, Strongin DE, Bhattacharyya D, Tao W, Berman A, Broxmeyer HE, et al. A noncytotoxic DsRed variant for whole-cell labeling. Nat Meth. 2008;5:955-7.

[289] Li ZS, Ramay HR, Hauch KD, Xiao DM, Zhang MQ. Chitosan-alginate hybrid scaffolds for bone tissue engineering. Biomaterials. 2005;26:3919-28.

[290] Carmell MA, Girard A, van de Kant HJG, Bourc'his D, Bestor TH, de Rooij DG, et al. MIWI2 is essential for spermatogenesis and repression of transposons in the mouse male germline. Dev Cell. 2007;12:503-14.

[291] Matsubara T, Kida K, Yamaguchi A, Hata K, Ichida F, Meguro H, et al. BMP2 regulates osterix through Msx2 and Runx2 during osteoblast differentiation. J Biol Chem. 2008;283:29119-25.

[292] Shannon MB, Patton BL, Harvey SJ, Miner JH. A hypomorphic mutation in the mouse Laminin α5 Gene (*Lama5*) causes polycystic kidney disease. Journal of the American Society of Nephrology. 2006;17:1913-22.

[293] Cooke Vesselina G, LeBleu Valerie S, Keskin D, Khan Z, O'Connell Joyce T, Teng Y, et al. Pericyte depletion results in hypoxia-associated epithelial-to-mesenchymal transition and metastasis mediated by met signaling pathway. Cancer Cell. 2012;21:66-81.

[294] Sánchez-Duffhues G, de Vinuesa AG, Lindeman JH, Mulder-Stapel A, DeRuiter MC, Van Munsteren C, et al. SLUG is expressed in endothelial cells lacking primary cilia to promote cellular calcification. Arterioscler Thromb Vasc Biol. 2015;35:616-27.

[295] Ritson SA. The transcriptional regulation of junctional adhesion molecule 2 by E-cadherin in mouse embryonic stem cells. Manchester, UK: The University of Manchester; 2011.

[296] de Vries WN, Evsikov AV, Haac BE, Fancher KS, Holbrook AE, Kemler R, et al. Maternal β-catenin and E-cadherin in mouse development. Development. 2004;131:4435-45.

[297] Bissell MJ, Hines WC. Why don't we get more cancer? A proposed role of the microenvironment in restraining cancer progression. Nat Med. 2011;17:320-9.

[298] Hutmacher DW. Biomaterials offer cancer research the third dimension. Nat Mater. 2010;9:90-3.

[299] Kelm JM, Timmins NE, Brown CJ, Fussenegger M, Nielsen LK. Method for generation of homogeneous multicellular tumor spheroids applicable to a wide variety of cell types. Biotechnology and Bioengineering. 2003;83:173-80.

[300] Ong S-M, Zhao Z, Arooz T, Zhao D, Zhang S, Du T, et al. Engineering a scaffold-free 3D tumor model for in vitro drug penetration studies. Biomaterials. 2010;31:1180-90.

[301] Ivascu A, Kubbies M. Rapid generation of single-tumor spheroids for high-throughput cell function and toxicity analysis. J Biomol Screening. 2006;11:922-32.

[302] Barrila J, Radtke AL, Crabbé A, Sarker SF, Herbst-Kralovetz MM, Ott CM, et al. Organotypic 3D cell culture models: using the rotating wall vessel to study host-pathogen interactions. Nat Rev Micro. 2010;8:791-801.

[303] Pickl M, Ries CH. Comparison of 3D and 2D tumor models reveals enhanced HER2 activation in 3D associated with an increased response to trastuzumab. Oncogene. 2008;28:461-8.

[304] Harma V, Virtanen J, Makela R, Happonen A, Mpindi J-P, Knuuttila M, et al. A comprehensive panel of three-dimensional models for studies of prostate cancer growth, invasion and drug responses. PLoS ONE. 2010;5.

[305] Chignola R, Schenetti A, Andrighetto G, Chiesa E, Foroni R, Sartoris S, et al. Forecasting the growth of multicell tumour spheroids: implications for the dynamic growth of solid tumours. Cell Prolif. 2000;33:219-29.

[306] Lu P, Weaver VM, Werb Z. The extracellular matrix: a dynamic niche in cancer progression. J Cell Biol. 2012;196:395-406.

[307] Davis GE, Senger DR. Endothelial extracellular matrix: biosynthesis, remodeling, and functions during vascular morphogenesis and neovessel stabilization. Circ Res. 2005;97:1093-107.

[308] Lee GY, Kenny PA, Lee EH, Bissell MJ. Three-dimensional culture models of normal and malignant breast epithelial cells. Nat Methods. 2007;4:359-65.

[309] Hotary KB, Allen ED, Brooks PC, Datta NS, Long MW, Weiss SJ. Membrane type I matrix metalloproteinase usurps tumor growth control imposed by the three-dimensional extracellular matrix. Cell. 2003;114:33-45.

[310] Lutolf MP, Lauer-Fields JL, Schmoekel HG, Metters AT, Weber FE, Fields GB, et al. Synthetic matrix metalloproteinase-sensitive hydrogels for the conduction of tissue regeneration: engineering cell-invasion characteristics. Proc Natl Acad Sci U S A. 2003;100:5413-8.

[311] Kalluri R, Weinberg RA. The basics of epithelial-mesenchymal transition. J Clin Invest. 2009;119:1420-8.

[312] Hanahan D, Weinberg Robert A. Hallmarks of cancer: the next generation. Cell. 2011;144:646-74.

[313] Xie D, Gore C, Liu J, Pong R-C, Mason R, Hao G, et al. Role of DAB2IP in modulating epithelial-to-mesenchymal transition and prostate cancer metastasis. Proc Natl Acad Sci U S A. 2010;107:2485-90.

[314] Saini S, Majid S, Yamamura S, Tabatabai L, Suh SO, Shahryari V, et al. Regulatory role of mir-203 in prostate cancer progression and metastasis. Clin Cancer Res. 2011;17:5287-98.

[315] Cano A, Perez-Moreno MA, Rodrigo I, Locascio A, Blanco MJ, del Barrio MG, et al. The transcription factor Snail controls epithelial-mesenchymal transitions by repressing E-cadherin expression. Nat Cell Biol. 2000;2:76-83.

[316] Beach S, Tang H, Park S, Dhillon AS, Keller ET, Kolch W, et al. Snail is a repressor of RKIP transcription in metastatic prostate cancer cells. Oncogene. 2007;27:2243-8.

[317] Liu YN, Abou-Kheir W, Yin JJ, Fang L, Hynes P, Casey O, et al. Critical and reciprocal regulation of KLF4 and SLUG in transforming growth factor β-initiated prostate cancer epithelial-mesenchymal transition. Mol Cell Biol. 2012;32:941-53.

[318] Baygi ME, Soheili ZS, Essmann F, Deezagi A, Engers R, Goering W, et al. Slug/SNAI2 regulates cell proliferation and invasiveness of metastatic prostate cancer cell lines. Tumor Biol. 2010;31:297-307.

[319] Kwok WK, Ling M-T, Lee T-W, Lau TCM, Zhou C, Zhang X, et al. Up-regulation of TWIST in prostate cancer and its implication as a therapeutic target. Cancer Res. 2005;65:5153-62.

[320] Yuen HF, Chua CW, Chan YP, Wong YC, Wang X, Chan KW. Significance of TWIST and E-cadherin expression in the metastatic progression of prostatic cancer. Histopathology. 2007;50:648-58.

[321] Liu J, Uygur B, Zhang Z, Shao L, Romero D, Vary C, et al. Slug inhibits proliferation of human prostate cancer cells via downregulation of cyclin D1 expression. The Prostate. 2010;70:1768-77.

[322] Leshem O, Madar S, Kogan-Sakin I, Kamer I, Goldstein I, Brosh R, et al. TMPRSS2/ERG promotes epithelial to mesenchymal transition through the ZEB1/ZEB2 axis in a prostate cancer model. PLoS ONE. 2011;6:e21650.

[323] Kong DJ, Li YW, Wang ZW, Banerjee S, Ahmad A, Kim HRC, et al. miR-200 regulates PDGF-D-mediated epithelial-mesenchymal transition, adhesion, and invasion of prostate cancer cells. Stem Cells. 2009;27:1712-21.

[324] Gandellini P, Folini M, Longoni N, Pennati M, Binda M, Colecchia M, et al. miR-205 exerts tumor-suppressive functions in human prostate through down-regulation of protein kinase C epsilon. Cancer Res. 2009;69:2287-95.

[325] Yao D, Dai C, Peng S. Mechanism of the mesenchymal-epithelial transition and its relationship with metastatic tumor formation. Mol Cancer Res. 2011;9:1608-20.

[326] Das R, Gregory PA, Hollier BG, Tilley WD, Selth LA. Epithelial plasticity in prostate cancer: principles and clinical perspectives. Trends in Molecular Medicine. 2014;20:643-51.

[327] Bae K-M, Parker NN, Dai Y, Vieweg J, Siemann DW. E-cadherin plasticity in prostate cancer stem cell invasion. Am J Cancer Res. 2011;1:71-84.

[328] De Marzo AM, Knudsen B, Chan-Tack K, Epstein JI. E-cadherin expression as a marker of tumor aggressiveness in routinely processed radical prostatectomy specimens. Urology. 1999;53:707-13.

[329] Rubin MA, Mucci NR, Figurski J, Fecko A, Pienta KJ, Day ML. E-cadherin expression in prostate cancer: a broad survey using high-density tissue microarray technology. Hum Pathol. 2001;32:690-7.

[330] Hlubek F, Brabletz T, Budczies J, Pfeiffer S, Jung A, Kirchner T. Heterogeneous expression of Wnt/β-catenin target genes within colorectal cancer. Int J Cancer. 2007;121:1941-8.

[331] Veiseh M, Gabikian P, Bahrami SB, Veiseh O, Zhang M, Hackman RC, et al. Tumor paint: a chlorotoxin:Cy5.5 bioconjugate for intraoperative visualization of cancer foci. Cancer Res. 2007;67:6882-8.

[332] Kircheis R, Wightman L, Schreiber A, Robitza B, Rossler V, Kursa M, et al. Polyethylenimine/DNA complexes shielded by transferrin target gene expression to tumors after systemic application. Gene Ther. 2001;8:28-40.

[333] Trudel D, Fradet Y, Meyer F, Harel F, Tétu B. Significance of MMP-2 expression in prostate cancer: an immunohistochemical study. Cancer Res. 2003;63:8511-5.

[334] Minchinton AI, Tannock IF. Drug penetration in solid tumours. Nat Rev Cancer. 2006;6:583-92.

[335] Jain RK, Stylianopoulos T. Delivering nanomedicine to solid tumors. Nat Rev Clin Oncol. 2010;7:653-64.

[336] Liotta LA, Kohn EC. The microenvironment of the tumour-host interface. Nature. 2001;411:375-9.

[337] Cabral H, Matsumoto Y, Mizuno K, Chen Q, Murakami M, Kimura M, et al. Accumulation of sub-100 nm polymeric micelles in poorly permeable tumours depends on size. Nat Nano. 2011;6:815-23.

[338] Wong C, Stylianopoulos T, Cui J, Martin J, Chauhan VP, Jiang W, et al. Multistage nanoparticle delivery system for deep penetration into tumor tissue. Proc Natl Acad Sci USA. 2011;108:2426-31.

[339] Sugahara KN, Teesalu T, Karmali PP, Kotamraju VR, Agemy L, Girard OM, et al. Tissue-penetrating delivery of compounds and nanoparticles into tumors. Cancer Cell. 2009;16:510-20.

[340] Ho DN, Kohler N, Sigdel A, Kalluri R, Morgan JR, Xu C, et al. Penetration of endothelial cell coated multicellular tumor spheroids by iron oxide nanoparticles. Theranostics. 2012;2:66-75.

[341] Robson T, Hirst DG. Transcriptional targeting in cancer gene therapy. J Biomed Biotechnol. 2003:110-37.

CURRICULUM VITAE

EDUCATION

University of Washington, Seattle, WA 12/2015
Ph.D., Materials Science and Engineering (Dual Ph.D. in Nanotechnology and Molecular Engineering)

Nanjing University of Technology, Nanjing, China 06/2008
M.S., Microbiology

California Polytechnic State University, San Luis Obispo, CA 09/2006–06/2007
Master student, Biomedical and General Engineering

Nanjing University of Technology, Nanjing, China 06/2005
B.E., Bioengineering

HONORS AND AWARDS

09/2013–09/2014: College of Engineering Dean's Fellowship, University of Washington
11/2014: Graduate and Professional Senate (GPSS) Travel Grants, University of Washington
06/2008: Excellent dissertation, Nanjing University of Technology
06/2004: The third-prize scholarship, Nanjing University of Technology
06/2003: The second-prize scholarship, Nanjing University of Technology
06/2002: The third-prize scholarship, Nanjing University of Technology
12/2001: The third place in the College English Grammar Test, Nanjing University of Technology

PUBLICATIONS

1. **Kui Wang**, Forrest M. Kievit, Peter A. Chiarelli, Zachary R. Stephen, John R. Silber, Richard G. Ellenbogen, and Miqin Zhang. Nanoparticle-mediated delivery of anti-MGMT siRNA sensitizes human glioblastoma cells and xenografts to temozolomide. *In preparation*
2. **Kui Wang**, Forrest M. Kievit, Yayi Deng, Ariane E. Erickson, John R. Silber, Richard G. Ellenbogen, and Miqin Zhang. Primary glioblastoma cell culture on three-dimensional chitosan-hyaluronic acid scaffolds increases stemness and drug resistance. *In preparation*
3. **Kui Wang**, Forrest M. Kievit, Jonathan Sham, Mike Jeon, Zachary R. Stephen, Arvind Bakthavatsalam, James O. Park, and Miqin Zhang. Iron oxide-based nanovector for tumor targeted siRNA delivery in an orthotopic hepatocellular carcinoma xenograft mouse model. *Small;* 2015, *In press*
4. **Kui Wang**, Forrest M. Kievit, Mike Jeon, John R. Silber, Richard G. Ellenbogen, and Miqin Zhang. Nanoparticle-mediated target delivery of TRAIL as gene therapy for glioblastoma. *Advanced Healthcare Materials;* 2015, *In press*
5. **Kui Wang**, Forrest M. Kievit, Stephen J. Florczyk, Zachary R. Stephen, and Miqin Zhang. 3D Porous Chitosan-alginate scaffolds as an *in vitro* model for evaluating nanoparticle-mediated tumor targeting and gene delivery to prostate cancer. *Biomacromolecules;* 2015; 16 (10): 3362–3372
6. Stephen J. Florczyk*****, **Kui Wang***, Soumen Jana, David Wood, Samara K. Sytsma, Jonathan Sham, Forrest M. Kievit, and Miqin Zhang. Porous chitosan-hyaluronic acid scaffolds as a mimic of glioblastoma microenvironment ECM. *Biomaterials;* 2013; 34 (38):10143–10150 ***co-first authors**
7. **Kui Wang**, James O. Park, and Miqin Zhang. Treatment of glioblastoma multiforme using combination siRNA targeting EGFR and β-catenin. *The Journal of Gene Medicine*; 2013; 15 (1): 42–50
8. Qingxin Mu, Guanyou Lin, Victoria Patton, **Kui Wang**, Oliver Press, and Miqin Zhang. Gemcitabine and chlorotoxin conjugated iron oxide nanoparticles for glioblastoma therapy. *Journal of Materials Chemistry B*; 2015, *In press*
9. Chen Fang, **Kui Wang**, Zachary R. Stephen, Qingxin Mu, Forrest M. Kievit, Daniel T. Chiu, Oliver W. Press, Miqin Zhang. Temozolomide nanoparticles for targeted glioblastoma therapy. *ACS applied materials & interfaces*; 2015; 7 (12): 6674–6682
10. Forrest M Kievit, Zachary R Stephen, **Kui Wang**, Christopher J Dayringer, Jonathan G

Sham, Richard G Ellenbogen, John R Silber, Miqin Zhang. Nanoparticle mediated silencing of DNA repair sensitizes pediatric brain tumor cells to γ-irradiation. *Molecular oncology;* 2015; 9 (6): 1071–1080

11. Qingxin Mu, Mike Jeon, Meng-Hsuan Hsiao, Victoria K. Patton, **Kui Wang**, Oliver W Press, Miqin Zhang. Stable and efficient paclitaxel nanoparticles for targeted glioblastoma therapy. *Advanced Healthcare Materials*; 2015; 4 (8): 1236–45
12. Zach R. Stephen, Forrest M. Kievit, Omid Veiseh, Peter A. Chiarelli, Chen Fang, **Kui Wang**, Shelby Hatzinger, Richard G. Ellenbogen, John R. Silber, and Miqin Zhang. Redox-responsive magnetic nanoparticle for targeted convection-enhanced delivery of O6-Benzylguanine to brain tumors. *ACS Nano*; 2014; 8 (10): 10383–10395
13. Forrest M. Kievit, Stephen J. Florczyk, Matthew C. Leung, **Kui Wang**, Jennifer D. Wu, John R. Silber, Richard G. Ellenbogen, Jerry S.H. Lee, and Miqin Zhang. Proliferation and enrichment of CD133+ glioblastoma cancer stem cells on 3D chitosan-alginate scaffolds. *Biomaterials*; 2014; 35 (33): 9137–9143
14. Ching-Ting Tsao, Forrest M. Kievit, **Kui Wang**, Ariane E. Erickson, Richard G. Ellenbogen, and Miqin Zhang. Chitosan-based thermoreversible hydrogel as an *in vitro* tumor microenvironment for testing breast cancer therapies, *Molecular Pharmaceutics*, 2014, 11 (7): 2134–2142
15. Vy Phan-Lai, Forrest M. Kievit, Stephen J. Florczyk, **Kui Wang**, Mary L. Disis, and Miqin Zhang. CCL21 and IFNγ recruit and activate tumor specific T cells in 3D scaffold model of breast cancer. *Anti-Cancer Agents in Medicinal Chemistry*; 2014; 14 (2): 204–210
16. Forrest M. Kievit, Ashleigh Cooper, Soumen Jana, Matthew C. Leung, **Kui Wang**, Dennis Edmondson, David Wood, Jerry S. H. Lee, Richard G. Ellenbogen, and Miqin Zhang. Aligned chitosan-polycaprolactone polyblend nanofibers promote the migration of glioblastoma cells. *Advanced Healthcare Materials*; 2013; 2 (12): 1651–1659.
17. Vy Phan-Lai, Stephen J. Florczyk, Forrest M. Kievit, **Kui Wang**, Ekram Gad, Mary L. Disis, and Miqin Zhang. Three-dimensional scaffolds to evaluate tumor associated fibroblast-mediated suppression of breast tumor specific T cells. *Biomacromolecules*; 2013; 14 (5): 1330–1337
18. Fareid Asphahani, Myo Thein, **Kui Wang**, David Wood, Sau Shun Wong, Jian Xu, and Miqin Zhang. Real-time characterization of cytotoxicity using single-cell impedance

monitoring. *Analyst*; 2012; 7; 137 (13): 3011–9

19. Fareid Asphahani, **Kui Wang**, Myo Thein, Omid Veiseh, Sandy Yung, Jian Xu, and Miqin Zhang. Single-cell bioelectrical impedance platform for monitoring cellular response to drug treatment. *Physical biology*; 2011; 8 (1): 015006
20. Forrest Kievit, Freddy Wang, Chen Fang, Hyejung Mok, **Kui Wang**, John R. Silber, Richard G. Ellenbogen, and Miqin Zhang. Doxorubicin loaded iron oxide nanoparticles overcome multidrug resistance in cancer in vitro. *Journal of Controlled Release*; 2011; 152 (1): 76–83
21. **Kui Wang**, Chao Zheng, Cheng Wu, Ming Gao, Qiang Liu, Kechun Yang, Kevin Ellsworth, Lin Xu, and Jie Wu. α-chloralose diminishes γ oscillations in rat hippocampal slices. *Neuroscience Letters*; 2008; 441 (1): 66–71
22. Metin Akay, **Kui Wang**, Yasemin M Akay, Andrei Dragomir, and Jie Wu. Nonlinear dynamical analysis of carbachol induced hippocampal oscillations in mice. *Acta Pharmacologica Sinica*; 2009; 30 (6): 859–867
23. **Kui Wang**, Ming Yan, Lin Xu, and Jie Wu. The updated advancements in θ oscillations in the hippocampus. *Progress in Physiological Sciences*; 2008; 39 (4): 331–334
24. Yan Li, Y Ming an, **Kui Wang**, Lin Xu, Wei Xu, and Ping Kai OuYang. Study on dsRNA mediated gene silencing in *Saccharomyces cerevisiae*: suppressing the expression of GRE3 gene. *Progress in Biochemistry and Biophysics*; 2007; 34 (3): 292–298

CONFERENCE PAPER/ABSTRACT

1. **Kui Wang**, Stephen J. Florczyk, Forrest M. Kievit, and Miqin Zhang. Chitosan-hyaluronic acid scaffolds as a mimic of glioblastoma microenvironment extracellular matrix. *The 2014 BMES Annual Meeting.* San Antonio, TX. 2014
2. **Kui Wang**, Stephen J. Florczyk, Forrest M. Kievit, and Miqin Zhang. Culture of human GBM cells on ECM-mimicking chitosan-hyaluronic acid scaffolds increases malignancy and drug resistance. *The 19th Annual Education Day and Scientific Meeting of the Society for Neuro-Oncology*. Miami, FL. 2014
3. **Kui Wang**, Jon Valla, and Jie Wu. Deficits of hippocampal theta oscillations in an Alzheimer's disease model of triple transgenic mice. *The 2008 Arizona Alzheimer's Consortium Annual Conference.* Phoenix, Arizona. 2008

4. Yan Li, **Kui Wang**, Ming Yan, Lin Xu, and Ping Kai OuYang. Suppression of GRE3 expression *Saccharomyces cerevisiae* by double-stranded RNA mediated gene silencing. *Industry Biotechnology Postgraduate Forum of Yangtze River Delta*. Wuxi, China. 2006